Vibration Isolation for Rotorcraft Using Electrical Actuation

Henderson, Jean-Paul

Award date:
2012

Awarding institution:
University of Bath

Vibration Isolation for Rotorcraft Using Electrical Actuation

Jean-Paul Henderson

A thesis submitted for the degree of Doctor of Philosophy

University of Bath
Department of Mechanical Engineering

June 2012

Table of Contents

List of Figures

Acknowledgements

There is something magical about helicopters. May the work presented here be used for the good of humanity.

To my principal supervisor Prof. Andrew Plummer; the sheer number of times he has sat, thought, and guided this project with in-depth understanding is highly appreciated. Prof. Nigel Johnston and Prof. Chris Bowen have each contributed at crucial times with their own fields of expertise. My industry liaison Peter Court has watched and agreed with the turns this project has taken with great interest. That Prof. Phil Mellor at Bristol University was willing to assist was always appreciated. It has been a pleasure to work with supervisors of such high standard.

Numerous technicians have contributed to the machining, assembly, electrical wiring, and data acquisition of the experimental work. I would like to mention Graham Rattley's and Alan Jefferis's particular contributions to the project. Thank-you to all the researchers who have made the University of Bath Centre for Power Transmission and Motion Control a positive environment to work in. Support, ideas, emotion and debates about trivia or the future of society will always be remembered with great fondness.

A thank-you to my family on the other side of this Earth. Emails have been a poor substitute for not being near you. I would also like to acknowledge the talent of my late grandfather, whose work has given me inspiration.

Finally, to Calkin and Nolan, may all the tears and joy that surrounded this body of work be a sign of great love.

The project was funded by the University of Bath, Great Western Research, and AgustaWestland Ltd from October 2008 to September 2011.

Statement From Industrial Liaison

The following statement was added at the request of AgustaWestland Limited.

AgustaWestland Limited part sponsored the student's degree through the University of Bath including hardware to be kept by the University. AgustaWestland Limited wishes to acknowledge the support of the Student and the Universities and their cooperation throughout this Student Sponsor Agreement, together with that of "Great Western Research" (GWR) for their funding and support with this Project.

The Student Sponsor Agreement dated 25th September 2008 specifies some rules to be observed for preserving the confidentiality of the information in this thesis. The reader must be aware of the following and shall not disseminate anything that belongs to the Student, his sponsors, the Universities or AgustaWestland Limited without the prior consent of the original owner(s) while restrictions on use are in place.

Figures or Diagrams marked as "Copyright AgustaWestland Limited" are owned exclusively by AgustaWestland Limited.

The Student and Universities have formally assigned their rights to the invention in this thesis to AgustaWestland Limited, Patent Application No. GB1112244.7 refers, and AgustaWestland Limited is granted exclusive rights for "V/STOL and rotary wing aircraft and all products and services associated with the same for civil and military aircraft".

Abstract

The Active Control of Structural Response (ACSR) vibration suppression system, where hydraulic actuators located between the gearbox and the fuselage are used to cancel vibration in large helicopters, has been used successfully for many years. However the power consumed by the actuators can be high, and using hydraulic actuation for smaller rotorcraft has not been seen as practical. In contrast to active vibration reduction systems, passive vibration isolation systems require no external power. Passive vibration isolation systems however have the disadvantage of being limited to working at one specific frequency which will not be acceptable as slowed rotor flight becomes more common for fuel efficiency and noise legislation reasons.

In this thesis two electrically powered actuation concepts, one piezoelectric, and one electromagnetic were initially evaluated. An electrically powered actively augmented passive, or hybrid, vibration reduction system based on an electro hydrostatic actuator (EHA) concept was proposed to be developed further. This hybrid actuator will have a wider range of operating frequencies than a purely passive system, and have lower power consumption than a purely active system. The design is termed a "Resonant EHA"; in that the resonant frequency of the coupled fluid, pump and electric motor rotor inertia matches the fundamental vibration frequency. The hydraulic cylinder, fluid and pump act as a single stage gear ratio, and the. brushless electric motor's inertia is the main resonating mass as in a Dynamic Antiresonant Vibration Isolator (DAVI) passive vibration reduction system. The electrical power is used to compensate for friction in the actuator and other losses, and if needed can shift the operating point away from the resonant frequency.

Simulation results indicated that a hydraulic circuit in which the pump leakage is fed back into the low pressure line would introduce unacceptable disturbances in the flows to and from the cylinder. To eliminate the source of the disturbances, a fully integrated electric motor and pump circuit design was chosen in which the electric motor is immersed in hydraulic fluid.

An EHA demonstrator was built sized for a 1.5 tonne rotorcraft. For sizing comparison purposes the frameless brushless D.C motor for each strut of 1.5 tonne rotorcraft has a rotor and stator mass of approximately 1 kg, and can produce a continuous stall torque of 2 Nm. The bidirectional pump has a displacement of 1.5 cm^3/rev, the mean system pressure was taken as 90 bar, and the double ended hydraulic cylinder has a 32 mm diameter bore, and 18 mm rod.

Initial test results for the proof of concept EHA showed highly significant free play with a reversal of torque direction, resulting in unacceptable loss in transmission stiffness. The free play was traced to the gear pump and a hypothesis for the origin of the free play was put forward. To avoid torque reversals the EHA was further tested with a constant offset torque bias which proved successful in restoring a sufficient stiffness to the transmission. The sizing of the electric motor and power consumed with a non-zero offset torque is greater than a torque reversing motor, which limits the immediate application of the device in the present form. Future research investigating the use of other transmission elements, such as a piston pump, to obtain a more linear stiffness is recommended.

As a hybrid vibration isolation system a Root Mean Square (RMS) reduction by a factor of four and near elimination of the fundamental frequency vibrations was achieved for the frequency range of 10 to 20 hertz.

List of Abbreviations

ACSR	Active Control of Structural Response
AW101	AgustaWestland Limited 101 Series Helicopter
DAVI	Dynamic Anti-Resonant Vibration Absorber
DC	Direct Current
EADS	The European Aeronautic Defense and Space Company
EHA	Electro Hydrostatic Actuator
EMA	Electro Mechanical Actuator
HMD	Hybrid Mass Damper
LIVE	Liquid Isolation Vibration Eliminator
LVDT	Linear Variable Differential Transformer
MTOW	Maximum Take-Off Weight
RMS	Root Mean Square
SARIB	Systeme Antivibratoire a Resonateur Integre a Barres
TMD	Tuned Mass Damper
VIREA	Vibration Isolation for Rotorcraft using Electrical Actuation

List of Symbols

a	Mechanical gearing ratio length
a_{Co}	Conic cross-sectional orifice area
A	Area
A_{Ch}	Area of chamber
A_{Va}	Area of poppet valve seat
b	Mechanical gearing ratio length
B	Fluid bulk modulus
B_{Ef}	Effective bulk modulus
c	Damping
c_{Cf}	Viscous friction coefficient
c_{Fr}	Damping coefficient of poppet in free state
c_{Sh}	Rotational friction of motor and pump
c_{St}	Poppet end stop damping
C	Capacitance
C_D	Orifice discharge coefficient
C_F	Pressure difference coefficient
C_I	Driving cycle intensity factor
d	Displacement
d_{Fr}	Piezoelectric stack free displacement
D	Pump displacement
D_{Ch}	Chamber diameter
D_{Va}	Diameter of valve poppet
E	Young's modulus
E_{mo}	Motor voltage
f	Frequency
F	Force

F_{Ac}	Actuator force
F_{Bl}	Piezoelectric stack blocking force
F_{Pr}	Preload force on poppet valve spring
F_{Fc}	Friction force acting on piston
F_{Mx}	Piston friction absolute value
i	Current input
I	Inertia
k	Linear spring stiffness, strut stiffness
k_{Sp}	Poppet valve spring stiffness
k_{St}	Poppet valve end stop stiffness
$k(T)$	Heat transfer coefficient
K	Volumetric stiffness
K_C	Back electromotive force constant
K_{Ei}	External leakage coefficient of pump
K_{Fl}	Fluid bulk modulus over volume
K_{Il}	Internal leakage coefficient of pump
K_{Lc}	Internal leakage coefficient of the piston
K_{Pi}	Piezoelectric stack volumetric stiffness
K_{Ra}	Radial wall volumetric stiffness
K_{Ax}	Axial wall volumetric stiffness
L	Length, or inductance of electric motor
l	Characteristic length of fluid trapped in orifice
m_{Eq}	Equivalent mass of geared element
m_{Va}	Poppet valve mass and added mass
m_{Is}	Liner resonating mass for passive isolation
P	Pressure
P_{Ac}	Accumulator Pressure
P_{Do}	Pressure downstream of poppet valve

P_{Up}	Pressure upstream of poppet valve
Q	Flow
Q_{Ac}	Accumulator flow
Q_{Cl}	Refeeding circuit flow
Q_{El}	External leakage flow
Q_0	Effective orifice flow
R	Resistance
t	Thickness
T_{Mo}	Total motor torque
T_{ex}	External torque acting on motor
u	Velocity
U	Hysteric loss per unit piezoelectric stack volume per cycle.
v_{Ac}	Piezoelectric stack active volume
V	Voltage
V_{Ho}	Volume of hose
x	Valve position in poppet valve, or gearbox displacement input
x_{St}	End stop position
x_{Ro}	Gearbox displacement
ΔT	Temperature rise
ρ	Fluid density
θ	Poppet valve conic angle, or shaft rotational angle for electric motor
ζ	Damping ratio
ω	Angular velocity

Chapter 1
Introduction

The motivation and goals of this thesis are given in this chapter.

1.1 Overview

1.1.1 Motivation

There is a special quality to a machine with the ability to come out of the sky and rescue those on the ground. The long rotor blades of a helicopter lead to a low disk loading compared to competing vertical take-off and landing aircraft, therefore the helicopter is, and will continue to be, a valuable mode of transportation throughout the world. Igor Sikorsky, the inventor of the modern helicopter, has been attributed to compare the helicopter to a vehicle that:

"…approaches closer than any other to fulfilment of mankind's ancient dreams of the flying horse and the magic carpet."

However the dream of flight as smooth as a magic carpet is interrupted by uneven rotor loads generated when the rotor blades rotate into, and out of, the relative wind present during a rotorcraft's forward flight. These oscillatory rotor loads, if left unchecked, produce a continuous vibration that can reduce structural lifetime, limit the flight envelope of the rotorcraft and most importantly fatigue the passengers and crew. It is this persistent vibration that this project seeks to remove in the most efficient manner possible, and ultimately fulfil the dream of a magic carpet flight experience.

There are two trends in aviation that additionally motivate the VIREA project. The first trend is the general electrification of aircraft systems. The desire to replace separate hydraulic, pneumatic, mechanical and electrical power transmission systems with a single electrical power transmission system has appeal in terms of perceived simplicity and efficiency. The second trend is the evolution of helicopters' rotors from rotating at a fixed speed to rotating at slightly reduced speeds. In the future the design of helicopters will at high speeds offload rotor lift to a stub wing allowing the rotor to be slowed, leading to a combination of either a higher top speed, longer range or better fuel economy with lower noise emissions. This leads to a vibration isolation system which must be able to allow a change in operational frequency.

1.1.2 Project Objective

The Vibration Isolation for Rotorcraft using Electrical Actuation (VIREA) project is focused on the investigation and testing of a next generation vibration suppression system for use in rotorcraft. The project's industrial partner, AgustaWestland, gave direction to the project by requesting the investigation of electrically actuated struts that are weight efficient and scalable.

The vibration suppression system is to be mounted individually on four struts between the rotor and the fuselage of a nominal 15 tonne helicopter as shown in Figure 1.1. The strut supports steady flight loads and the role of the actuator inside the strut is to deform the strut to primarily suppress vibrations at the blade passing frequency. An electrically powered vibration suppression system is to be investigated as this has the perceived advantages of being low maintenance and in principle allowing scalability of the same vibration suppression system across a wide range of rotorcraft sizes.

Although potentially scalable, in order to be a competitive system the proposed electrical actuator must be as weight efficient as current passive inertial mass type strut systems, and produce dynamic forces equivalent to hydraulically actuated systems.

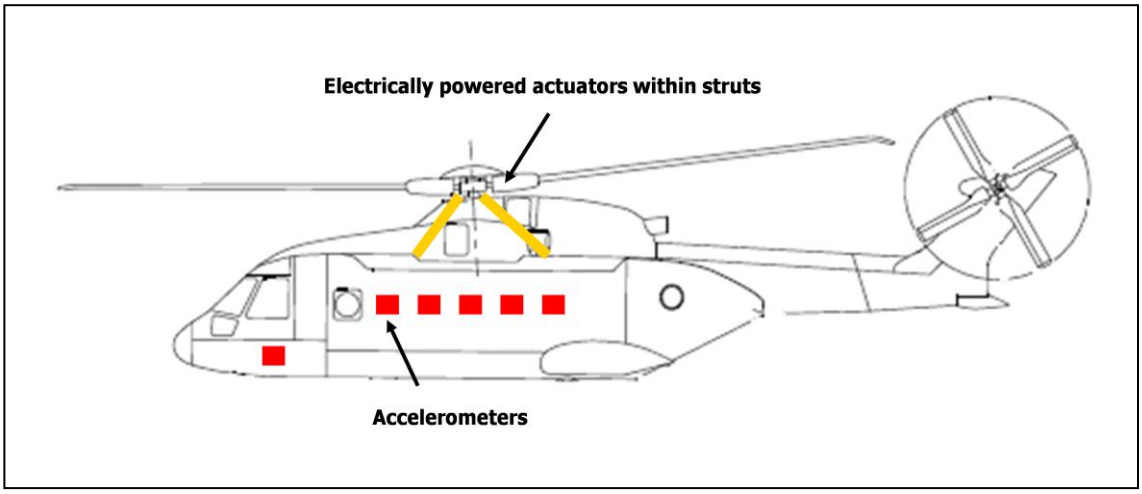

Figure 1.1 Location of actuators relative to helicopter body.

1.1.3 Actuator Target Specifications

The final vibration suppression system is to be mounted between the rotor and the fuselage of a fifteen tonne helicopter and primarily suppress the blade passing frequency. For a single actuator acting in parallel with a stiff 100kN/mm strut that is taken as acting as a linear spring the following list acts as guideline specifications for the final device:

i. Greater than ±35 kN force

ii. Greater than ±350 μm dynamic stroke

iii. 18 Hz basic operating frequency, with minus 10% frequency change potential

iv. Accommodates ±2 mm semi static stroke

A full description of target specifications is given in Appendix A.

1.2 Aims

Although this Ph.D. focuses on an application in rotorcraft, it is recognised that in the field of mechanical vibration control the development of a novel active vibration suppression system would also have potential applications including but not limited to: wheeled vehicle suspension, marine applications, robotics, industrial machinery, civil earthquake engineering, civil wind engineering and power generation. The broad aim of this Ph.D. is therefore to make a significant contribution to the field of electrical actuator design for active vibration control. In summary; this Ph.D. aims to investigate designs of an electrical actuator to produce sufficiently high dynamic forces to deform a stiff spring and allow satisfactory vibration suppression between two masses for a specific range of frequencies.

The aim of the VIREA project to be an interface between electrical and mechanical power can be illustrated in Figure 1.2, where question marks represent the wide range of device architectures available. Figure 1.2 shows that both external electrical power and mechanical power is being can be put into and taken out of the actuator, that there is energy storage potential within the actuator.

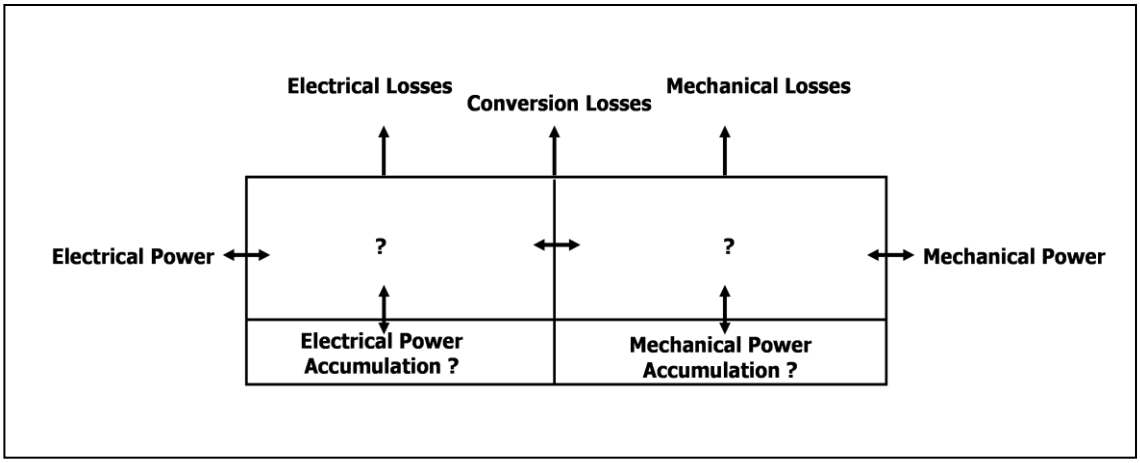

Figure 1.2 Power flows into and out of target actuator.

1.3 Novelty of Work

The novelty of work claimed in this thesis includes:

(i) Concept generation based on a hybrid active-passive geared resonating mass actuator where the resonating mass is a moving element of the electric motor, for use in vehicles to enable widened bandwidth vibration isolation with low power requirements. One sub-set of hybrid active-passive vibration isolation devices is termed a "Resonant Electro Hydrostatic Actuator (EHA)". Patent application A12850GB D08 which describes the Resonant EHA has been assigned to the project industrial partner AgustaWestland.

(ii) Construction and experimental testing of a Resonant EHA.

(iii) Analysis of performance of the Resonant EHA in comparison with theoretical and simulated characteristics.

1.4 Structure of Thesis

In this thesis the following structure is used: Chapter 2 gives a literature review of vibration reduction strategies and electrical actuator design, Chapter 3 examines a piezoelectric actuator design, Chapter 4 details work on the strut and actuator as a hybrid active-passive system and circuit level design of a Resonant EHA, Chapter 5 describes the experimental device and initial experimental results, Chapter 6 compares experimental and simulation results, and Chapter 7 draws a number of conclusions and sets out future work.

Chapter 2
Literature Review

A review of vibration isolation strategies and a review of electrical actuator design are given in this chapter. Active, passive and finally hybrid active-passive vibration isolation strategies are reviewed in sections 2.1, 2.2 and 2.3 respectively. Two types of electrical actuators: piezoelectric based actuators and electromagnetic based actuators are reviewed in sections 2.4 and 2.5 respectively.

2.1 Active Vibration Systems

A successful vibration suppression system, termed Active Control of Structural Response (ACSR), currently employed by AgustaWestland in the AW101 places a hydraulically powered actuator in parallel with each static load carrying strut, as shown Figure 2.1. The actuator can change the strut length dynamically to accommodate rotor vibration without transmitting force to the fuselage. Each of the four compliant tubes which each actuator is mounted in parallel to acts as a stiff spring which both carries the static loads and transmits dynamic loads.

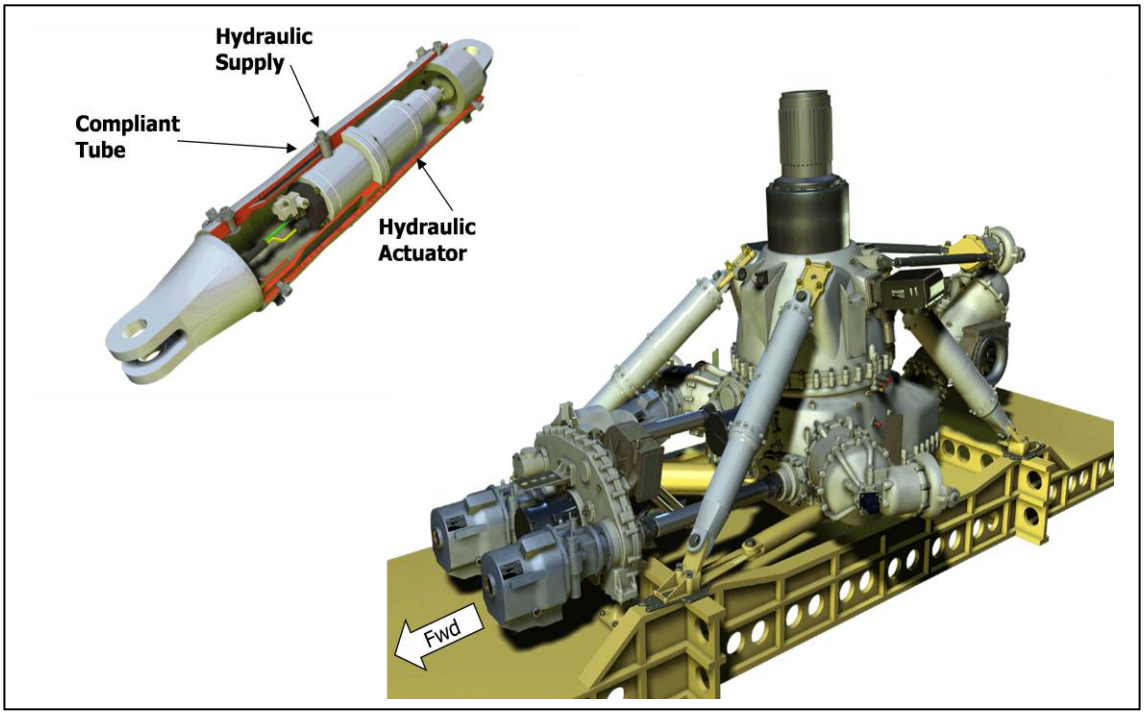

Figure 2.1 Single strut cutaway showing a single hydraulic actuator (left) and gearbox with four struts (right). Image copyright AgustaWestland Limited.

The ACSR system uses the principle of superposition where a controlled secondary excitation is applied to a structure which is being excited by a primary source. Using actuators in the vibration reduction system gives flexibility via a control system over when, where and what magnitude input force should be applied to the system, all of which can be adjusted in real time. Feedback, feed forward, weighted, unweighted, fixed, adaptive are examples of control methods which can be implemented, as described in [2]. In the ACSR system magnitude and phase of the force demands for each actuator are calculated by a control algorithm minimising the sum of accelerometer readings across the fuselage [3], rather than simply isolating the fuselage from the gearbox. This is significant as the superposition forces will in practice minimise disturbances from every transmission path, for example the disturbance in air from the passing blades impinging on the fuselage, not just the forces passing through the struts.

Electrically powered actuators have a lower force per unit volume than hydraulically powered systems, and are therefore suited to lower force vibration suppression applications. Active isolation of tables, for example in semiconductor manufacturing equipment, are in commercial use where either electromagnetic or piezoelectric actuators are employed [4]. Space applications for isolating sensitive payloads using moving coil actuators [5] are also relevant. Adaptive optics where a telescope mirror is mounted on piezoelectric actuators, have improved the optical resolution of telescopes and are an example of nanometer resolution motion control [6]. Active engine mounts for vehicles have been investigated with solenoid actuators [7].

Active vibration reduction systems all require an external power source, which in some applications may be undesirable. Passive vibration reduction systems which require no external power are an alternative, which will be described in the next section, Section 2.2.

2.2 Passive Vibration Isolation

Soft mounts are effective for damping high frequency vibration, however at low frequencies the displacement of the objects being isolated is unacceptably large, therefore these are not used on helicopters [3].

DAVI (Dynamic Anti-Resonant Vibration Absorber) and SARIB (Systeme Antivibratoire a Resonateur Integre a Barres) are examples of tuned-mass vibration absorbers in which a pivoted lever arm and mass are carefully chosen in relation to a spring stiffness so that the mass vibrates out of phase with the incoming vibrations. The pivoted lever arm acts as a mechanical gearing ratio that makes the resonating mass appear larger by a factor of the gearing ratio squared. Figure 2.2 from [1] shows a recent update of SARIB to include a torque tube instead of the spring between the fuselage and the main gear box, where the gearing ratio is determined by the lengths “a” and “c”. It is claimed that the torque tube leads to a very compact design where integration with the gearbox is simplified. Due to the fixed nature of the system in situ iterative tuning still has to be carried out in order to exactly match the resonating mass to the desired isolation frequency.

A rotary version of a mechanical passive differential mass device, namely the “inerter” [8, 9] has been implemented in Formula 1 motor racing to complement the suspension system. The inerter is compact due to its rotary nature, having fewer limitations in terms of space compared to a flapping tuned mass which requires a large arc in which to oscillate in. The rotary device also is less susceptible to stroke saturation compared to linear differential mass devices.

The use of fluid itself as the resonating mass is the idea behind the Liquid Isolation Vibration Eliminator (LIVE) [10, 11], or previous designs [12], which have been used successfully. For the LIVE system there is a hydraulic gearing mechanism due to the difference in area between the driven piston and the tube which contains the resonating fluid. The LIVE system benefits from being completely enclosed, eliminating the possibility of leakage and is a compact design where the fluid itself is both the gearing and the resonating element. The Anti-Resonance Isolation System (ARIS) is also based on hydraulic principles and has been implemented commercially by Eurocopter [1].

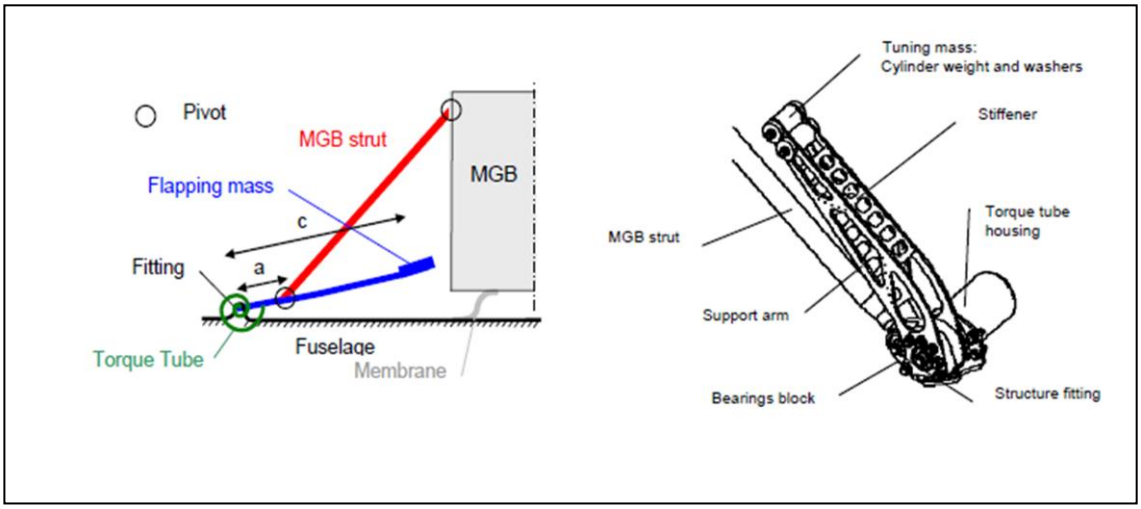

Figure 2.2 Torque tube SARIB passive vibration isolation system from [1].

Passive systems are relatively simple and have good stability. Passive systems are however limited by having fixed parameters, and therefore cannot adapt to variations in input frequency or mass (due to for example cargo or fuel variations). The bandwidth of tuned mass vibration absorbers is traditionally low but using twin vibrating masses to increase the bandwidth of the resonating system has also recently been numerically demonstrated [13]. Variable (or adaptable) passive systems are more flexible with respect to long term variation in conditions by allowing real time tuning of the device. The addition of an actuator that changes the location of a mass, and therefore the gearing ratio and effective inertia of a tuned mass system is one example of a variable passive system [14]. Examples of variable passive systems for use in rotorcraft are given in Kydsinski [14].

Hybrid systems, which are defined as having a combination of active and passive elements to directly counteract vibration transmission, offer a means of altering the magnitude of response, and will also provide wider bandwidth potential compared to a passive system, are reviewed in Section 2.3.

2.3 Hybrid Vibration Isolation

In hybrid vibration isolation systems there are components that actively assist the vibration isolation, and components that make the system acts as a passive damper if the energy input to the system is removed [15]. In this thesis hybrid vibration isolation is taken as being distinct to "semi-active" vibration isolation strategies, where semi-active implies variable stiffness or variable damping systems which can be controlled. The passive inertial mass forces in a hybrid system can be geared, or non-geared according to the device design and requirements.

Non-geared reaction mass, or proof mass actuators for space applications are presented in [16]. Incorporating passive isolation leads to potentially lower power requirements from the actuator. The use of a "Smart Spring" with electromagnet to actively isolate marine machinery in parallel with passive elements is described in [17]. Peak forces that are normally transmitted across a passive mount at resonant frequencies are able to be reduced with recursive least squares based control [18, 19]. The destabilisation of linear non geared inertial actuators when the inertial mass makes physical contact with end stops has been examined in [20]. An impulse is transmitted into the structure coinciding with stroke saturation, and the system is shown to become unstable. In the context of this project this paper inspired the concept of the avoidance of stroke saturation by using a rotary resonating element. Hybrid active-passive devices for noise and vibration suppression in aircraft has a patent issued [21], however the use of device gearing in order to minimise the resonating mass does not seem to be emphasised. Hybrid hydraulic engine mounts including actively assisting solenoid actuator have been reviewed and built [22, 23]. In engine mounts the fluid is the resonating element but the addition of the active actuator gives the ability to tailor the vibration response to specific driving or load conditions. Hydraulic hybrid active-passive systems where the fluid itself is the controlled resonating element are possible. Incorporating active elements into system where the fluid is the resonating mass by using a magnetoreological fluid and externally controlling the fluid has been attempted [10, 24].

In the field of civil engineering, implementation of hybrid mass dampers (HMD) on tall slender buildings to counteract wind and earthquake loading has occurred since 1995 [24-26]. Buildings will have resonance frequencies determined by their height and width which if excited can cause unacceptable sway for their occupants. In this application passive and active vibration isolation solutions are common but the use of hybrid systems is increasing [27]. One example of an HMD

in a building is a high mass raft that acts as a compound pendulum, which passively is a tuned mass damper, but is also connected to rotary AC servo motors that drive the raft through ball screw gearing [28]. Another recent proposed application of HMD is the active structural control of offshore wind turbines, particularly floating wind turbines where the tower pitch angle in response to disturbances must be kept within reasonable bounds [29]. The influence of the gear ratio of the actuator is noted, recognising the impact of the gearing mechanical design on the ultimate response of the system.

Actuators are to be part of an active or hybrid vibration reduction system, therefore a review of piezoelectric actuators and electromagnetic follows, in Section 2.4 and Section 2.5.

2.4 Piezoelectric Actuators

2.4.1 Piezoelectric Actuators Overview

A piezoelectric stack is characterised by being a monolithic object with micrometre order displacements, and up to tens of kilonewtons forces [30]. Although there are different forms of piezoelectric actuators with different geometries and poling directions such as bender actuators, only piezoelectric cylindrical stacks are considered due to the kilonewton order forces required in this application. Other electrically powered actuators, such as magnetostrictive, or shape memory alloy based devices exist, however piezoelectric actuators are closer at achieving the power density and velocity required for the proposed application [31]. The piezoelectric effect is where an electrical field is applied to a piezoelectric material and a strain is induced in the material. The strain magnitude is dependent on the material piezoelectric coefficients, dielectric properties, geometric conditions including layer thickness and magnitude of applied voltage.

A previous internal report [32] includes analysis of using a single piezoelectric actuator as a direct replacement for the current hydraulic actuator in the AW101 helicopter. For a single stack, the closest feasible solution was to use a positive DC bias voltage, which allowed the full length of the permissible strain (-0.03% to +0.15% gives ±0.9% with a DC bias). Using a DC bias, a ±30kN at ±300μm specification was calculated to be able to be obtained by a custom 55mm diameter, 550mm long stack. The conclusion of the report is that simple piezoelectric stacks are too long to be practical to obtain the required strain. A piezoelectric stack system

would also have to have the semi static displacement of the spring compensated for by some additional mechanism. Eurocopter [33] use piezoelectric stacks, to reduce the 1st gear meshing frequency between the gearbox and the fuselage for helicopter interior noise reduction. By using three piezoelectric actuators with clamped ends to the strut, it is possible to use the bending vibrations as well as the longitudinal vibrations from the piezoelectric. It was shown that the actuator authority is sufficient to reduce the 1st gear-meshing frequency (600 Hz) independent from the actual flight condition up to 19.5 dB. EADS Astrium [33] have researched separated piezoelectric stacks for active isolation of vibration loads for the Ariane V launcher. The strut developed can produce ±16 kN and ±0.25 mm stroke.

Using gearing to increase displacement comes at the expense of a reduction in force. If non-linear gearing such as a buckling mechanism is used, more work could be done at lower displacements, then a theoretical doubling in the work output of the piezoelectric actuator is possible [34]. Using a bender type piezoelectric actuator in compression, it is possible to buckle the actuator itself, and to gain larger displacements as a result. This mechanism is examined in [35] where the actuator is used to control the aileron of a UAV. As opposed to gearing, by using motion accumulation it is possible to obtain longer strokes without sacrificing the maximum force obtainable. Longer strokes are obtained through repeated motion therefore the devices power density can be increased compared to a stand-alone piezoelectric stack. Piezoelectric devices with mechanical motion accumulation such as the Inchworm [36] actuator and ultrasonic rotary motors have been used for milliwatt scale applications. A feed screw based piezoelectric actuator with motion accumulation is presented in [37, 38]. The use of optimisation techniques to improve the design leads to a predicted specific power of 195 W/kg for the design, but peak forces are limited. A device termed a piezoelectric pump (commonly contracted to “piezo pump”), which uses hydraulic motion accumulation is reviewed in detail in the next section.

2.4.2 Piezo Pump Review

The piezo pump concept is a hydraulic rectification mechanism, where fluid is forced out of the pumping chamber through an open outlet at high pressure and into a conventional linear hydraulic cylinder. On the return stroke of the pumping chamber, the outlet shuts off, and the inlet opens drawing fluid into the chamber. Due to the relatively low strains which are typically 0.1% [39] of piezoelectric materials, higher frequency (100 Hz to 5000 Hz) displacements of the

piezoelectric stack are rectified into lower frequency longer displacement motion of the load. For small scale devices in the range of tens of millilitres per minute piezo pumps are becoming commercially available in micro fluidic low backpressure applications such as medical dispensing [40]. The efficiency in terms of input power versus output power of a piezo pump in [41] was found to be 7% using a lead magnesium niobate (PMN) stack or 1% using a lead zirconate titanate (PZT) stack. An experimental efficiency of 7% was also obtained by a separate group [56].

Modelling of active materials with hydraulic motion accumulation has been reported in [42-46]. Neglecting losses, in a positive displacement pump the volume of fluid displaced in time increases with an increase in pumping frequency, therefore there has been much work on attempting to drive the piezoelectric stack at higher frequencies typically in the kHz range. However the flow rate has usually been less than expected. Chaudhuri et al. attribute the decrease in output of a piezo pump at higher frequencies to the inertia of the fluid [46, 47] as seen in Figure 2.3 which shows flow rate in the form of a piston velocity against driving frequency. It is found in [48] that vortex formation at the outlet, or just inside the inlet, will cause pressure losses that will become greater with higher flow rate. The inlet and outlet of the chamber can be controlled by means of active [49-51], passive [52-56], or even Magneto Rheological (MR) valves [57]. The maximum reported pressure differential obtained by these groups have been 10 MPa (100 bar) at 2 kHz [56].

As well as fluid inertia, another significant limitation on increasing the pumping frequency is that the response time of valves is finite [58]. Active hydraulic valves have an open and close frequency in the order of 100 Hz, while high specification servo valves can have a response time of up to 400 Hz. Passive valves, while limited by their intrinsic inertia have been reported operating up to 5500 Hz [56]. Reducing the pressure drop across a series of valves while still maintaining an adequate frequency response is a major challenge in building a piezo pump. An alternate approach to designing piezo pumps is including the pumping element and valves in the piston as shown in a patent application by EADS [59]. Electromagnetic actuators are described in the following section, Section 2.5.

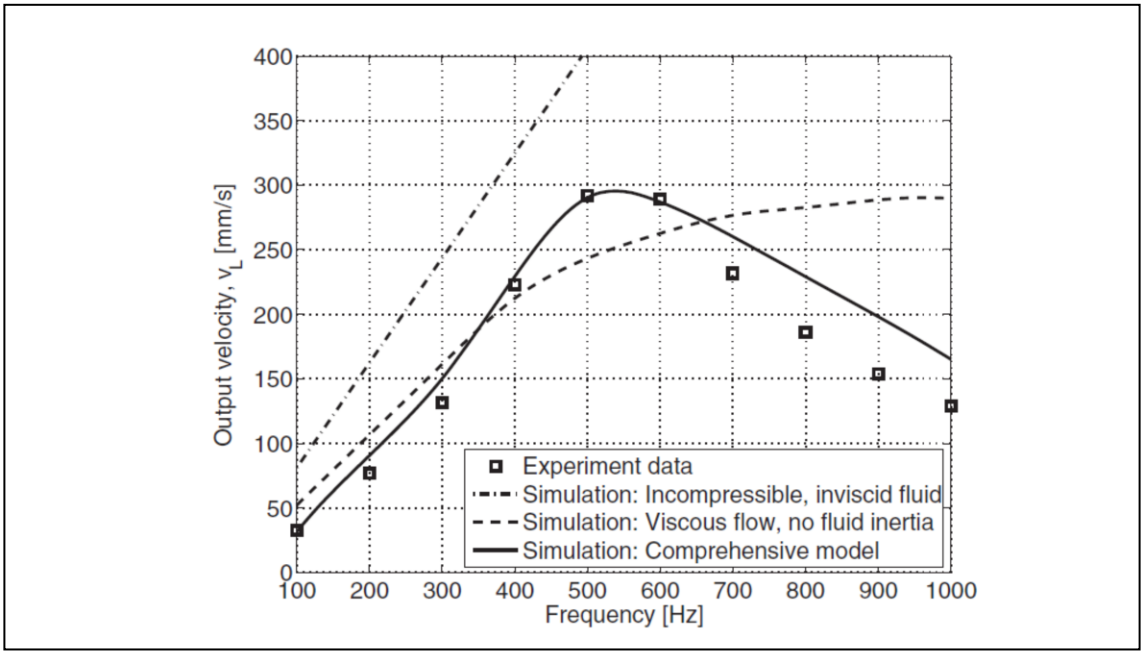

Figure 2.3 Piezo pump experimental and simulation results from Chaudhuri et al. [47].

2.5 Electromagnetic Actuators

2.5.1 Electromagnetic Actuators Overview

Electromagnetic actuators consist of two components: a stator and rotor for rotary devices, or a stator and shaft for linear devices. Typically for a linear moving coil actuator the shaft will have tens of millimetres order displacement, and tens of newtons force [30].

Electromagnetic linear actuators including solenoid actuators, where a plunger tries to minimize the air gap by moving to a position of less reluctance, or moving coil actuators, where a force is produced by the interaction of a perpendicular magnetic field and electrical current, directly convert electrical energy into mechanical energy. The highest forces are in the order of 1 kN for commercially available actuators [30]. To increase the force output of an actuator gearing can be used. Solenoid based linear actuators can only achieve a few millimetres stroke due to the decrease in magnetic field strength with distance. The length of a linear moving coil actuator has to increase to accommodate a longer stroke, giving a larger volume and higher mass. For example, a previous internal report [32] evaluated a direct acting linear electromagnetic actuator with a 30:1 hydraulic gearing ratio. The report concluded that for the 1 kN force required when direct acting in parallel with the stiff spring, the mass of the actuator (40 kg) was too large.

Electromagnetic rotary motors have a higher output per unit volume due to the complete utilisation of the magnets compared to a linear moving coil actuator. For applications requiring linear displacement output gearing will also be incorporated into the rotary to linear motion transmission mechanism. An actuator using mechanical transmission is termed an Electro Mechanical Actuator (EMA). For an EMA where the linear motion is at right angles to the rotary driving axis the gearing could involve cams, a worm screw or a rack and pinion mechanism. For rotary to linear motion along a parallel drive axis lead screws, ball screws, or roller screws can be used. It is difficult to produce lead screws with a high gearing ratio to have greater than 30% power transmission efficiency, while ball screws are limited in the maximum force that can be conveyed [60]. Roller screws have high power transmission efficiency and are back driveable but may have a high inertia or acceleration limitations.

An issue with mechanical gearing is gear lifetime, which is strongly related to the adequate lubrication of the gears. Lubrication by enclosing the entire gear transmission and filling the enclosure with oil is shown for example where the gear transmission is a roller screw [61]. Wear due to the very small strokes for this application, which imply point loads on the balls in a ball screw, is always nearly at the same place, therefore lifetime calculations are less reliable compared to more traditional constant velocity gearing applications.

In event of power failure, friction limits the ability of mechanical gearing to run free, therefore the jamming of mechanical transmission remains a concern and has limited the implementation of EMA's in commercial aircraft. In terms of this project although the run free requirement is not critical, such as in an aircraft aileron, it would still be preferable. Hydraulic power transmission has a run free capability through the use of pressure relief valves therefore an electrically powered actuator with hydraulic transmission is reviewed further.

2.5.2 Electro Hydrostatic Actuator

An Electro Hydrostatic Actuator (EHA) is a device in which a hydraulic pump transfers the rotational motion of an electric motor to an output cylinder by means of fluid under pressure. The ratio of piston area to pump displacement determines the gearing ratio. There are two types of EHA, an EHA with fixed pump displacement and variable motor speed and an EHA with

variable pump displacement and a fixed motor speed. The fixed pump variable speed motor is more popular due to its simple structure.

The lessons learned with using EHAs in a the Airbus A380 were outlined in [62]. A summary of the main issues with regard to commercial implementation of EHA in [62] were:

(i) Pump performance: design of an efficient variable speed pump is challenging.

(ii) Heating is a problem as the system is relatively enclosed.

(iii) The power electronics need to be lighter and have smaller EMI/Lightning filter sizes.

An experimental EHA for use in the aileron of an F-18 aircraft has been described [63]. For use as an aileron the experiment was successful, however, for dynamic operations a drop in performance with increasing frequency is observed due to the acceleration limitations of the motor. Modelling an EHA including non linear actuator piston friction, the refeeding circuit and a variable gain PID controller is found in [64]. It is claimed that the variable gain controller introduced into the model compensates for the non-linear friction. Compared to a conventional hydraulic system the potential for an EHA system to be more energy efficient is shown in [65]. The extra efficiency is obtained both by using an accumulator to provide a static pressure that counterbalances static loads, and because the hydraulic system does not restrict the flow to provide velocity control.

This thesis will discuss a design process that considered a wide range of actuator configurations which lead to the investigation of a piezo pump for use in an active vibration suppression system, and a Resonant EHA for use in a hybrid vibration suppression system.

Chapter 3
Piezo Pump Actuator

The selection of a piezoelectric actuator design, a description of the piezo pump model with simulation results, and conclusions regarding the feasibility of a piezo pump actuator are given in this chapter.

3.1 Piezoelectric Device Selection

The subjective evaluation criteria used to assist actuator selection was:

i. Potential to meet specific force.

ii. Potential to meet specific power.

iii. Potential to meet dynamic and static displacement.

iv. Potential to meet power transmission efficiency.

Figure 3.1 shows a selection tree of possible concept choices in terms of the piezoelectric device architecture. Figure 3.1 shows that the short linear stroke of the piezoelectric stack can be transferred to longer strokes through either gearing or motion accumulation, with mechanical or hydraulic methods available.

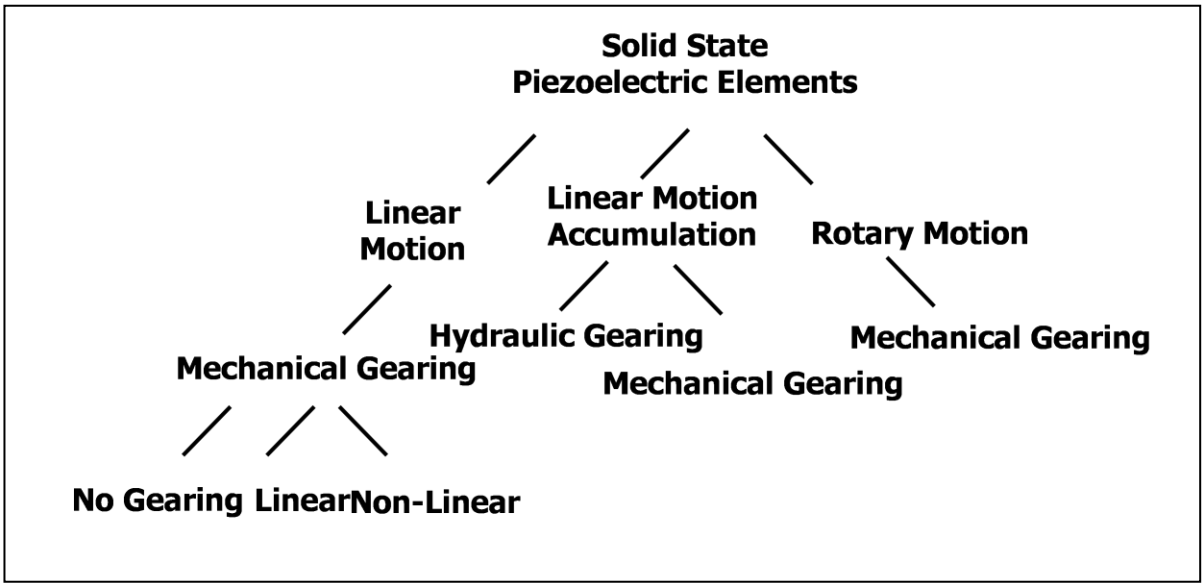

Figure 3.1 Piezoelectric actuator device architecture selection tree.

From the literature review in Section 2.4.1 it is apparent that active actuator requirements for dynamic stroke, specific force amplitude and specific power are unrealistic for a directly coupled piezoelectric actuator. The fundamental vibration frequency for this application is typically 20 Hz, and the power density of any piezoelectric actuator will be greater by operating at a frequency of at least an order of magnitude higher than this. Therefore the piezoelectric stack will be excited at over 200 Hz for the control of a 20 Hz fundamental. Motion accumulation is then needed, which requires rectification. Mechanical rectification is unlikely to be sufficiently robust, therefore hydraulic rectification, a piezo pump was chosen. The piezo pump concept was evaluated first through mechanical and hydraulic modelling, and finally electrical and thermal modelling.

3.2 Piezo Pump Model

The hydraulic system that is to be used to convert a unidirectional pump to bidirectional motion is shown in Figure 3.2. The unidirectional pump shown in Figure 3.2 is the piezo pump shown in Figure 3.3. In comparison to the original ACSR system the hydraulic supply has been transferred from a common shaft driven hydraulic power pack to individual electrically powered piezo pumps for each strut. The control of the hydraulic cylinder at the 18 Hz fundamental is by the bidirectional servo valve which is the same as the ACSR system. The benefit of this design is the ability to eliminate the shaft driven hydraulic power pack, which is not present on smaller rotorcraft. For the hydraulic system shown in Figure 3.2 the bidirectional hydraulic servo valve's orifice will dissipate energy in the condition the cylinder piston is being driven by the spring returning from extension or contraction, which is a form of passive control. This passive control is assumed to be appropriate for the vibration suppression application but has not been investigated or proven. The piezo pump will have a piezoelectric stack, pumping chamber and inlet and outlet ports governed by unidirectional flow control valves, as shown in Figure 3.3.

Even though the hydraulic cylinder is driving a spring, which is a load where maximum pressure and maximum flow requirements occur separately in the actuator stroke, for initial sizing purposes it is useful to consider that the maximum pressure and maximum flow occur simultaneously. In this study the bidirectional servo valve and hydraulic cylinder dynamics are removed, and solely what is the maximum obtainable flow rate from a piezo pump acting against a defined two port pressure gradient will be investigated.

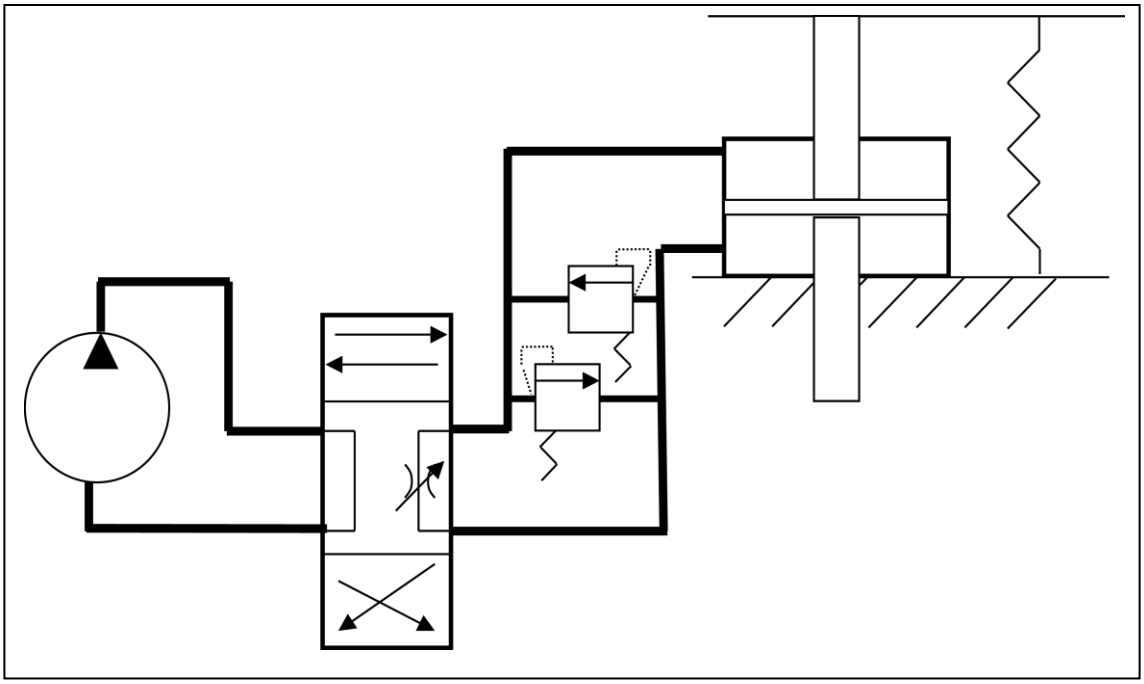

Figure 3.2 Piezo pump hydraulic circuit for bidirectional motion against spring.

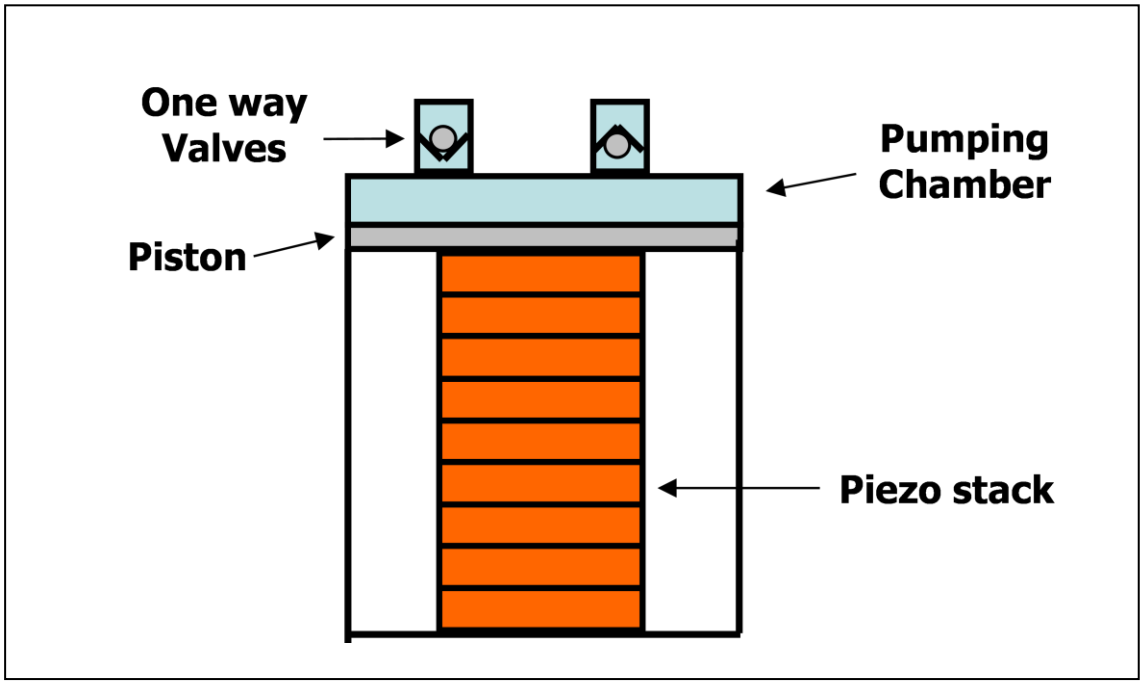

Figure 3.3 Piezo pump schematic diagram.

3.2.1 Blocking Force and Free Displacement Initial Selection

For a first model of a piezo pump, the volume of fluid displaced in the pumping chamber per second can be given by the linear flow equation:

$$Q = A_{Ch} f d \tag{3.1}$$

where A_{Ch} is the cross sectional area of the pumping chamber, f is the driving frequency (Hz), d is the piezo stack displacement amplitude. For the piezo pump linear model the maximum flow rate that can be obtained from a given piezoelectric stack is primarily a function of the piezoelectric stack driving frequency. The piezo stack displacement is dependent on the chamber pressure, so it the flow rate can also be written as:

$$Q = A_{Ch} d_{Fr} f \left(1 - \frac{P}{F_B} A_{Ch} \right) \tag{3.2}$$

where d_{Fr} is the piezo stack unloaded (or free) displacement, P is the pressure change in the chamber, F_B is the piezoelectric stack blocking force. By differentiating Equation (3.2) with respect to the chamber piston area and finding the maximum value by setting the differentiated equation to zero an appropriate choice of blocking force for the piezo can then be found to be:

$$F_B = 2PA_{Ch} \tag{3.3}$$

Therefore the piezo stack blocking force can be sized for guideline purposes as twice the maximum required force. Substituting equation (3.3) into (3.2), the piezo free displacement is found to be:

$$d_{Fr} = \frac{2Q}{A_{Ch} f} \tag{3.4}$$

Therefore the piezo stack free displacement can be sized relative to twice the maximum flow required. The next two sections will investigate under which circumstances the use of the linear flow equation can be justified. Specifically, a more detailed piezo pump model of how the maximum obtainable flow rate is affected by the pumping chamber stiffness, and the unidirectional valve's resonant frequency and orifice area is examined.

3.2.2 Piezo Stack and Chamber Model

A decrease in volume of the chamber leads to a pressure rise which, if greater than the outlet pressure, expels fluid from the outlet of the chamber. Conversely a decrease in pressure below the inlet pressure would allow fluid to enter through the inlet.

Rather than modelling the stiffness of the piezoelectric stack separately, the ability of the piezo stack to resist compression was combined with the fluid bulk modulus to give a total chamber bulk modulus. In total the chamber stiffness was modelled with four components:

i. Volumetric stiffness of the fluid, K_{Fl}

ii. Volumetric stiffness of the piezo stack, K_{Pi}

iii. Radial stiffness of the chamber walls, K_{Ra}

v. Axial stiffness of the chamber walls, K_{Ax}

The increase in pressure of the fluid in the pumping chamber is obtained in the form.

$$\Delta P = K\Delta V \tag{3.5}$$

where K is the total volumetric stiffness ΔV is the change in volume due to piston displacement. The volumetric stiffness of the fluid is:

$$K_{Fl} = \frac{B}{V} \tag{3.6}$$

where B is the bulk modulus, and V is the volume of the pumping chamber. Modelling the piezo stack as a simple spring of stiffness k_{Pi} and considering the relationship between an increase in pressure in the chamber and the resulting compression of the piezo the equivalent volumetric stiffness is:

$$K_{Pi} = \frac{k_{Pi}}{A_{Ch}{}^2} \tag{3.7}$$

For radial expansion of the chamber, equating hoop stress of the chamber wall to fluid pressure [66] results in:

$$K_{Ra} = \frac{4Et}{\pi D_{Ch}{}^3 L} \tag{3.8}$$

where E is the Young's Modulus of the chamber wall material, t is the thickness of the wall material, D_{Ch} is the diameter of the chamber, and L is the length of the chamber. In the axial direction, a similar expansion will occur:

$$K_{Ax} = \frac{E\pi D_{Ch} t}{L A_{Ch}^{\ 2}} \tag{3.9}$$

The stiffnesses are combined in series to give the total chamber stiffness:

$$K = \frac{1}{\frac{1}{K_{Fl}} + \frac{1}{K_{Pi}} + \frac{1}{K_{Ra}} + \frac{1}{K_{Ax}}} \tag{3.10}$$

When the pressure in the pumping chamber is greater than the pressure in the driving side of the cylinder the outlet valve opens and fluid flows out of the chamber, while the intake remains closed. When the pressure in the pumping chamber is less than the driven side, fluid enters from the intake. A lower saturation limit models cavitation and ensures the chamber pressure is not lower than the vapour pressure. The piezo pump unidirectional valves, as shown in Figure 3.3, control the fluid flow into and out of the pumping chamber. Passive valves are chosen to be used as no external power is required for their operation. Poppet valves are modelled, but the model should be similar for a wide range of passive valve geometries.

3.2.3 Poppet Passive Valve Model

The poppet valve model includes valve inertia, fluid inertia at the orifice, variable valve opening times, and valve bounce. The model used is based on the work by Johnston [67]. Figure 3.4 shows the diagram of the passive poppet type valve model. The valve has mass m_{Va} and is attached to a spring with linear stiffness k_{Sp}. When the valve is between the stops the valve has a damping of c_{Fr} however when the valve is on or hits the stops the valve is subject to a high stiffness k_{St} and damping c_{St}. When the upstream pressure P_{Up} is greater than the downstream pressure P_{Do} then the valve opens and a net flow Q occurs. The flow is:

$$Q = Q_0 + A_{Va} u \tag{3.11}$$

where Q_0 is the effective orifice flow rate, A_{Va} is the valve face area and u is the velocity of the valve.

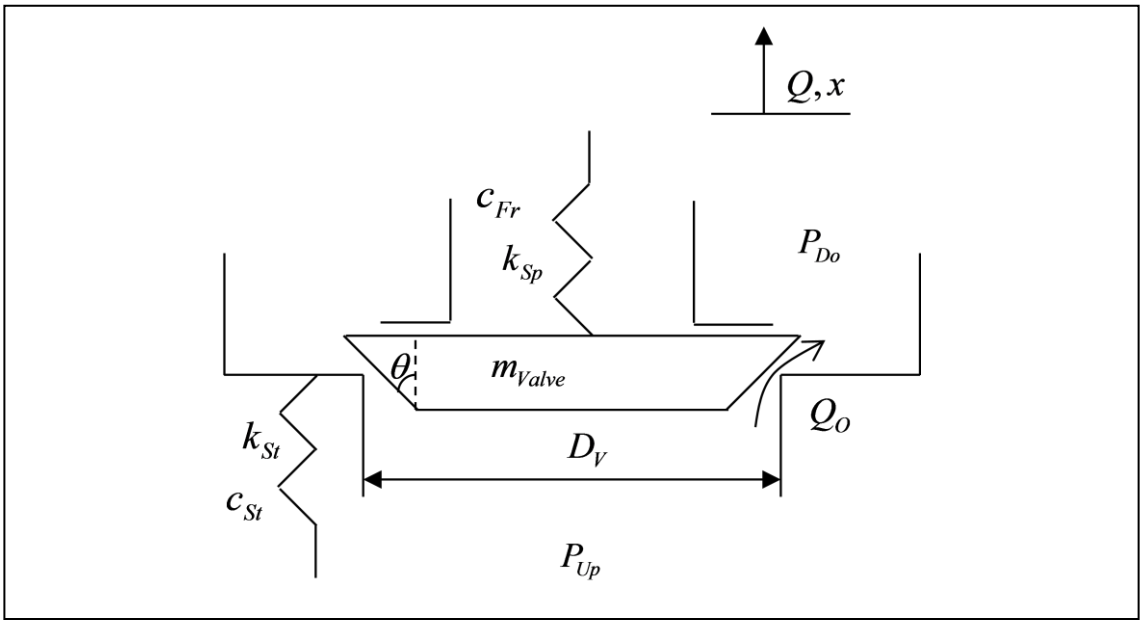

Figure 3.4 Poppet valve components.

The rate of change of effective orifice flow rate is included in the inertia term for valve flow:

$$P_{Up} - P_{Do} = \frac{\rho}{2}\left(\frac{Q_0}{C_D a}\right)^2 + \frac{\rho l}{a}\frac{dQ_0}{dt} \qquad \textbf{(3.12)}$$

where ρ is the fluid density, l is the characteristic length of fluid in the orifice taken to be the thickness of the valve, and C_D is the discharge coefficient which is taken as a constant. The conic orifice cross sectional area a is given by:

$$a = \frac{1}{\cos\theta}\frac{\pi}{4}\left(D_V^2 - \left(D_V - 2\sin\theta\cos\theta x\right)^2\right) \qquad \textbf{(3.13)}$$

where D_V is the shut valve diameter and θ is half the valve angle of the valve cone. A minimum positive orifice cross sectional area is specified to represent seal leakage. Equation 3.11 can rearranged to give:

$$\frac{dQ_0}{dt} = \frac{a}{\rho l}\left(P_{Up} - P_{Do} - \frac{\rho}{2}\left(\frac{Q_0}{C_D a}\right)^2\right) \qquad \textbf{(3.14)}$$

Q_0 can be found through integration.

The velocity u and position x of the valve are found through integration of:

$$\frac{du}{dt} = \frac{F_{Ne}}{m_{Va}} \tag{3.15}$$

The mass being accelerated, m_{Va}, is comprised not only of the mass of the poppet, but also the added mass of the displaced fluid and mass of the spring attached to the valve. The forces on the poppet F_{Ne} are found for three different cases which are when the valve is shut, partially open and fully open. The valve lift x is allowed to be slightly negative to describe the effect of bouncing against the valve seat. There are three potential cases:

Case 1; poppet shut: $x < 0$

$$F_{Ne} = A_{Va} C_F \left(P_{Up} - P_{Do}\right) - c_{St} \frac{dx}{dt} - k_{St} x - k_{Sp} x - F_{Pr} \tag{3.16}$$

Case 2; poppet partially open: : $0 \leq x \leq x_{St}$

$$F_{Ne} = A_{Va} C_F \left(P_{Up} - P_{Do}\right) - c_{Fr} \frac{dx}{dt} - k_{Sp} x - F_{Pr} \tag{3.17}$$

Case 3; poppet fully open: $x > x_{St}$

$$F_{Ne} = A_{Va} C_F \left(P_{Up} - P_{Do}\right) - c_{St} \frac{dx}{dt} - k_{Sp} x - F_{Pr} - k_{St}\left(x - x_{St}\right) \tag{3.18}$$

where A_{Va} is the valve seat area, and F_{Pr} is the preload force on the spring. The poppet body force coefficient C_F is strictly a function of valve design and operating conditions including whether the valve is cavitating, however a constant value is used here. The free and end stop damping values are found by:

$$c = \varsigma 2\sqrt{k m_{Va}} \tag{3.19}$$

where ς is the damping ratio and k stiffness of either the free valve or end stop respectively.

3.2.4 Simulation Parameters

The piezo pump model was implemented in Simulink version 7.9. The solver used was the Adams-Bashworth variable step solver with a maximum step size of 0.02 ms divided by the driving frequency.

The piezo pump model was investigated using parameters based on the large size AW101 rotorcraft. Piezo stack parameters are for the largest commercially available stack from the company PI Instruments; the P-056.90P from the xxP series which is 56 mm in diameter and 169 mm long, with a blocking force of 70 kN. The default parameters for the simulation are shown in Table 3.1.

Table 3.1 Piezo pump parameters.

Parameter	**Value**
Nominal driving frequency, ω	400 Hz
P-056.90P piezo stack stiffness, k_{Pi}	390 kN/mm
P-056.90P piezo stack free displacement range, d	0 to 180 μm
Chamber diameter, D_{Ch}	56 mm
Chamber height, h	1 mm
Chamber wall thickness, t	1 mm
Chamber wall Young's modulus, E	207 GPa
Bulk modulus of fluid, B	1 GPa
Fluid density, ρ	850 kg/m^3
Nominal valve seat diameter, D_{Va}	10 mm
Maximum valve lift, x_{St}	1 mm

Nominal valve spring stiffness, k_{Sp}	50 kN/m
Nominal valve mass (including spring mass and added mass), m_{Va}	1 g
Free damping ratio, ς_{Fr}	0.5
Endstop damping ration ς_{St}	0.1
Endstop stiffness, k_{St}	1000 kN/m
Valve preload, F_{Pr}	0 N
Discharge coefficient, C_D	0.72
Force coefficient, C_F	0.4
Valve half angle, θ	45°
Absolute vapour pressure, P_{Va}	1 bar
Upstream pressure, P_{Up}	100 bar
Downstream pressure, P_{Do}	10 bar

3.3 Piezo Pump Results and Discussion

3.3.1 Piezo Pump Linearity

To verify the passive poppet valve model, the valve mass was idealised to have near zero mass (0.001 g) in order to give a very high response, and the result against frequency was compared with the equivalent valve opening for a simple orifice equation valve model where the valve opens and closes instantaneously, as shown in Figure 3.5. Figure 3.5 shows the flow rate against frequency where high response poppet and pressure difference flow rates up to 500 Hz have a similar tendency but are altered at higher frequencies when the presence of back flow from the returning valve area, and the finite opening time in the high response light mass poppet valve, become significant. Figure 3.6 and Figure 3.7 show the flow rate, orifice area and chamber pressure for several pumping cycles of the simple orifice valve model and high response poppet valve model respectively. The presence of backflow and the proportional opening of the poppet valve can be compared to the instantaneously closing pressure difference valve.

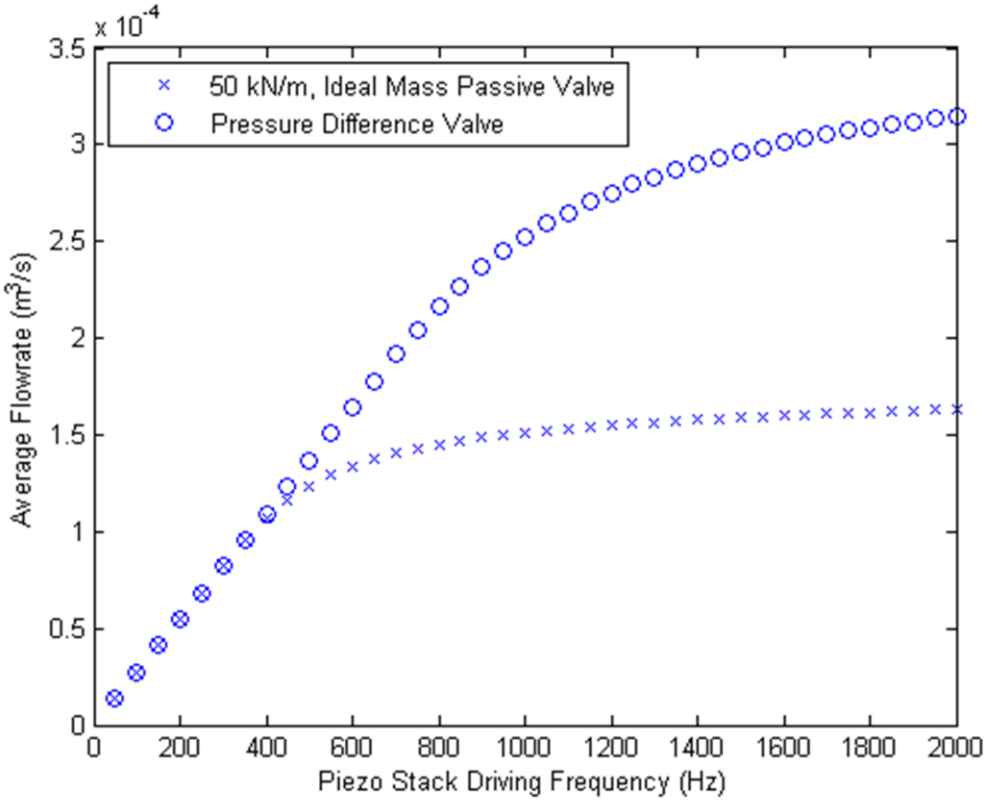

Figure 3.5 High response poppet valve and pressure difference valve against frequency.

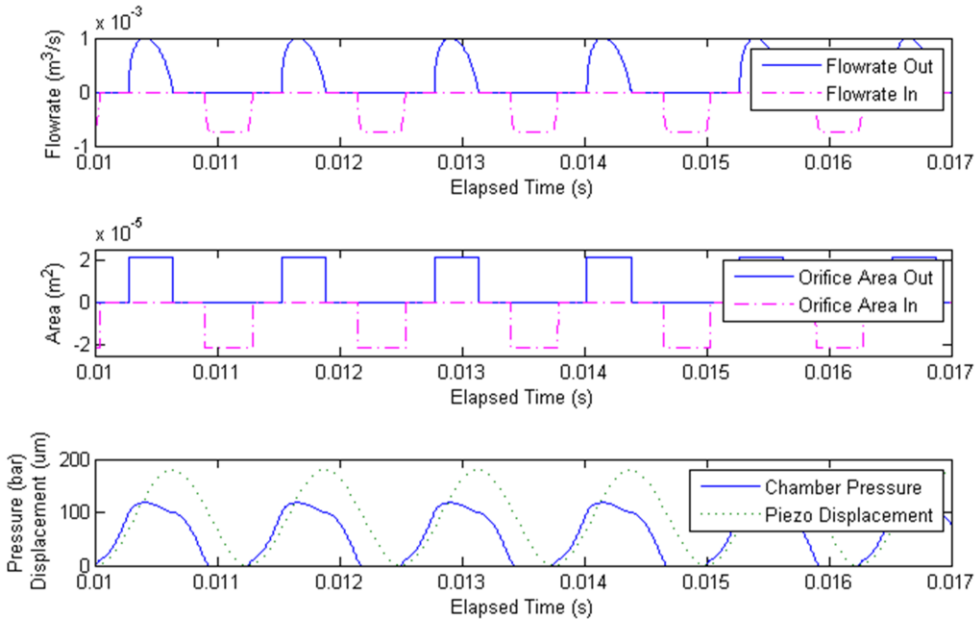

Figure 3.6 Instantaneous pressure difference valve at 800 Hz.

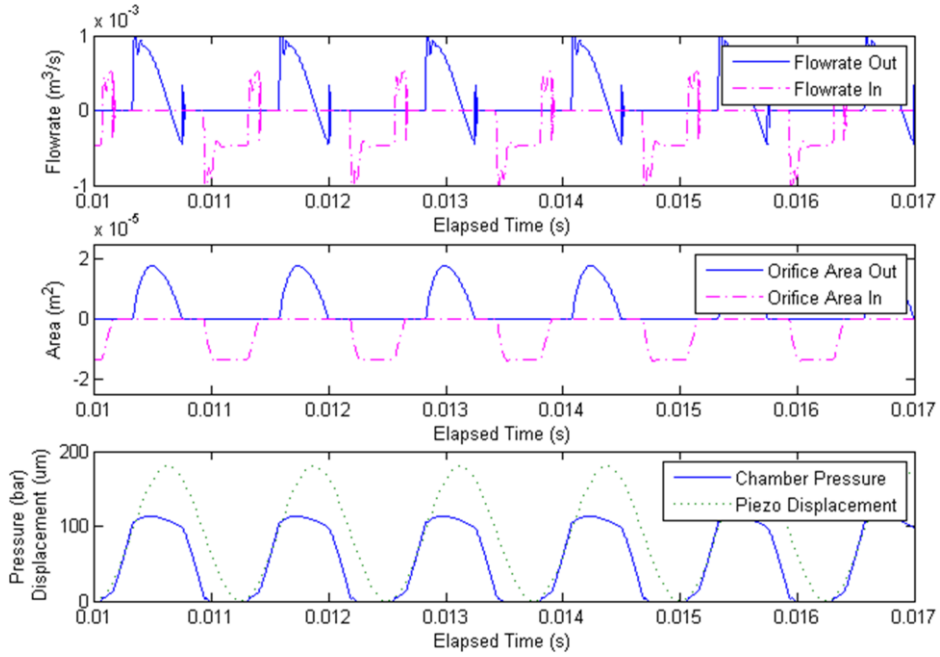

Figure 3.7 High response poppet valve with variable orifice and backflow at 800 Hz.

In the results presented, the parameter “downstream pressure”, which is the inlet pressure to the pumping chamber, is slightly restricting the flow rate from the piezo pump. It can be seen in the lowest sub plot in both Figure 3.6 and Figure 3.7 on retraction of the piezo stack the chamber pressure is reaching the cavitation limit, near zero pressure. Consequently the flow into the chamber is restricted by the difference between inlet pressure and the minimum chamber pressure. The piezo pump effectiveness would increase if the inlet pressure was raised to the point where the chamber pressure did not cavitate.

Simulations for the default parameters were run with the average flow rate versus driving frequency for valve spring stiffness of 5 kN/m to 100 kN/m. The average flow rate against pumping frequency is shown in Figure 3.8, for a valve seat diameter is 10mm with 1 mm lift, valve mass of 1 g against a constant pressure load. The flow rate is approximately linear up to the order of 400 Hz, but declines for higher frequencies is similar to other researchers experimental and simulation results [47, 68] shown in Figure 2.3 in the literature review.

The resonant frequency of the passive poppet valves is given by:

$$f = \frac{1}{2\pi}\sqrt{\frac{k_{Sp}}{m_{Va}}} \qquad \textbf{(3.20)}$$

For a valve mass of 1 g spring stiffnesses of 5 kN/m and 50 kN/m will give resonant frequencies of 356 Hz and 1130 Hz respectively. For lower spring stiffnesses the variability in the flow rate in Figure 3. can be attributed to the driving frequency being near or over the valve resonant frequency. From Equation 3.20 it can be seen that for a given spring stiffness to obtain a high resonant frequency it is better to make the valve mass as low as possible.

If the spring is too stiff relative to the pressure difference across the valve and the valve area, the valve does not fully open, resulting in a decreased flow rate, which explains the very stiff spring trends seen in Figure 3.8.

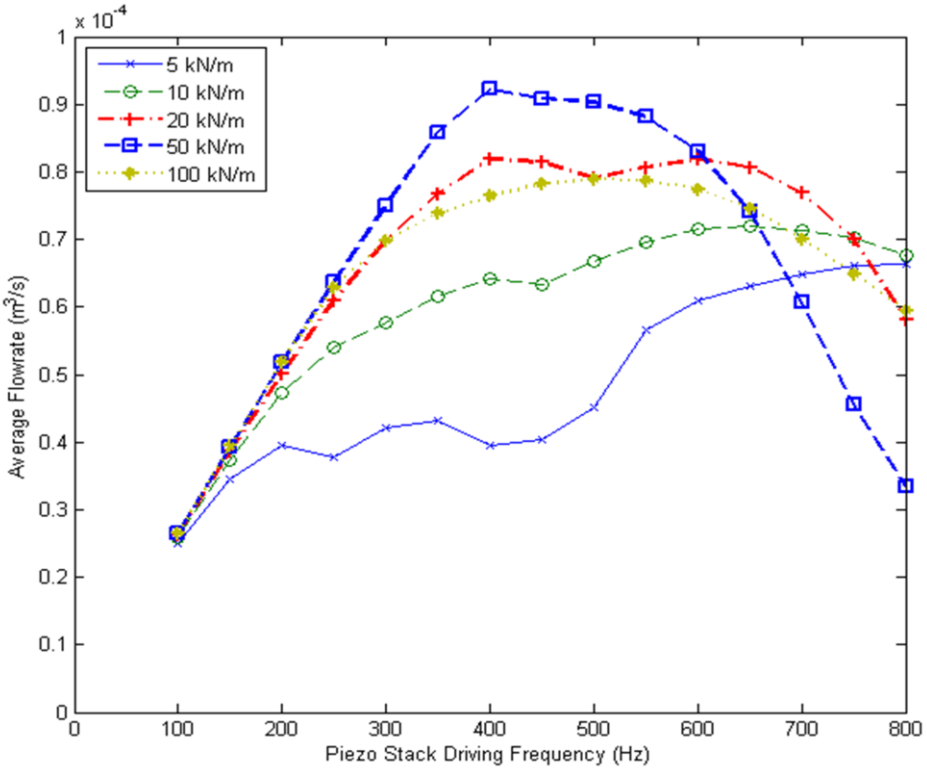

Figure 3.8 Pumping chamber flow for range of valve spring stiffness.

Three spring stiffness and driving frequency cases were chosen for further investigation; first, the optimal spring and frequency, which is a 50 kN/m spring and a driving frequency of 400 Hz, secondly a weak spring at the same frequency, which is a 5 kN/m spring and a driving frequency of 400 Hz , and third a stiff spring at a higher frequency, which is a 50 kN/m spring s and a driving frequency of 800 Hz. Flow into and out of the pumping chamber, valve openings and chamber pressure are shown over several pumping cycles for the three cases in Figure 3.9 to Figure 3.11.

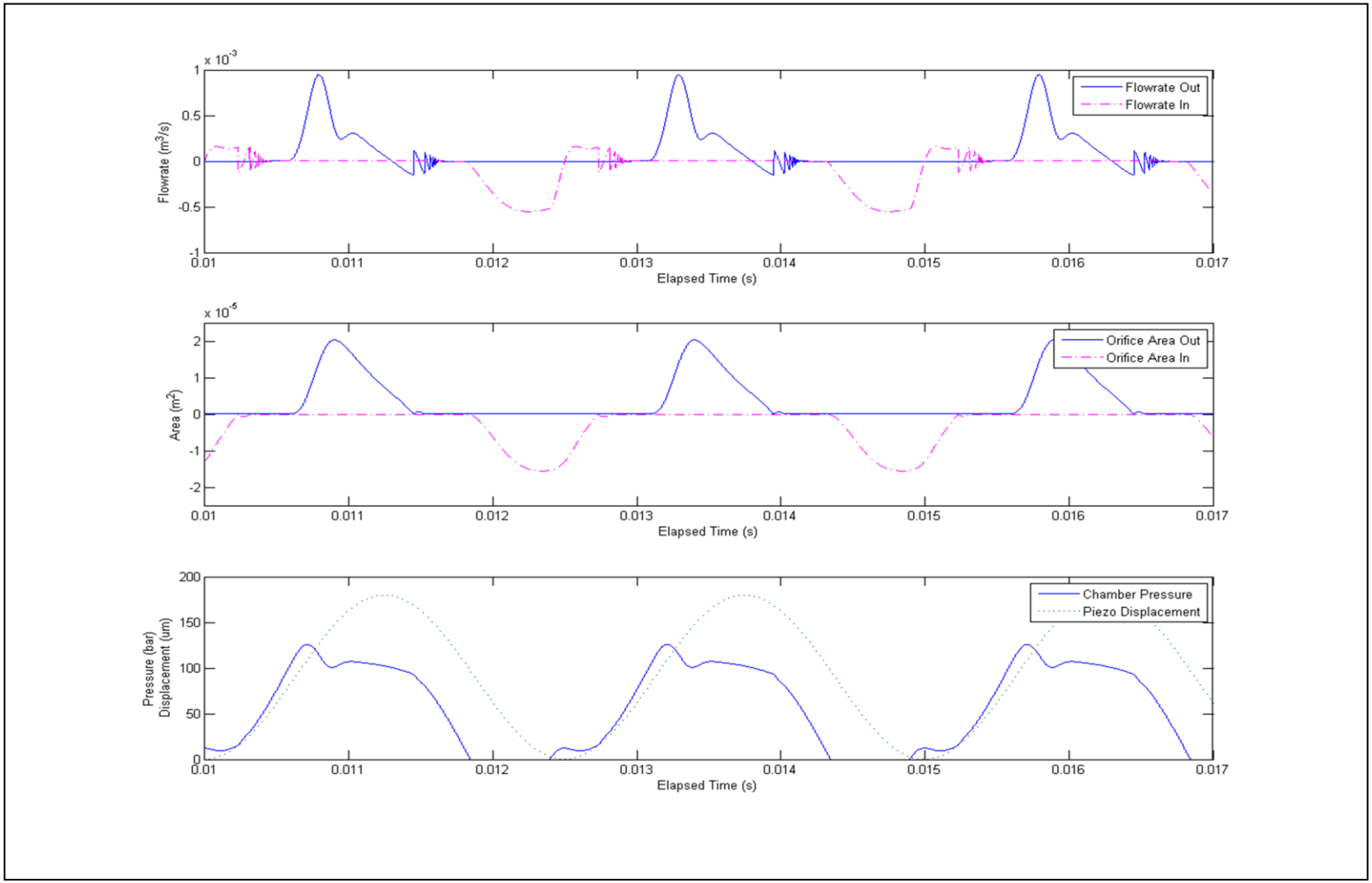

Figure 3.9 Chamber flows, valve openings, and chamber pressure for 50 kN/m valve at 400 Hz.

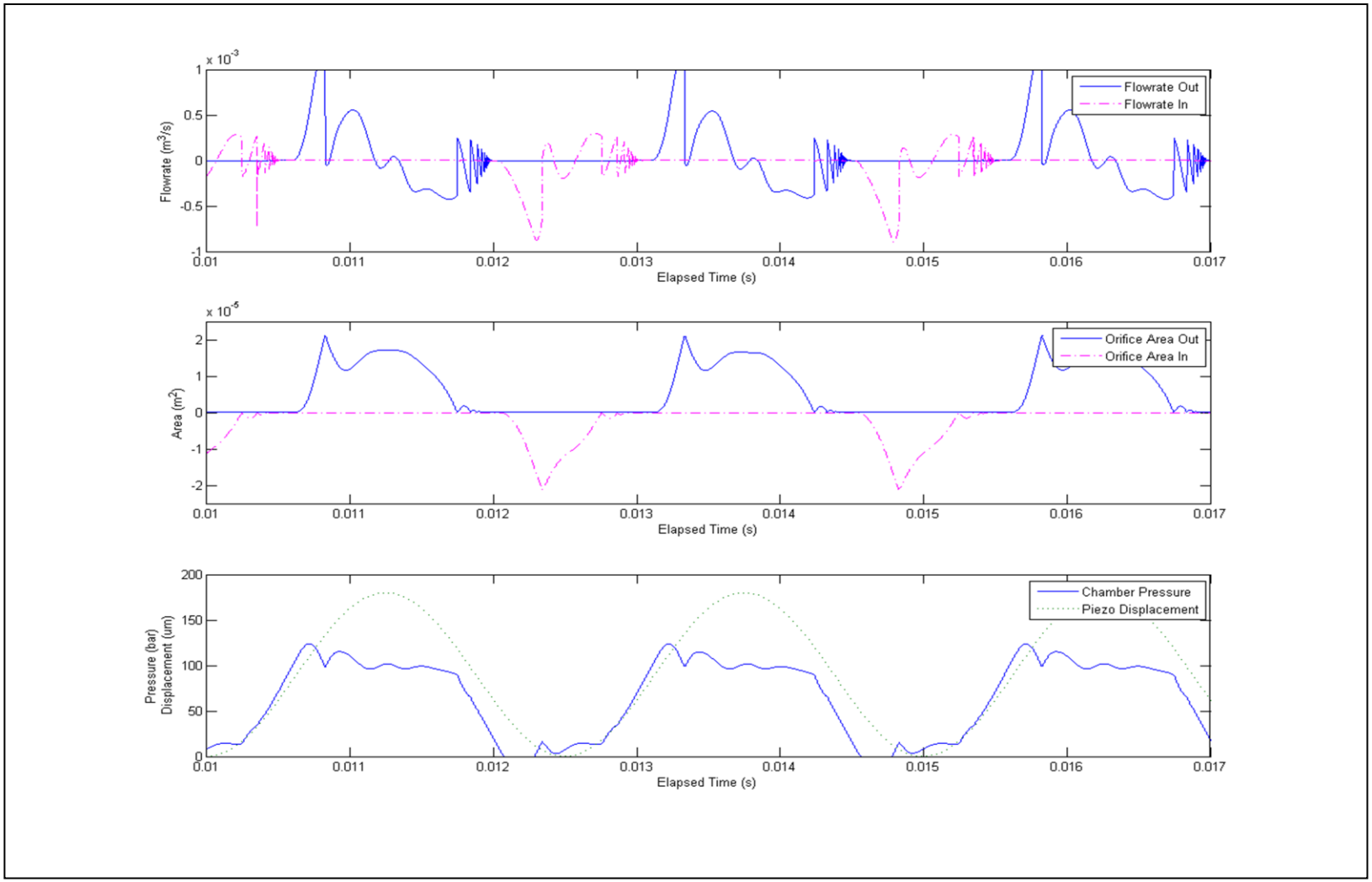

Figure 3.10 Chamber flows, valve openings, and chamber pressure for 5 kN/m valve at 400 Hz.

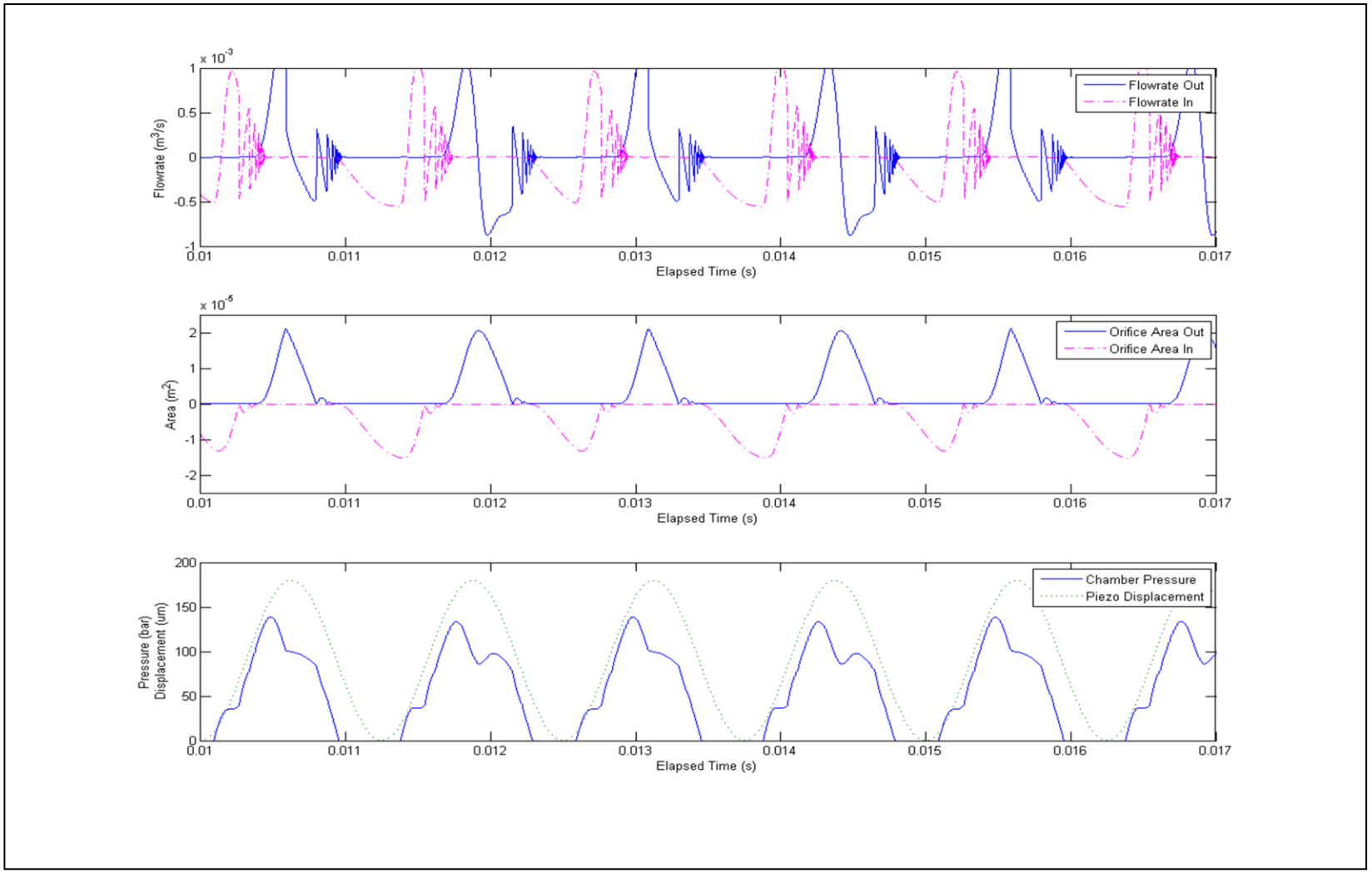

Figure 3.11 Chamber flows, valve openings, and chamber pressure for 50 kN/m valve at 800 Hz.

To investigate the flow rate dependence on valve area the simulation was run to determine the average flow rate versus a range of valve diameters, and therefore valve opening areas, for spring stiffness of 5 kN/m to 100 kN/m, with all other parameters held constant is shown in Figure 3.2. Using the ideal flow equation, Equation 3.1, for a 100 bar load the maximum displacement is 116 μm, the piston area and the 400 Hz driving frequency a maximum ideal linear flow of $12x10^{-5}$ m^3/s (7.2 lpm) is found. Figure 3.2 shows that increasing the valve diameter and matching the spring stiffness is beneficial to improve flow rate until close to the limit of the maximum ideal flow is reached.

As the valve diameter and therefore area are increased the spring stiffness proportionally has to be increased to obtain maximum flow rate. Figure 3.2 is constructed under the supposition that valve mass is fixed for all valve seat diameters, but in reality minimising poppet mass while creating an adequate orifice opening is not trivial and an increase in valve size will increase the added mass of displaced fluid.

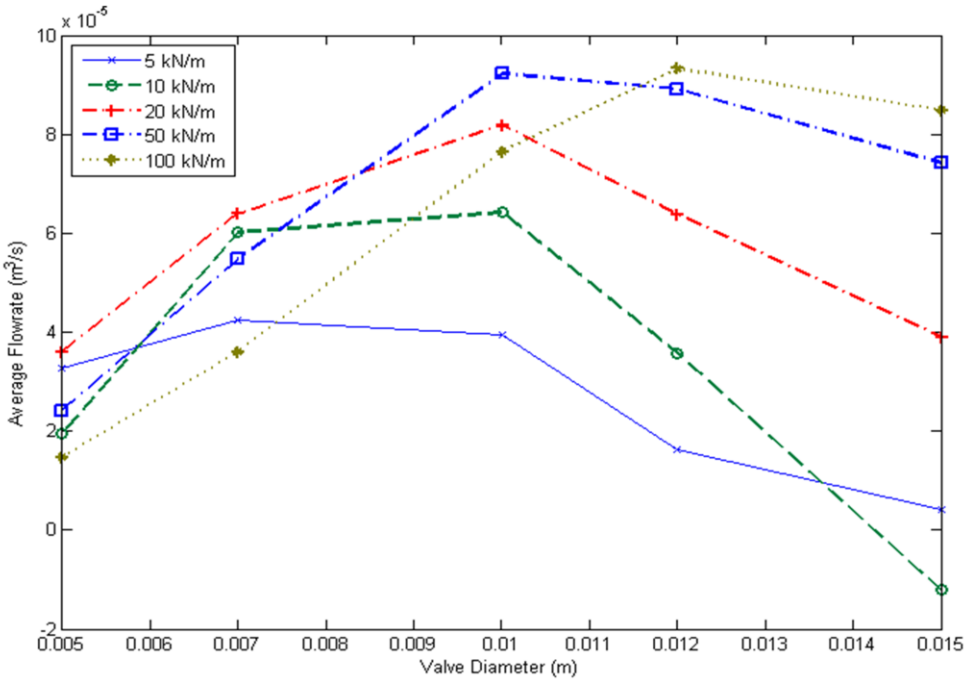

Figure 3.12 Chamber flow rate at 400 Hz against valve diameter for valve springs 5 kN/mm to 100 kN/mm.

3.3.2 Piezo Pump Application Feasibility

3.3.2.1 Piezo Pump Flow Rate Against Upstream Pressure

The flow rate versus upstream pressure simulation results for the piezo pump with the poppet valve model, and the actuator load demand for the AW 101 scale application where the cylinder is pushing against a 100kN/mm spring is shown in Figure 3.13. It can be seen that according to the model pressure and flow requirements could be attained with carefully selected spring stiffness, valve area and valve mass parameters.

The actuator would work directly in parallel with the strut and would be expected to deliver a peak force of the order of 35 kN, and have a peak velocity of 40 mm/s. If a hydraulic actuator with a net equivalent diameter of 56 mm (area of 2.5×10^{-3} m^2) is used, then a peak pressure of 150 bar, and a peak flow rate of 0.86×10^{-4} m^3/s is required (5.2 lpm), as shown in Figure 3.13.

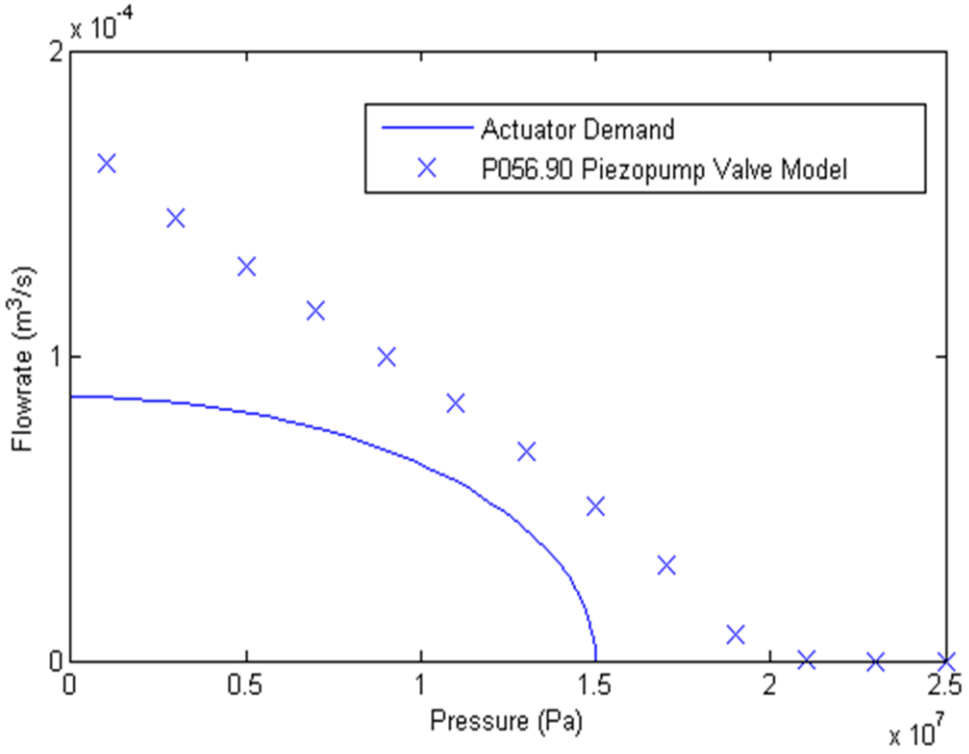

Figure 3.13 Average flow rate from pumping chamber versus upstream opposing pressure.

Although in Figure 3.13 the average flow rates appear able to be met at the range of pressures demanded, and valve dynamics are believed to determine the dominant characteristics of the piezo pump caution should be applied to the results due to the following secondary issues which will further lower the practically obtainable flow rate:

i. Piping friction and the bidirectional valve losses have been neglected.

ii. Inertia of the fluid in pipes has not been included.

iii. Resonances or anti-resonances due to pipe lengths can occur.

iv. Vortex formation in the pumping chamber and valve contractions have been shown by other authors [47, 48] to be present but is not taken into account here.

Two further issues relating to practical implementation of the piezo pump, namely the piezo current demand and device temperature rise at high frequency are important and are discussed in the next two sections.

3.3.2.2 Current Demand from Amplifier

Treating the piezo stack as a capacitive load the peak AC current demand from the amplifier is:

$$I_{Peak} = 2\pi fCV \tag{3.21}$$

where C is the actuator capacitance, and V is the driving voltage amplitude. Using Equation (3.21) for a AW101 scale rotorcraft; the capacitance of the largest commercially available stack from the company PI instruments; the P-056.90P, is 21000 nF, and driving at a frequency of 400 Hz at 0 to 1000 volts gives a peak demand current of 26 amps. The peak current is an order of magnitude higher than standard for even large commercially available amplifiers.

The scalability of the piezo stack current demand for a range of rotorcraft sizes was investigated, with the results shown in Appendix B, and it was found that only in much smaller rotorcraft than considered here could the current demands, and therefore amplifier sizes begin to look feasible.

3.3.2.3 Temperature Rise in Piezoelectric Stack

The temperature rise (in K) of an actuator can be estimated from [69] by the expression:

$$\Delta T = \frac{Uf v_{Ac}}{k(T)A} \tag{3.22}$$

where U is the hysteretic loss per unit volume per cycle, v_{Ac} is the active volume of the piezo stack, A is the heat transferring surfaces of the piezo stack, and $k(T)$ is the overall heat transfer coefficient. A steady state 100% duty cycle is implied. Using free convection the temperature rise in the piezo stack is from 89°C in the smallest considered rotorcraft to 140°C in the largest. As a worked example of the stack temperature rise for the largest scale rotorcraft, using a loss per cycle of 5 kJm^{-3} [69], driving frequency of 400 Hz, taking a solid to liquid heat transfer coefficient of 200 Wm^{-2}, and the P-056.90P piezo stack the cylindrical surface area and volume of $29x10^{-3}$ m^2 and $4.2x10^{-4}$ m^3, results in a temperature rise of 140°C.

The maximum operating temperature of the lead zirconium titrate (PZT) materials used in the P-056.90P piezo stack is approximately 150°C. The combination of a high ambient temperature (for example the maximum operating temperature of 120°C, see Appendix A) and the temperature rise would put the material temperature above the permissible maximum. Either forced convective cooling or liquid cooling of the device are possible, but the extra energy required and the added mass of the cooling equipment indicate other systems should be preferentially pursued.

3.4 Piezo Pump Conclusions

For a piezo pump careful consideration of the operating frequency and valve resonant frequency has to be taken otherwise the flow output of the piezo pump device can be extremely low. The temptation to increase operating frequency to increase pump output has been confirmed only to hold true up to frequencies in the order of 400 Hz. Valve size and therefore orifice area has to be adequate in order not to prohibitively restrict flow. Spring stiffness and valve mass need to be simultaneously optimised for the area of the valve. Further secondary modelling including vortex formation in the valves should also be investigated. Although the model in principle indicates a piezo pump is possible for this application the high current demand and high temperature rises for large continuously operated piezo stacks suggest care should be taken when deciding to use a piezo pump.

The feasibility of the piezo pump for the VIREA project therefore appears limited, however if the potential of the device is considered beyond the scope of this project there are two positive conclusions that can be drawn from the results. The first conclusion is that the piezo pump actuator appears more promising with smaller scale applications that use a small piezo stack which would have a low capacitance and a small volume to area ratio. The second conclusion is that applications that require an intermittent power, or low duty cycles are suited to the piezo pump actuator. Ideally, an application where short power demands are required, then the device is left to cool to ambient temperature show promise.

The following chapters in the thesis investigate devices built around electromagnetic actuation.

Chapter 4
Resonant Electro Hydrostatic Actuator

The selection of an electromagnetic actuator design, a description of Resonant EHA modelling, initial simulation results, and a description of device design iterations are given in this chapter.

4.1 Electromagnetic Device and System Selection

Electromagnet actuators considered for vibration suppression utilise gearing to convert long stroke low force motion into short stroke high force motion. Figure 4.1 illustrates the four major device architectures available for electromagnetic actuators with gearing. To achieve constant utilisation of the electromagnets rotary motors were considered preferable to linear motors. Although not directly relevant for the proof of concept device the final actuator will have to maintain performance with a 10000 hour lifetime which at 20 Hz is in the order of 700 million cycles. Both mechanical and hydraulic gearing have concerns with meeting the projected lifetime but hydraulic gearing was chosen to be investigated due to integral lubrication within the device, and the ability to obtain a high (30:1) single stage gearing ratio.

In any electrically powered device heating issues will invariably occur from transmission losses. A critical difference between a self-contained electrical actuator and the current hydraulically powered actuator is that waste heat will not be carried away from the actuator unless a separate cooling system is designed. If a separate liquid cooling system is not incorporated the electrical device will require a significant surface area.

Linear Motion Mechanical Gearing	**Linear Motion Hydraulic Gearing**
Rotary Motion Mechanical Gearing	**Rotary Motion Hydraulic Gearing**

·**Figure 4.1 Selection matrix of electromagnetic device architectures.**

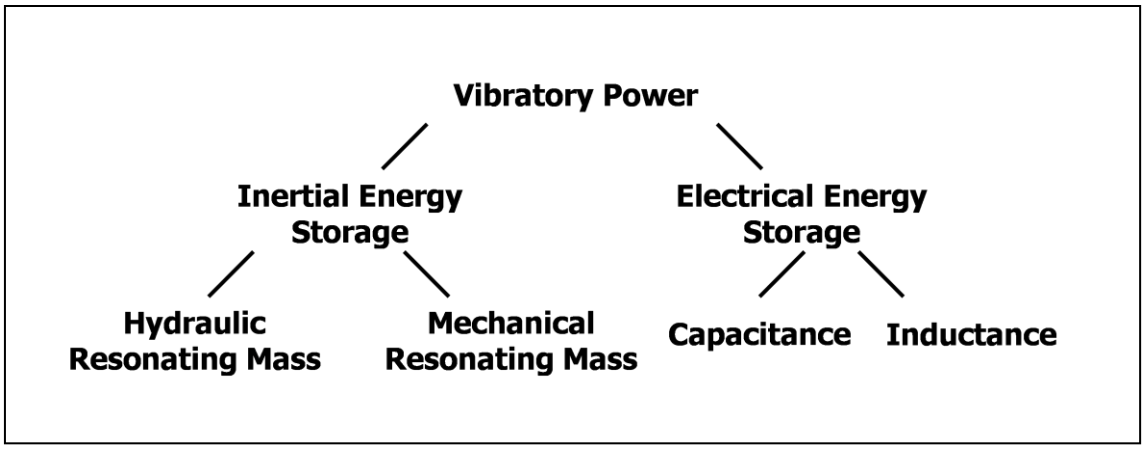

Figure 4.2 Selection tree of methods to store and return power from forced vibration.

It is therefore important to design the electrically powered device from the basis of minimising waste heat. Designing the device to absorb energy for half a cycle and output energy for the other half is a means for reducing the external electrical power demand, and is the basis for passive isolation. Figure 4.2 shows options on where the energy could be stored. Storing a small amount of energy in the electrical servo drive capacitors is possible, but kinetic energy will be the principle storage method used here, as mechanical to electrical conversion losses will then be minimised.

As opposed to a high power demand active system, a hybrid system will reduce the power requirement of the actuator. As stated in the literature review in Section 2.2 simple passive systems operate at a fixed frequency. Variable passive systems can shift the operating frequency; however they do not alter the magnitude of vibration isolation determined by their quality factor, while a hybrid system can. Hybrid systems also in principle allow the superposition of forces onto the fuselage, leading to vibration minimisation of all disturbance transfer paths, such as blade vortices impacting on the fuselage.

Hybrid actuators incorporating passive vibration isolation elements will have the advantage of working (in a reduced capacity) in the case of an external power supply failure. Hybrid systems may also have a relatively faster response time for changing load conditions compared to an active system in the condition transients generated by the change in load conditions die away

faster than an active control algorithm updates, although this needs to be verified. For these reasons a hybrid vibration system was chosen to develop on.

To illustrate the difference between an active system and a hybrid system, Figure 4.3 shows an actuator directly pushing against a spring, which is an active system, and an actuator assisting a resonating mass, which a hybrid system. The hybrid system can be said to be actively augmenting a passive system. In Figure 4.3 x is the displacement of the gearbox, c is the damping of the strut lumped with losses in the actuator, k is the strut stiffness. In the hybrid system in Figure 4.3 a and b are lengths that determine a linear mechanical gearing ratio. If instead of a mechanical gearing ratio, a hydraulic gearing ratio is used, and instead of a linear resonating mass, the solid mechanical rotor of an electric motor acts as the differential mass element, then the comparable system is shown in Figure 4.4. This combination of an EHA in parallel with a spring where the rotor inertia and hydraulic gearing ratio are sized to act as a passive vibration absorber is termed a Resonant EHA. In the Resonant EHA the gearing ratio is determined by the ratio pump displacement D to piston area A. Force F_{Ac} and torque T_{Mo} are the comparable force or torque inputs in Figure 4.3 and Figure 4.4 respectively. The linear resonating mass m_{Is} in Figure 4.3 is comparable to the electromagnetic motor rotor inertia I in Figure 4.4.

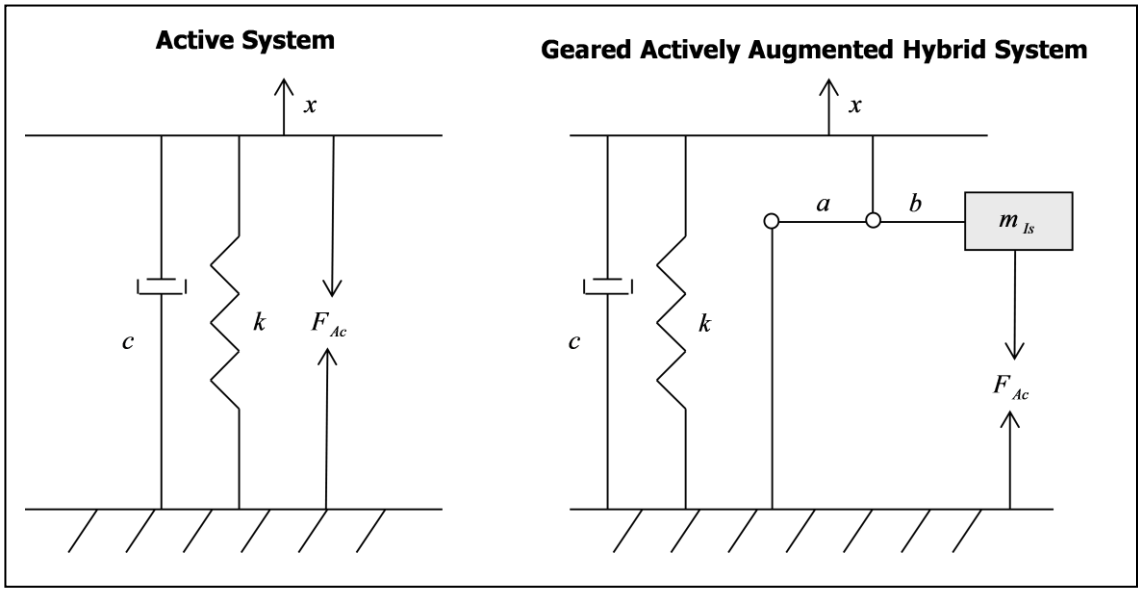

Figure 4.3 Active system compared to mechanically geared hybrid active-passive system.

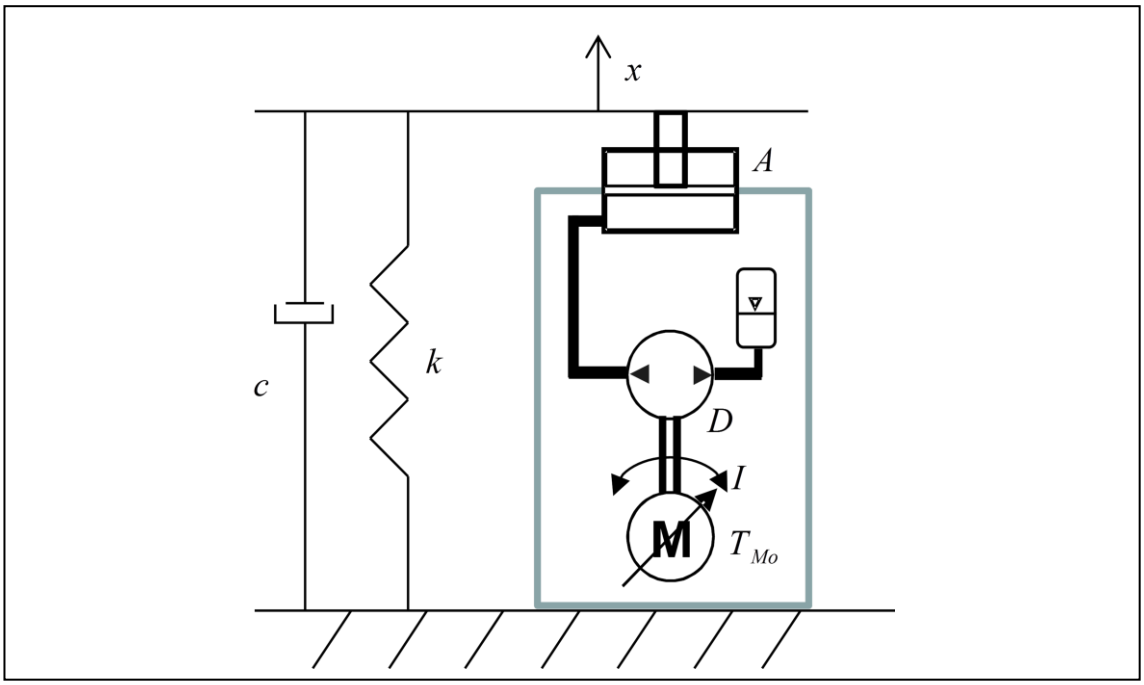

Figure 4.4 Schematic of Resonant EHA hybrid active-passive system.

Rotary motion of the passive resonating element was chosen due to the more volume and mass efficient use of electromagnets in a rotary motor than an axial motor for the same power output, the removal of the risk of stroke saturation for the resonating mass, and that semi-static deflection is automatically compensated for.

Figure 4.4 shows a hydraulic circuit suitable for a single acting single ended hydraulic cylinder. Using a single acting hydraulic cylinder to obtain bidirectional motion against a spring would require loading the spring with a constant torque from the pump. The constant torque in addition to the dynamic torque would require a greater size electric motor, therefore double acting hydraulic cylinders acting about a zero mean torque were considered preferable.

An EHA system (shown in Figure 4.4 and later in Figures 4.11 and 4.14) is controlled by a pump, compared to the original ACSR system which is controlled by a servo valve. The pump is rigidly attached to the electric motor rotor, where the dynamics of the rotor are determined both passively by the resonant frequency of the rotor, and actively by the magnitude, phase and waveform of the electric motors torque demand. The elimination of the servo valve allows the removal of restrictions from the system, so the system should be more efficient in terms of

having less components dissipating energy. The ACSR system is a hydraulic system where leakage is returned to a central tank, in contrast in an EHA, where the word hydrostatic implies the construction of a self-contained system. Each strut is individually powered by electrical servo drives, therefore the ability to eliminate the central shaft driven hydraulic power pack would be a benefit from this system

With reference to Figure 4.4, most modelling presented in this thesis compares a sinusoidal displacement input "x" on one side of the isolator and spring with a resulting net force measured at the "ground". A displacement input and force output matches what was experimentally performed on the physical device, and was therefore used. For functional vibration isolation the struts connecting the gearbox/blades to the fuselage of a helicopter can be viewed as being perfectly flexible at the specified frequency and associated harmonics while being rigid at all other frequencies. If the struts are considered to have zero stiffness at the specified frequency, the driven gearbox will be free to move, and if considered as a lumped mass, have rigid body motion at the specified frequency. The actuator's 350 um target dynamic stroke was derived from measured flight test data at maximum forward velocity, a common high demand condition. Instead of a displacement input "x", a mass representing one quarter the gearbox and a sinusoidal force input representing the aerodynamic loading from the blades also could be used in modelling. It is suggested that future modelling describes the strut and vibration suppression device as being mounted between two masses, one mass representing one quarter the gearbox having a force input, and the other being one quarter the fuselage where subsequent displacement or acceleration is measured (and minimised). Further considerations closer to implementation of the vibration suppression device in the rotorcraft should include the stiffness of the fuselage mounting points, and the check interactions between all four struts, however these models are outside the scope of this thesis.

The parameters affecting performance of the Resonant EHA will be investigated through modelling in the following sections, Section 4.2 to Section 4.4.

4.2 Resonant EHA Lumped Element Models

In this thesis a non-standard measure of the degrees of freedom in a model is given, specifically when a fixed displacement input is used. "Zero" degrees of freedom indicates the resonating mass is rigidly connected with infinite stiffness to the displacement input, and a "Single" degree of freedom indicates there is relative movement between the displacement input and the resonating element motion.

4.2.1 Zero Degree of Freedom Model

In a zero degree of freedom initial model, to evaluate the equivalent mass of the electric motor rotor inertia first the flow between the piston and the hydraulic motor is taken to be conserved:

$$v_{Ro}A = D\omega_{Mo} \tag{4.1}$$

where v_{Ro} is the velocity of the piston and A is the area of the piston, D is the volumetric displacement of the pump, and ω_{Mo} is the rotational velocity of the motor. Secondly the pressure at the pump is equated to the pressure at the piston:

$$\frac{F_{Cy}}{A} = \frac{T_{Mo}}{D} \tag{4.2}$$

where T_{Mo} is the motor torque, and F_{Cy} is the force on the cylinder. Using the above equations and Newton's Second Law, the equivalent mass m_{Eq} of the device, is found to be:

$$m_{Eq} = \frac{A^2}{D^2} I \tag{4.3}$$

where I is the combined electric and hydraulic motor inertia. Therefore the equivalent mass of the device is the rotating inertia multiplied by a gearing ratio squared.

Using the equivalent mass of the rotating parts, a diagram of the forces on the rotor and fuselage can be constructed, as shown in Figure 4.5.

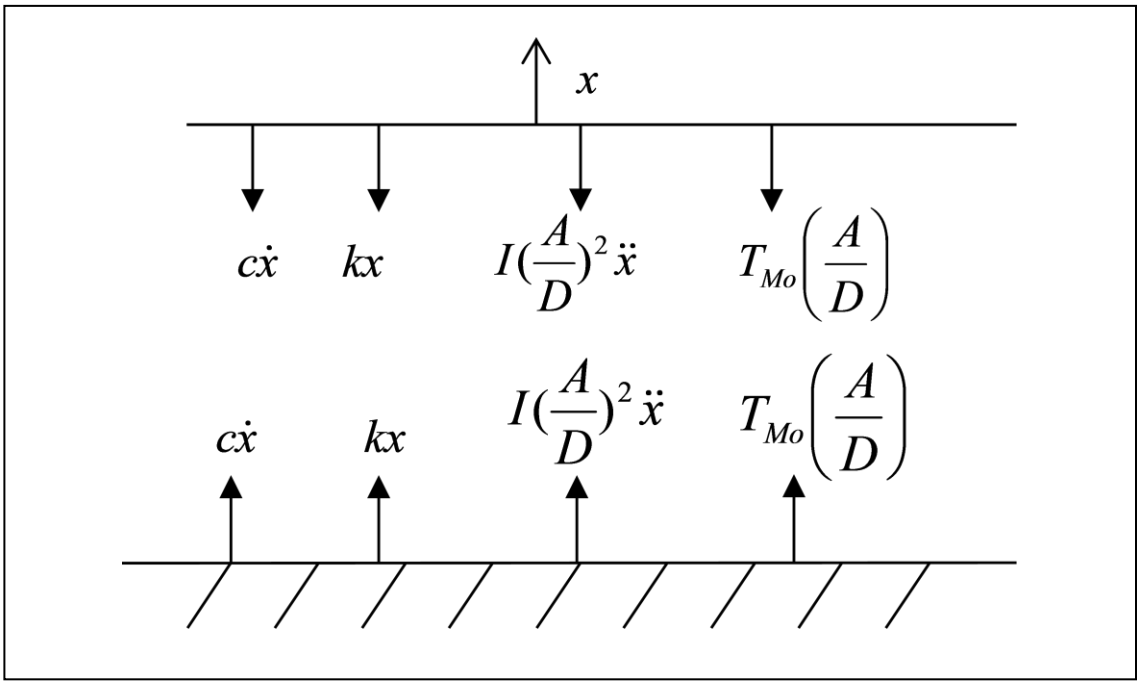

Figure 4.5 Zero degree of freedom model forces on fuselage.

The sum of forces on the fuselage F_{Fu} for a Resonant EHA is:

$$(\frac{A}{D})^2 I\ddot{x} + c\dot{x} + kx + T_{Mo}(\frac{A}{D}) = F_{Fu} \quad \textbf{(4.4)}$$

A transfer function relating the torque required to set the fuselage force to zero to the displacement input can be obtained:

$$\frac{T_{Mo}(s)}{X(s)} = -(\frac{D}{A})\left((\frac{A}{D})^2 Is^2 + cs + k\right) \quad \textbf{(4.5)}$$

The passive transfer function is:

$$\frac{F_{Fu}(s)}{X(s)} = (\frac{A}{D})^2 Is^2 + cs + k \quad \textbf{(4.6)}$$

The frequency at which the inertial and spring forces are in anti-phase is:

$$f = \frac{1}{2\pi}\frac{D}{A}\sqrt{\frac{k}{I}} \quad \textbf{(4.7)}$$

4.2.1.1 Zero Degree of Freedom Model Discussion

Analysis of torque to displacement transfer function, Equation 4.5, reveals the motivation for the development of the hybrid device; specifically, that the torque input at the frequency where the rotor inertia force opposes the spring stiffness force no motor torque input is required to directly deform the strut. Instead, the torque input is a function of both the damping, and how far from the resonant frequency the device is being used. Equation 4.5 also shows one factor in achieving a compact design of the passive vibration isolation components is a sufficiently high gearing ratio, as the required resonating inertia, which dictates the mass and volume of the system, is divided by the gearing ratio squared. Transmission stiffness in the zero degree of freedom model is taken as infinite, therefore in the next section the model is improved to investigate the influence of transmission stiffness as a result of hydraulic oil compressibility.

4.2.2 Single Degree of Freedom Model

The Resonant EHA model is updated to include the transmission stiffness, which relates to the bulk modulus of the pressurised hydraulic fluid. Figure 4.6 shows a passive linear analogy of the linear to rotational single degree of freedom model used.

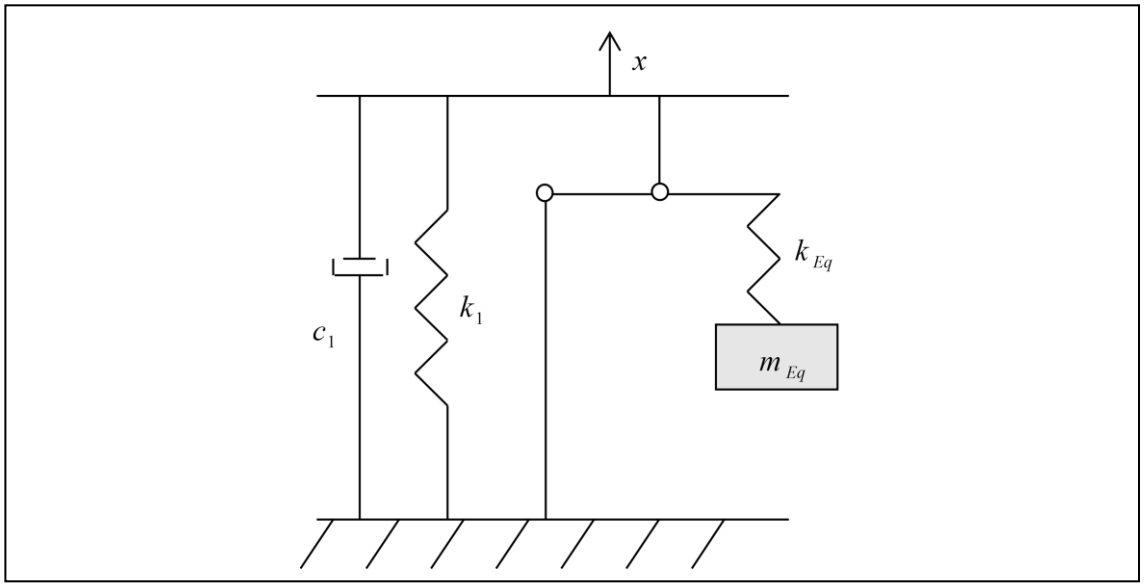

Figure 4.6 Linear analogy of single degree of freedom model.

The single degree of freedom model for a Resonant EHA is as follows. The sum of forces on the fuselage as a function of the driven displacement x and pump angle θ is:

$$c_1\dot{x} + k_1 x + \frac{A}{D}(k_2(\frac{A}{D}x - \theta)) = F_{Fu} \quad \textbf{(4.8)}$$

k_2 is the pump torsional stiffness given by:

$$k_2 = \frac{2BD^2}{V_{To}} \quad \textbf{(4.9)}$$

where V_{To} is the total of volume of fluid between the pump and piston on one side of the pump. The equation of motion of the motor is:

$$k_2(\frac{A}{D}x - \theta) - T_{Mo} = I\ddot{\theta} + c_2\dot{\theta} \quad \textbf{(4.10)}$$

where c_2 is the pump and motor torsional damping. Substituting in for θ in Equation (4.8) and transferring to the s domain gives:

$$F_{Fu}(s) = \left((\frac{A}{D})^2 \left(\frac{Is^2 + c_2 s}{\frac{I}{k_2}s^2 + \frac{c_2}{k_2}s + 1} \right) + c_1 s + k_1 \right) X(s) + \left(\frac{\frac{A}{D}}{\frac{I}{k_2}s^2 + \frac{c_2}{k_2}s + 1} \right) T_{Mo}(s) \quad \textbf{(4.11)}$$

The transfer function for obtaining zero net force on the fuselage is:

$$\frac{T_{Mo}(s)}{X(s)} = -(\frac{D}{A})\left(\frac{c_1 I}{k_2}s^3 + \left((\frac{A}{D})^2 I + \frac{c_2 c_1}{k_2} + \frac{k_1 I}{k_2} \right)s^2 + \left(\frac{c_2 k_1}{k_2} + c_1 + c_2(\frac{A}{D})^2 \right)s + k_1) \right) \quad \textbf{(4.12)}$$

which when k_2 goes to infinity reduces to the zero degree of freedom transfer function given in Equation (4.5). The transfer function for passive vibration isolation is:

$$\frac{F_{Fu}(s)}{X(s)} = (\frac{A}{D})^2 \left(\frac{Is^2 + c_2 s}{\frac{I}{k_2}s^2 + \frac{c_2}{k_2}s + 1} \right) + c_1 s + k_1 \quad \textbf{(4.13)}$$

4.2.2.1 Zero and Single Degree of Freedom Model Comparison

A series of comparisons between the zero degree of freedom model and the single degree of freedom model using equivalent damping values is undertaken with the parameters in Table 4.1. The damping in the device using the zero degree of freedom model was taken as:

$$c = \zeta 2\sqrt{k m_{Eq}} \qquad \textbf{(4.14)}$$

where ζ is the damping ratio. The nominal basis of parameter selection was representative of a 2 tonne rotor craft with a blade passing frequency of 25 Hz and a damping ratio of 0.3. Using Equation 4.5 and Equation 4.12 the active torque required to set the fuselage force to zero near the target frequency is shown in Figure 4.7.

Table 4.1 Zero and single degree of freedom model parameters.

Parameter	Value
Strut stiffness k , k_1	20 kN/mm
Piston area, A	550 mm^2
Motor displacement, D	1.5 cm^3/rev
Combined inertia, I	$1.4x10^{-4}$ kgm^2
Zero degree of freedom damping (damping ratio of 0.3) , c	$7.3x10^4$ Ns/m
Single degree of freedom damping, linear , c_1	$3.7x10^4$ Ns/m
Single degree of freedom damping, rotary , c_2	$7x10^{-3}$ Nms/rad
Bulk modulus, B	900 MPa
Fluid volume, V_{To}	8.9 cm^3
Single degree of freedom rotary stiffness, k_2	11.5 Nm/rad

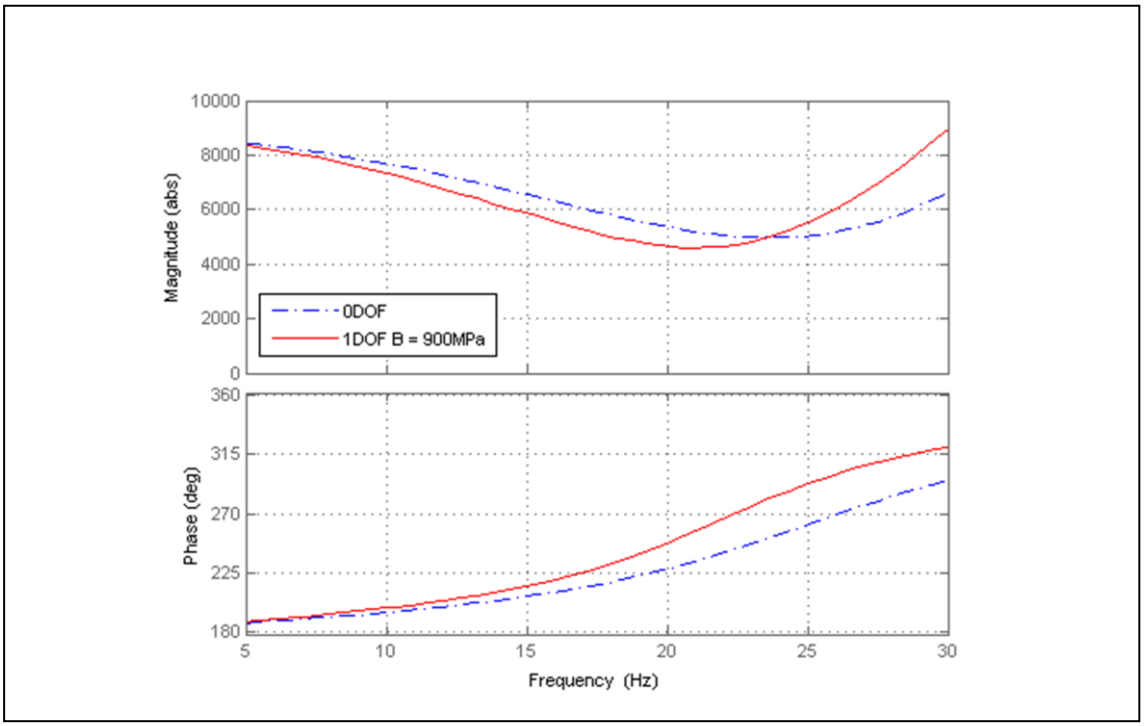

Figure 4.7 Torque required (Nm/m) to set fuselage force to zero for 5 Hz to 30 Hz.

From Figure 4.7 for similar damping values, the difference between the zero degree of freedom model with infinite stiffness and the one degree of freedom model with a suitable expected stiffness is slight, with the one degree of freedom model giving a lower minimum force frequency (21.0 Hz versus 24.2 Hz). Adequate transmission stiffness is dependent on a high fluid bulk modulus, and minimising the volume of fluid present.

The torque required to set the fuselage force to zero for the frequency range of 5 to 100 Hz is shown in Figure 4.8. Across the zero and one degree of freedom models there is a similar trend where the required torque magnitude rises with frequency after the passive isolation frequency. An example from the 900 MPa single degree of freedom curve in Figure 4.8 where the torque required at 42 Hz (magnitude of 22700 Nm/m) is five times greater than at 21 Hz (magnitude of 4600 Nm/m). Control of harmonics of a fundamental input is feasible for the same sized motor if the displacement inputs at the harmonics approximately decrease at the same rate as any increase in torque required.

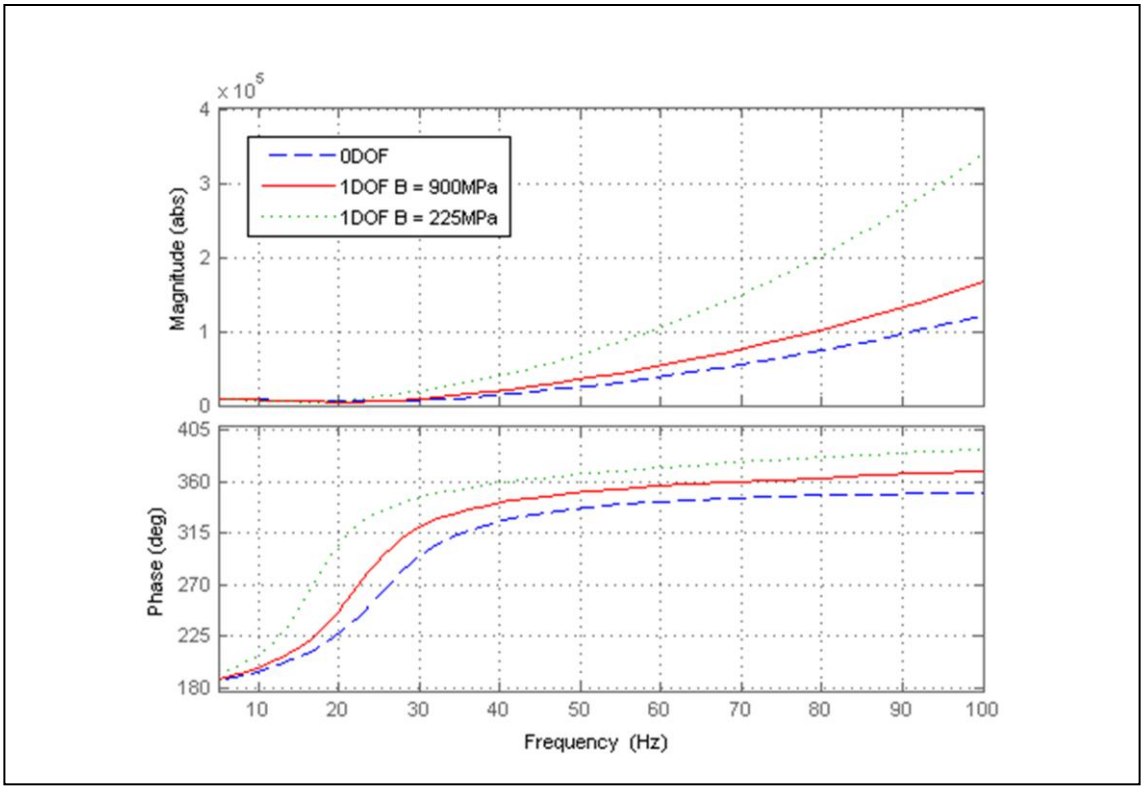

Figure 4.8 Torque required (Nm/m) to set fuselage force to zero up to 100 Hz.

The passive vibration transmission characteristics of the zero and one degree of freedom models up to 100 Hz are shown in Figure 4.9. The zero degree of freedom model predicts the transmitted force will rise with frequency. The single degree of freedom models show a distinct peak. The magnitude of the peak is determined by the damping in the system as well as the stiffness. Passively the effect of the peaks in the single degree of freedom model is to magnify inputs, such as the harmonics of a lower frequency fundamental input, which coincide with peak frequency. In this case due to the magnitude of the peak small input harmonics could become a significant transmitted passive force component.

The feasibility of a Resonant EHA as a vibration suppression system is examined using the zero degree of freedom model in the following section, Section 4.3.

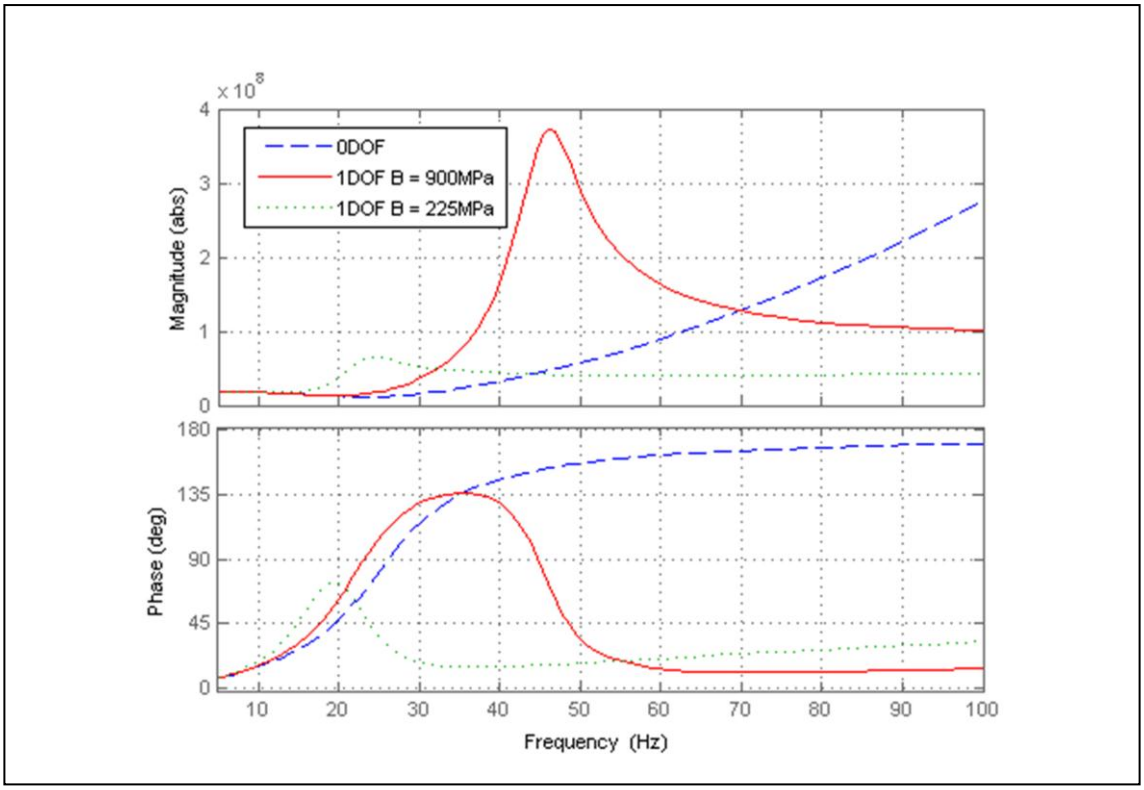

Figure 4.9 Passive fuselage force (N/m) up to 100 Hz.

4.3 Resonant EHA Feasibility

For feasibility studies using the zero degree of freedom model the torque required for the AW101 scale helicopter at 90% of the fundamental target frequency and a damping ratios of 0.3 were found from Equation 4.5. The torque was in principle found to be able to be met without overheating by relatively compact commercially available brushless DC motors.

The ability of the Resonant EHA design to scale in size across a range of typical rotorcraft sizes is investigated here. The maximum permissible semi-static deflection of the gearbox under several g's manoeuvring can be taken as fixed, therefore the strut stiffness can be taken as relatively proportional to the mean take-off weight (MTOW) of the rotorcraft. If the motor torque at the fundamental frequency is determined by damping, as in Equation 4.5 where the equivalent resonating mass is designed to match the spring stiffness of the strut, the torque magnitude is approximately proportional to rotorcraft size assuming the device damping is constant across a range of device sizes. This relationship is shown in Equation 4.15:

$$T_{Mo} \propto c \propto \zeta k \propto \zeta m_{MTOW} \qquad \textbf{(4.15)}$$

Appendix C gives detail for the scalability comparison using a constant gearing ratio and variation in blade passing frequency with size, with the result being that the required torque and rotor inertia were found to be in principle feasible across all sizes of rotorcraft for current generation of commercially available brushless DC electric motors.

As results were expected to hold for a range of devices, rather than testing a large AW101 scale device a smaller "Light1" rotorcraft scale device representative of a 2 tonne rotorcraft with a blade passing frequency of 25 Hz was chosen for experimental testing. Experimental testing in this thesis will therefore refer to parameters relevant to the smaller Light1 scale proof of concept device. For the Light1 scale device the Bode plot of the transfer function between torque and displacement (Equation 4.5) for three damping coefficients is shown in Figure 4.10.

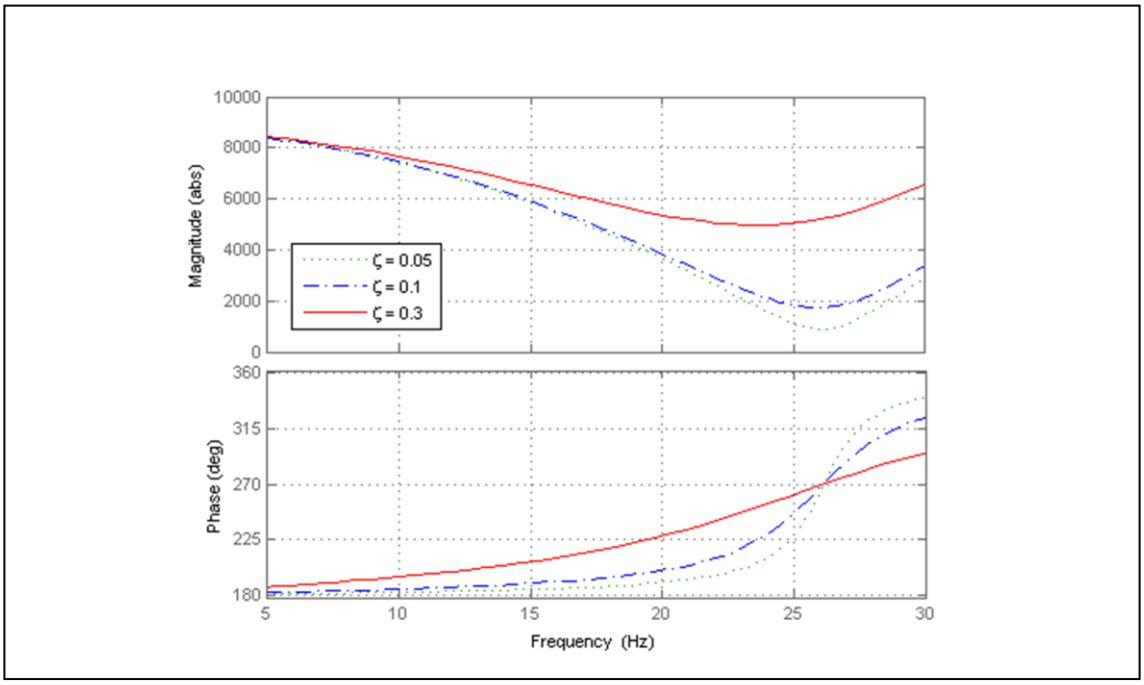

Figure 4.10 Torque required (Nm/m) to set fuselage force to zero for three damping levels.

In Figure 4.10 the damping coefficients were chosen to represent near ideal (0.05), optimistic (0.1), and more realistic (0.3) damping ratios. Using the zero degree of freedom transfer function for displacement amplitude of 0.35 mm and a damping ratio of 0.3 at 90% of the resonant frequency the torque input 1.9 Nm is found, confirming the possibility of using a relatively compact and low mass electric motor.

Non linearities such as leakage and piston friction are better to model with constituent equations, therefore the next section, Section 4.4, considers detailed physical models for two EHA hydraulic circuits.

4.4 Resonant EHA Physical Modelling

4.4.1 Refeeding Circuit Hydraulic System

A model of an open drain Resonant EHA including fluid compressibility, DC motor dynamics and hydraulic leakage is described in this section. The physical construction of hydraulic motors demands a shaft seal loose enough to permit rotation of the shaft, therefore the absolute pressure of the shaft seal is rated to before leaking is relatively low, in the order of several bar. To prevent fluid building up behind the shaft seal and the pressure rising beyond the seal rated pressure a case drain is fitted to the pump, resulting in external leakage. The external leakage of the pump was fed back into the low pressure line through the refeeding circuit consisting of a low pressure accumulator and check valves. The EHA simulation structure is similar to that reported by Kang et.al. [64]. The hydraulic system diagram of the Resonant EHA with refeeding circuit is shown in Figure 4.11 showing an electric motor, hydraulic pump, refeeding circuit and double ended cylinder.

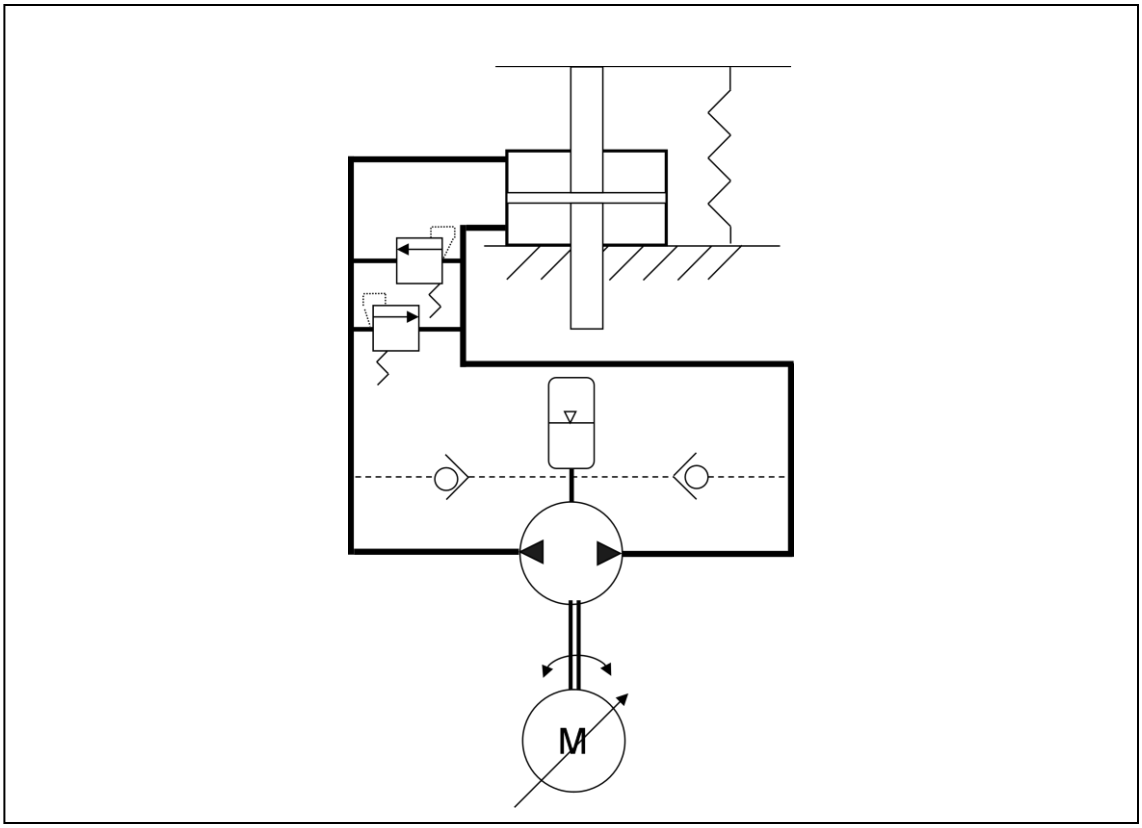

Figure 4.11 Resonant EHA hydraulic system with refeeding circuit.

The equations for each component of the EHA are as follows. The electrical motor is a brushless DC motor. The dynamic equations for a brushless DC motor are:

$$E_{mo} = K_C \omega + L\frac{di}{dt} + Ri \quad \textbf{(4.16)}$$

$$T_e = K_t i \quad \textbf{(4.17)}$$

$$T_e = I\dot{\omega} + c_{Sh}\omega + T_{ex} \quad \textbf{(4.18)}$$

where E_{mo} is the voltage input to the motor, K_C is the back electromotive force constant, L is the motor winding inductance, R is the motor winding resistance, i is the current input, T_e is the electromagnetic torque, K_t is the torque constant, I is the combined inertia of motor, shaft coupling and pump, c_{Sh} is the combined friction of motor and pump including shaft seal, T_{ex} is the load torque acting on the motor shaft, and ω is the rotational speed of the motor. The flow equations for fluid in lines either side of a hydraulic motor are:

$$Q_1 = D\omega - K_{Il}(P_1 - P_2) - K_{El}(P_1 - P_{Ac}) \quad \textbf{(4.19)}$$

$$Q_2 = D\omega - K_{Il}(P_1 - P_2) + K_{El}(P_1 - P_{Ac}) \quad \textbf{(4.20)}$$

where K_{Il} is the internal leakage coefficient of the pump, K_{El} is the external leakage coefficient of the pump, P_1 and P_2 are the pressures in each line, P_{Ac} is the accumulator pressure. The flow equations of the refeeding circuit are:

$$Q_{Ac} = Q_{El} - Q_{c1} - Q_{c2} \quad \textbf{(4.21)}$$

$$Q_{1f} = Q_1 + Q_{C1} \quad \textbf{(4.22)}$$

$$Q_{2f} = Q_2 - Q_{C2} \quad \textbf{(4.23)}$$

where Q_{Ac} is the flow to or from the accumulator, Q_{El} is the external leakage flow of the motor, Q_{C1}, Q_{C2} are the return flows governed by the poppet check valves described in the piezo pump valve Section 3.2.3. The accumulator is a flexible hose filled with hydraulic fluid and is modelled as:

$$\dot{P}_{Ac} = \frac{Q_{El} B_{Ef}}{V_{Ho}} \quad \textbf{(4.24)}$$

where B_{Ef} is the effective bulk modulus of the fluid in a flexible hose and V_{Ho} is the volume of the hose. The flow equations of fluid into and out of a double ended actuator are:

$$Q_{1f} = A\dot{x} + \frac{V_{1i} + Ax}{B}\dot{P}_1 + K_{Lc}(P_1 - P_2) \quad \textbf{(4.25)}$$

$$Q_{2f} = A\dot{x} - \frac{V_{2i} - Ax}{B}\dot{P}_2 + K_{Lc}(P_1 - P_2) \quad \textbf{(4.26)}$$

where x and $\dot{x}$ are the displacement and velocity of the piston which is rigidly connected to the gearbox, B is the bulk modulus of the oil, K_{Lc} is the internal leakage coefficient of the piston, V_{1i} and V_{2i} are the initial volume of chamber 1 and 2 plus fluid in the connecting pipes respectively. The balance of forces on the piston is:

$$A_P(P_1 - P_2) = F_{EHA} + F_{Fc} \quad \textbf{(4.27)}$$

where F_{EHA} is the force produced by the actuator. F_{Fc} is a Coulomb friction force acting on the piston which is either of the three states:

$$F_{Fc} = \begin{cases} F_{Mx} \; if \; c_{Cf}\dot{x} \geq F_{Mx} \\ c_{Cf}\dot{x} \\ -F_{Mx} \; if \; c_{Cf}\dot{x} \leq -F_{Mx} \end{cases} \quad \textbf{(4.28)}$$

where F_{Mx} is the friction absolute maximum value and c_{Cf} is a transitional friction coefficient.

The EHA sits in parallel with a linear stiff spring (the strut) that is attached to a displacement input (the gearbox) and ground (the fuselage, which in this simulation is fixed). The spring equation is:

$$F_{Sp} = kx \quad \textbf{(4.29)}$$

It is assumed the structural damping of the strut is negligible. The net force on the fuselage which should be minimised at the target frequency for one strut is:

$$F_{Ne} = kx - F_{EHA}(\dot{x}, \ddot{x}, i) \quad \textbf{(4.30)}$$

Leakage exiting the cylinder end seal and any dynamics of the relief valve lines are not believed to be important and are neglected.

4.4.1.1 Refeeding Circuit Resonant EHA Discussion

The refeeding circuit layout has the advantage of being simple to construct with readily available components, however the following three disadvantages are also present. First, the effective bulk modulus of a real fluid is a function of the entrained air content and the pressure. At higher mean pressures the bulk modulus of the fluid is higher, which is beneficial for the performance of the device. The low pressure side of the pump drops to a pressure set by the accumulator, which has to be typically less than 5 bar as a higher pressure in the housing of the pump would damage the shaft seal. With a 2% air content the effective bulk modulus of oil at 5 bar and 100 bar is 0.08 GPa and 1.35 GPa respectively. Therefore the low pressure side of the pump will have very low effective bulk modulus. Secondly, the ability of the refeeding circuit to prevent the low pressure line from cavitating is dependent on the performance of the check valves leading back into the circuit. Finally, the fluid returning to the circuit acts as a disturbance input which can excite higher frequency excitation modes. System parameter values are listed in Table 4.2.

Figure 4.12 shows the simulated net force on the fuselage for a refeeding circuit based model with a force input on the rotor mass equivalent to a 0.3 mm displacement for three cycles of the simulated net force on the fuselage. In Figure 4.12 although the fundamental frequency has been cancelled by a suitable torque input, higher frequency oscillations approaching a similar magnitude to the input force are seen, therefore as a vibration isolation system the RMS vibration suppression performance is poor. Figure 4.13 shows the source of the excitation; the pulse of fluid from one side of the refeeding circuit where the refeeding flow through the check joins the flow from the pump when the line pressure drops below the accumulator pressure. The 5th harmonic is the largest remaining Net Force waveform in Figure 4.12 due to the passive response's peak frequency, which varies with fluid stiffness, similar to than seen in Figure 4.9 using Equation 4.13, coinciding or being near the 5th harmonic's frequency.

Enclosing the electric motor and pump together in one package eliminates the need for a refeeding circuit, therefore an Enclosed EHA system is modelled in the next section, Section 4.4.

Table 4.2 Resonant EHA physical model nominal parameters.

Parameter	Value
Strut stiffness, k	20 kN/mm
Piston area, A	550 mm^2
Motor displacement, D	1.52 cm^3/rev
Combined inertia, I	$1.4x10^{-4}$ kgm^2
Back electromotive force constant, K_C	0.28 V(peak)/(rad/s)
Motor winding inductance, L	5 mH
Motor winding resistance, R	1.56 Ω
Torque constant, K_t	0.355 Nm/A
Friction and windage of motor and pump, c_{Sh}	2 mNm/(rad/s)
Internal leakage coefficient of pump, K_{Il}	$1x10^{-13}$ m^3/Pa
External leakage coefficient of pump, K_{El}	$1x10^{-13}$ m^3/Pa
System pressure, P_{Ac}	5 bar
Bulk modulus, B	80 MPa
Internal leakage coefficient of piston, K_{Lp}	$1x10^{-13}$ m^3/Pa
Initial volume of each chambers and connection , V_{1i} , V_{2i}	5.6 cm^3
Cylinder friction absolute maximum value, F_{Mx}	±700 N
Cylinder viscous friction coefficient, c_{Fc}	$15x10^3$ N/(m/s)

Accumulator volume, V_{Ho}	55 cm^3
Poppet valve seat diameter, D_{Va}	10 mm
Maximum poppet valve lift, x_{St}	1 mm
Nominal valve spring stiffness, k_{Sp}	10 kN/m
Nominal valve mass (including spring mass and added mass), m_{Va}	1 g
Poppet valve free damping ratio, ς_{Fr}	0.5
Poppet valve endstop damping ratio ς_{St}	0.1
Poppet valve endstop stiffness, k_{St}	1000 kN/m
Poppet valve preload, F_{Pr}	0 N
Poppet valve discharge coefficient, C_D	0.72
Poppet valve force coefficient, C_F	0.4
Poppet valve half angle, θ	45°
Vapour pressure, P_{Va}	1 bar

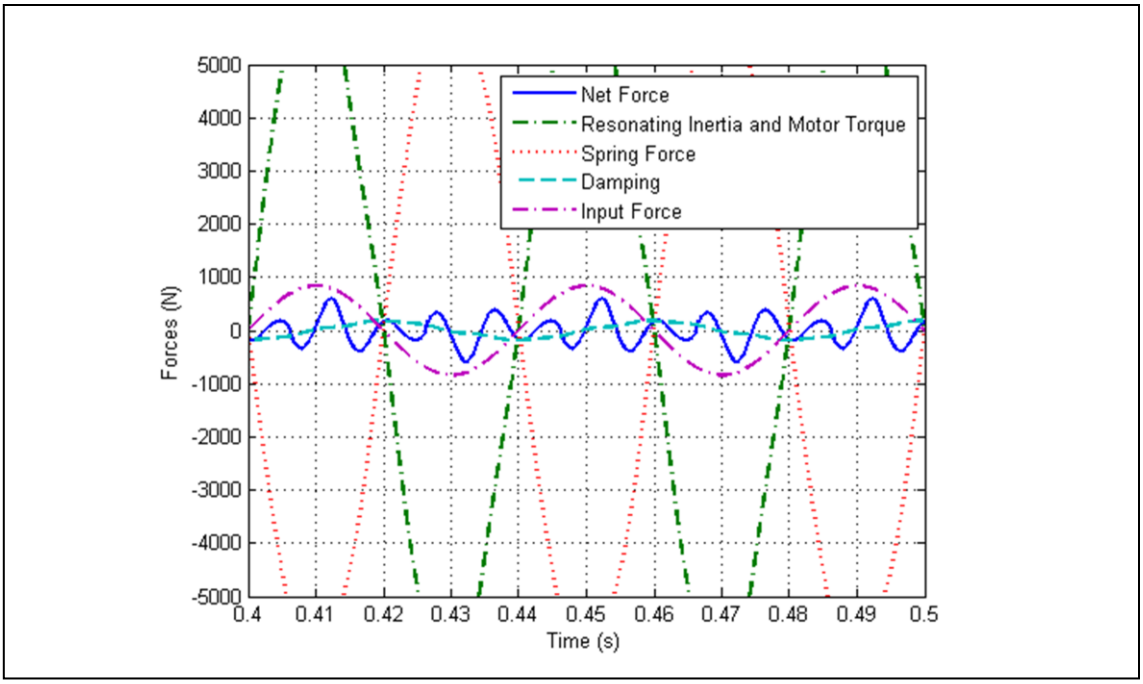

Figure 4.12 Fuselage force showing refeeding circuit induced disturbance.

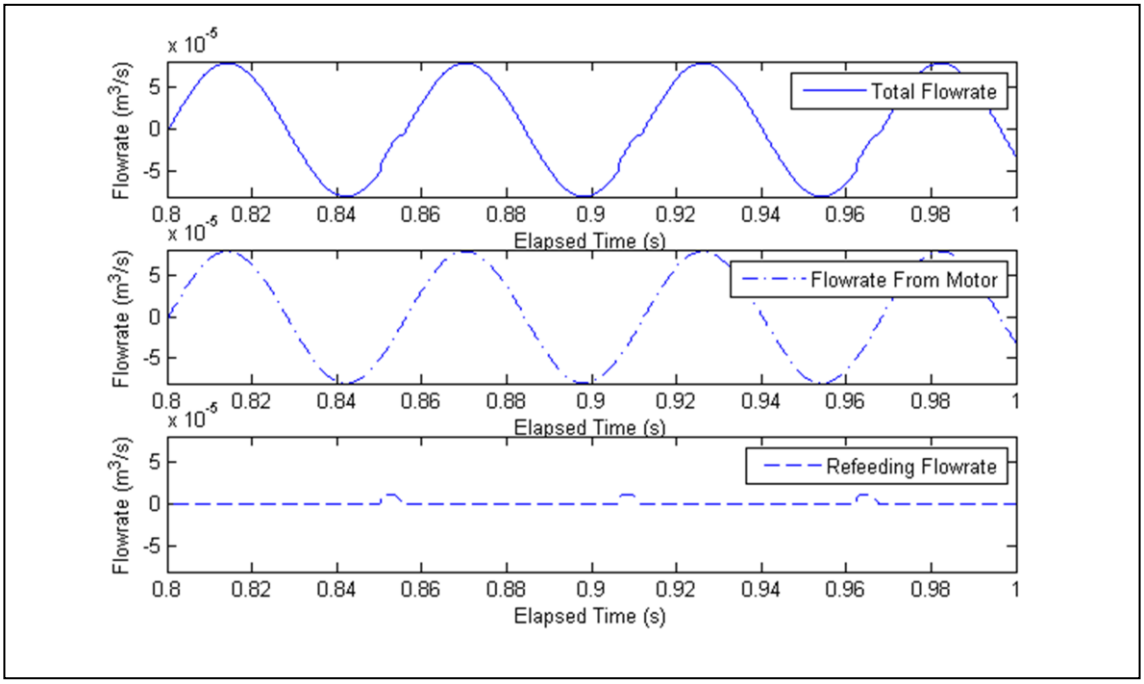

Figure 4.13 Flow to single side of hydraulic cylinder with refeeding circuit.

4.4.2 Enclosed Resonant EHA

The enclosed hydraulic system allows a high system pressure which results in a high hydraulic stiffness, and the elimination of the refeeding circuit removes a source of disturbances. The necessity to enclose the rotor to form a complete pressure vessel however leads to an increase in complexity, such as that signal and power wires to the electric motor have to go through the pressure vessel, and mass of the device. The Resonant EHA with the enclosed hydraulic system is shown in Figure 4.14. The flow equation between the pipes and cylinder are simply:

$$Q_{1f} = Q_1 \tag{4.31}$$

$$Q_{2f} = Q_2 \tag{4.32}$$

With the refeeding circuit equations removed, all other EHA equations are as presented in the refeeding circuit model. The system pressure set by the accumulator is now only limited by the electric motor pressure vessel, rather than the shaft seal, and so is set much higher than the refeeding circuit design.

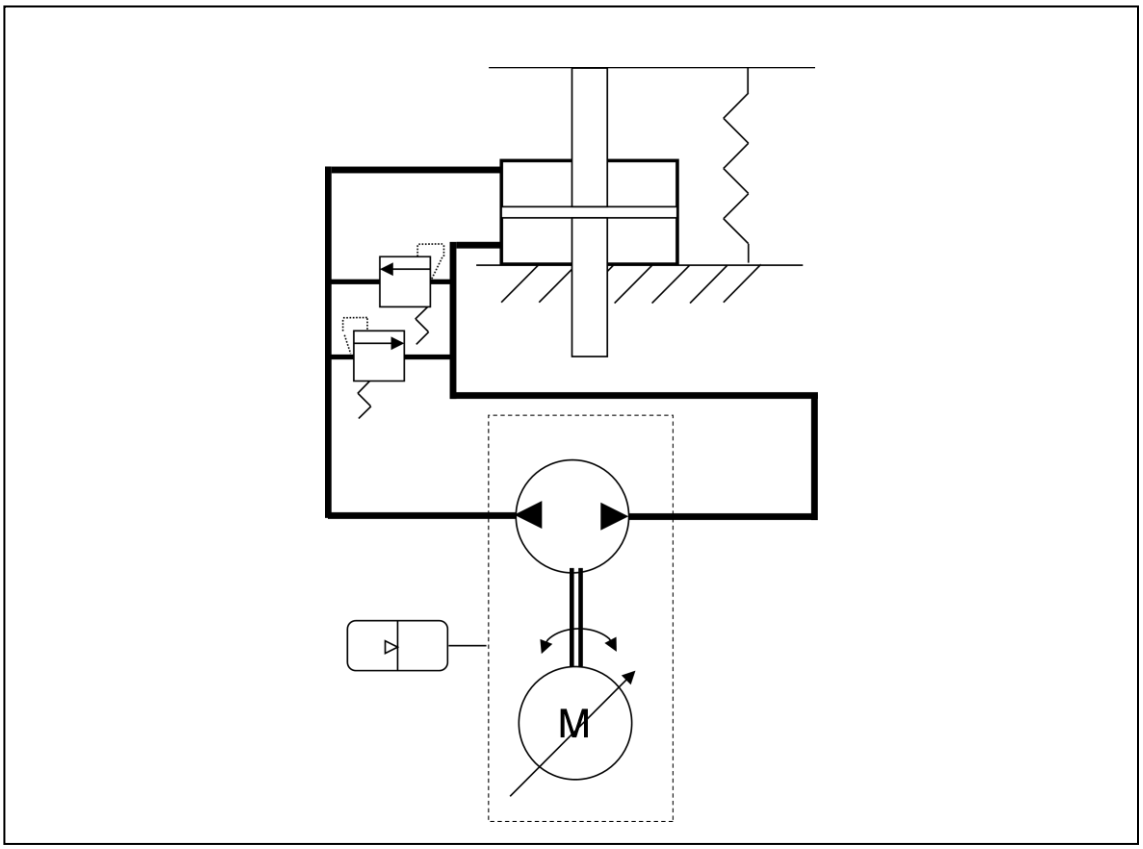

Figure 4.14 Enclosed Resonant EHA hydraulic circuit.

4.4.2.1 Enclosed Resonant EHA Discussion

A simulation of the enclosed Resonant EHA was constructed with parameters similar to those in Table 4.2. Specifically, the refeeding circuit related parameters are removed, the shaft viscous friction is updated to exclude the shaft seal friction but include viscous fluid shear, the bulk modulus is taken as 800 MPa and the system pressure set at 80 bar. Figure 4.15 shows the resulting net force on fuselage for Resonant EHA with an enclosed hydraulic circuit in time. The net force is smooth with no disturbances, therefore the feasibility of the enclosed hydraulic system EHA design to act as vibration isolator was considered better than the refeeding circuit EHA design.

From the modelling results the Resonant EHA appears able to meet the low net transferred force performance requirements in a relatively compact, low mass package. The design and construction of the experimental proof of concept Resonant EHA is given in the following chapter, Chapter 5.

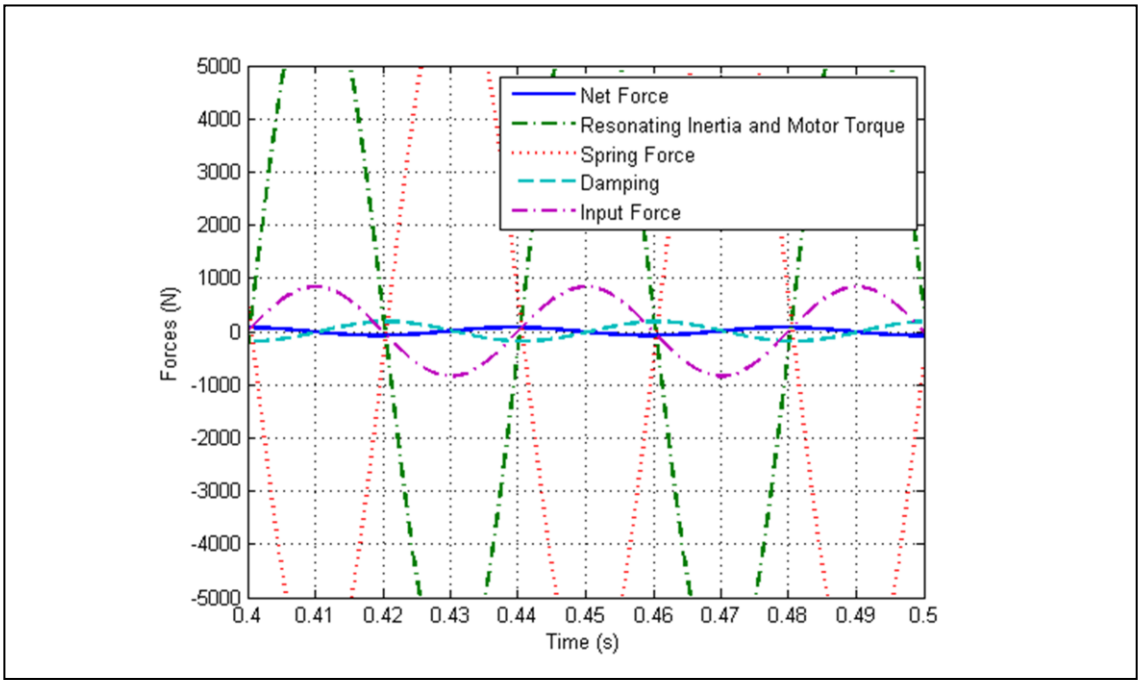

Figure 4.15 Fuselage force for Resonant EHA with enclosed hydraulic circuit.

Chapter 5
Resonant Electro Hydrostatic Actuator Experimental Device

The detail design of the experimental proof of concept Resonant EHA and component validation results are given in this chapter.

5.1 Experimental Device Description

5.1.1 Enclosed Resonant EHA Design

Key considerations taken in the practical design of the experimental Resonant EHA are given here. The design of the device was scaled down to a 2 tonne helicopter to allow the device to fit in an existing test rig, and was adapted for readily available components. The design of the proof of concept Resonant EHA included a gear pump, as a gear pump is compact, robust, and has low inertia. The maximum allowable motor inertia was found from the pump displacement, piston area and spring stiffness and driving frequency. During testing, small variations of the test driving frequency and/or spring stiffness were considered acceptable at this proof of concept stage.

The geometry of the EHA design allows flexibility in whether the motor-pump unit is placed in line with, or in parallel to the hydraulic cylinder. Placing the motor-pump unit in parallel produces a very compact length design in which piping can be minimised between the cylinder and the pump, however the motor-pump unit is placed off axis so could therefore introduce a bending mode of vibration which was considered undesirable. Although having the motor-pump unit inline dictates the load path being transferred through the motor-pump supporting structure, an inline based arrangement was decided upon due to all mass being present along the line of force. In order to form a closed system using a shaft seal the shaft seal would have to withstand the system pressure, which is not feasible while still allowing low friction rotation Instead, the shaft seal is removed and an enclosed vessel is formed around the shaft. There are two principal methods for forming a pressure vessel, either enclosing the rotor by inserting a pressure tube between the rotor and stator, or enclosing the stator and as a consequence having the stator wet. The wet stator approach was considered preferable as the alternative inevitably increases the gap between the stator and the rotor which impacts the electric motor performance. A cut out rendering of the inline, enclosed Resonant EHA for proof of concept testing is shown in Figure 5.1.

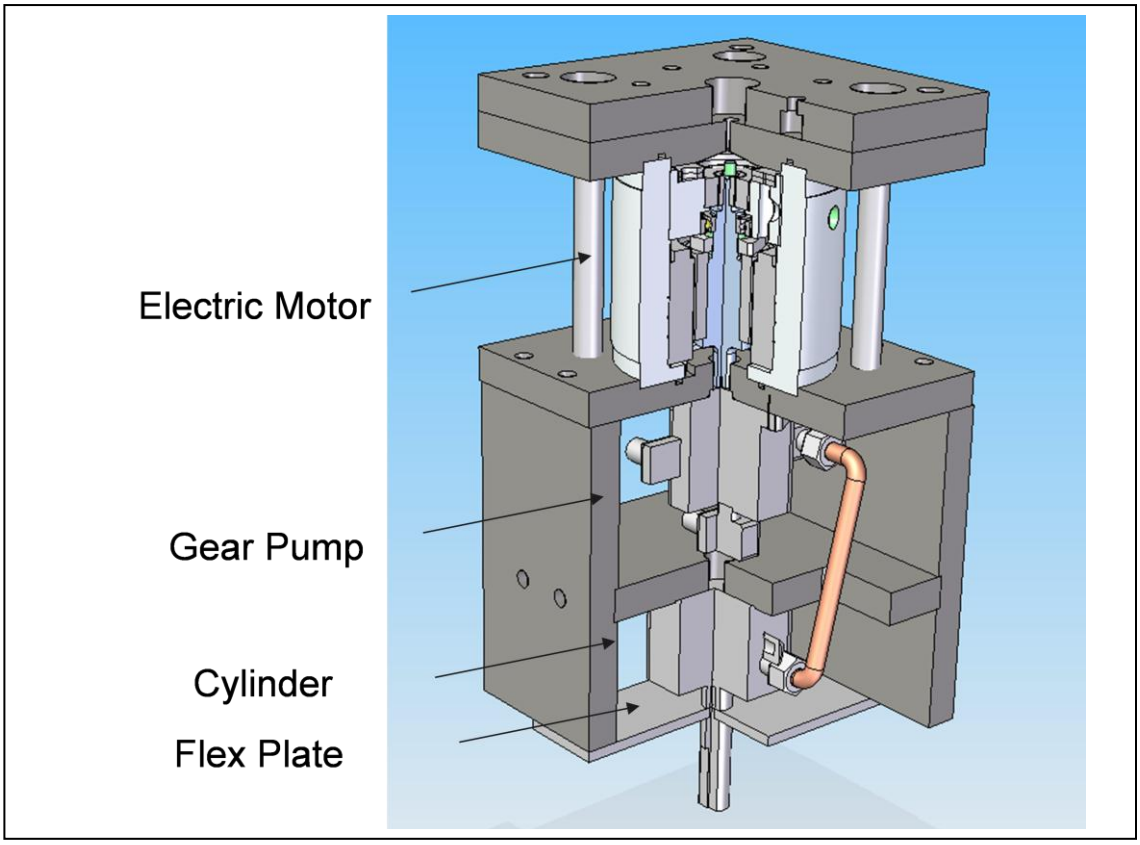

Figure 5.1 Enclosed inline Resonant EHA proof of concept cutaway drawing.

The supporting structure of the cylinder, pump, and motor was designed to be stiff, specifically to have a resonance frequency of over 10 times the fundamental 20 Hz testing frequency. The rotors position was specified to have a fine resolution and the ability to function immersed in pressurised oil, which was found to be met by an industrial resolver.

The flex plate is a clamped-clamped plate where the stiffness of the plate was intended to be equivalent to the compliance of the composite strut for the 2 tonne rotorcraft, and act as the stiff spring in parallel with the hydraulic cylinder. The stiffness of the target composite strut was taken as linear, which is not strictly true, and the flex plate itself being a clamped-clamped plate will exhibit different non-linearites. The flex plate was considered linear for small deflections as the maximum deflection in testing was less than 0.2% of the plate span. The Resonant EHA is approximately 340 mm in height and 200 mm square in width and depth.

5.1.2 Assembled Resonant EHA and Components

A detailed description of the Resonant EHA's components from the top to the bottom follows. A 20 mm thick steel top plate is bolted upwards to the testing machine load cell. The second top plate attaches to the upper flange via 4 bolts at the corners. 4 M16 x 180 mm cap screws clamp the top flange to the bottom flange with the pressurised motor housing in-between. The gear pump is bolted below the bottom flange. An accumulator which is not shown is attached to the leakage port of the pump. For the current experiment a flexible length of hose which also functioned as the feeding path was used as the accumulator. The use of the hose as an accumulator was justified in the test setup as the low leakage rate of the device ensured the pressure was maintained over hour length testing periods. Two 200 bar pressure sensors are attached via T junctions between the cylinder and the pump ports. The hydraulic circuit diagram, Figure 4.14, shows pressure relief valves that were not included in the proof of concept device, however they would need to be part of a final commercial device. The pressure vessel bottom flange is bolted to the steel "H" shape frame, where the hydraulic cylinder is attached to central rib of the "H" structure. The cylinder rod is threaded on to the spigot which clamps the flex plate. The flex plate is 7.9 mm thick stainless steel and is taken as being a linear spring over the displacement amplitudes considered. The driving actuator is clamped onto the head of the spigot from below using the testing machine jaws.

A list and brief description of bought in components for the proof of concept Resonant EHA is given in Table 5.1. A section view of the enclosed brushless motor is shown in Figure 5.2. A description of the features from the top is as follows. A blanking plug and Dowty washer (not shown) plug the bleed hole in the top flange. The resolver rotor is attached to the shaft via a nut. The resolver stator is glued to the bearing mount. The bearing is located with a circlip to the shaft. The motor rotor is attached to the shaft by a nut. The motor stator is glued to the housing. For the resonant design to be effective, the gear pump shaft is rigidly coupled to the brushless motor shaft. O rings seal the top flange and bottom flange to the housing, and the gear motor to the bottom flange. Feedthroughs for wires are not shown however they are present to allow both electrical power and resolver feedback and be able to withstand the mean system pressure without allowing leakage. Figure 5.3 shows the complete assembled proof of concept Resonant EHA. Figure 5.4 to Figure 5.9 show individual component details of the Resonant EHA including inside the electric motor pressure housing, the shaft and rotor, the gear motor, the flex plate and the compact double ended cylinder.

Table 5.1 Description of principle bought in components.

Bought In Component	Description
Kollmorgen KBMS 17x01C frameless brushless DC electric motor.	6 Nm peak torque, 2.1 Nm continuous stall torque, 810 W continuous power, 1 kg stator and rotor mass.
Harowe 15BRCX-601-K10 resolver.	Frameless, 36 mm diameter stator, ±10 arcmin resolution.
Kollmorgen AKD 01206 servo drive.	240 V voltage output.
TC Ltd. WFS-1/2”BSPT-18CU-3-V and WFS-1/4”NPT-24CU-4-V wire feedthroughs.	Multiple wire sealing assembly for pressure vessels.
Vivoil XV-0R 11 01 B BB E hydraulic gear motor.	1.5 cm^3/rev displacement, external case drain.
Parker 32 K T CHD hydraulic cylinder.	Compact mounting, 36 mm diameter bore, 18 mm diameter double ended rod, 10 mm stroke.

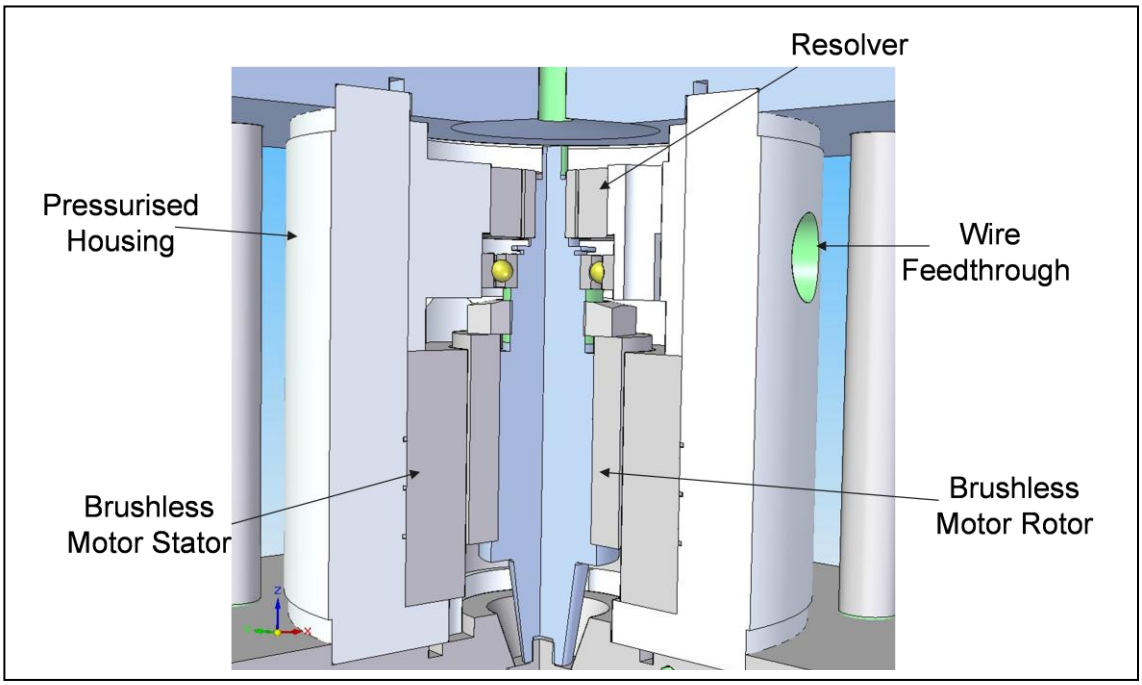

Figure 5.2 Enclosed Resonant EHA electric motor cutaway

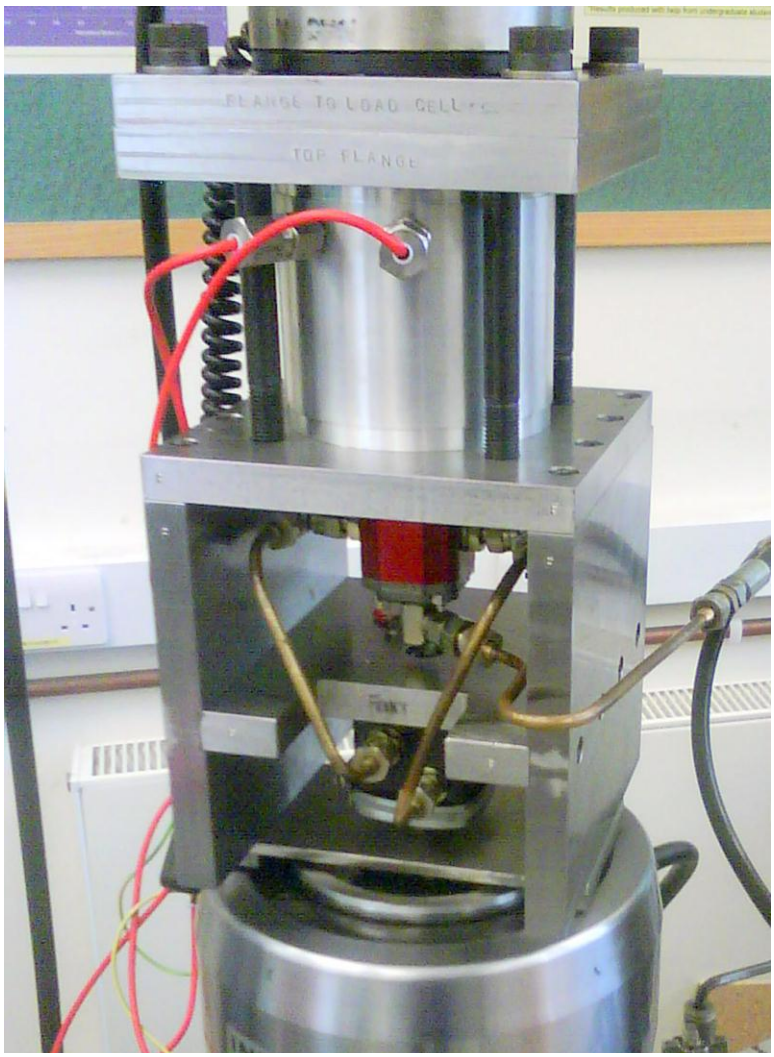

Figure 5.3 Proof of concept Resonant EHA as constructed.

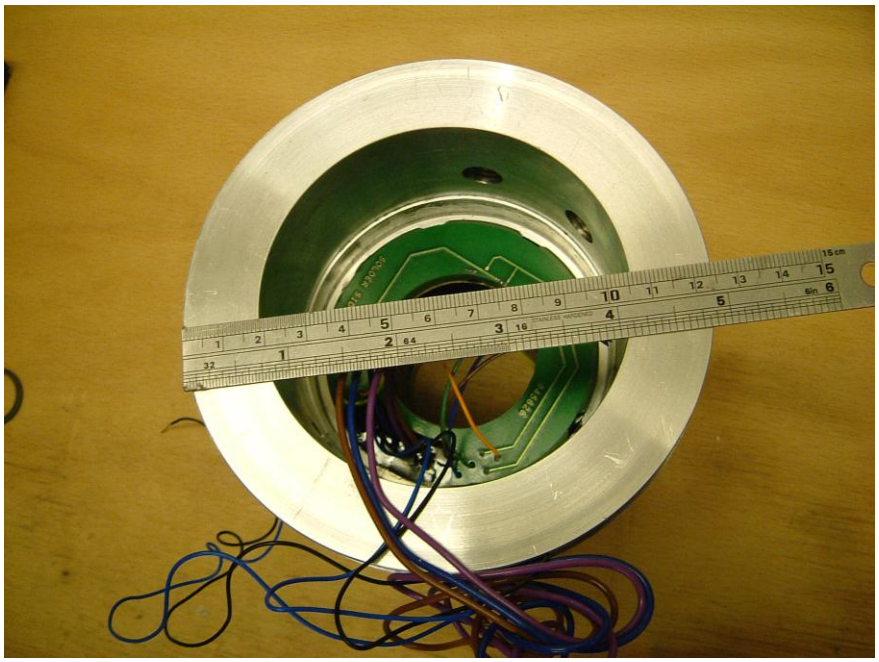

Figure 5.4 Pressure housing with DC brushless motor stator inserted.

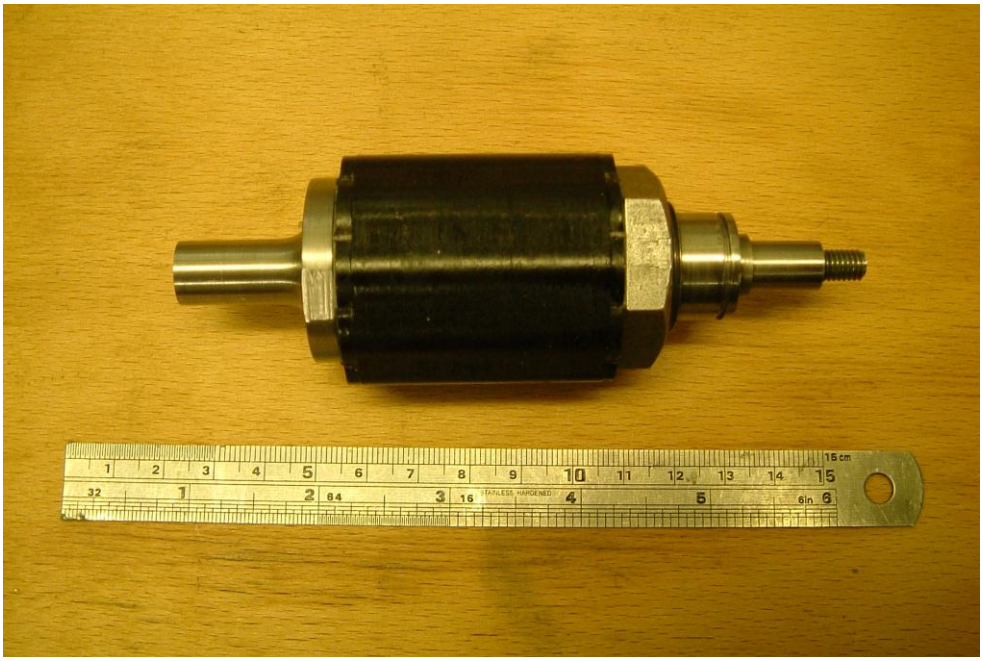

Figure 5.5 Shaft and brushless motor rotor.

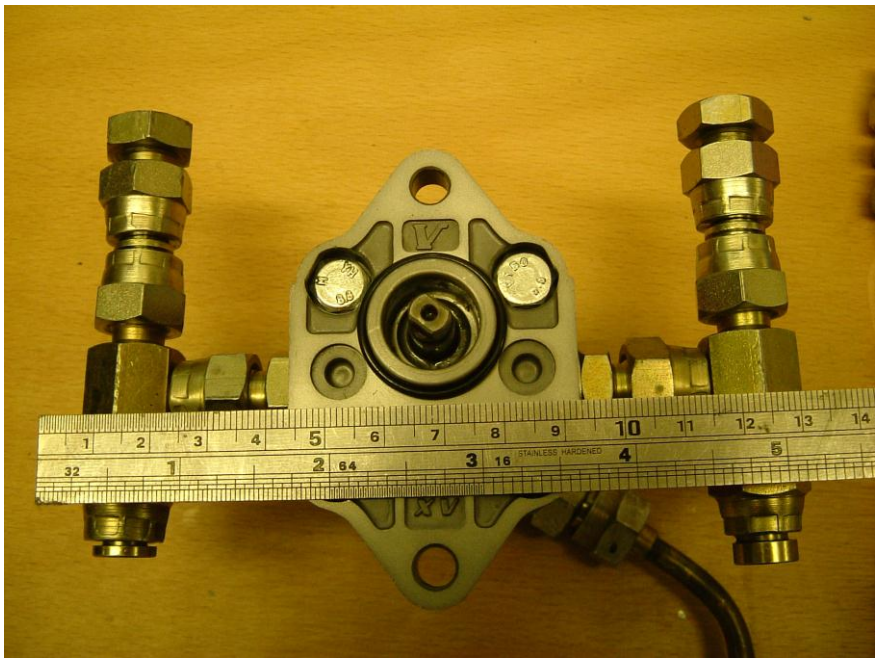

Figure 5.6 Hydraulic gear pump with shaft seal removed.

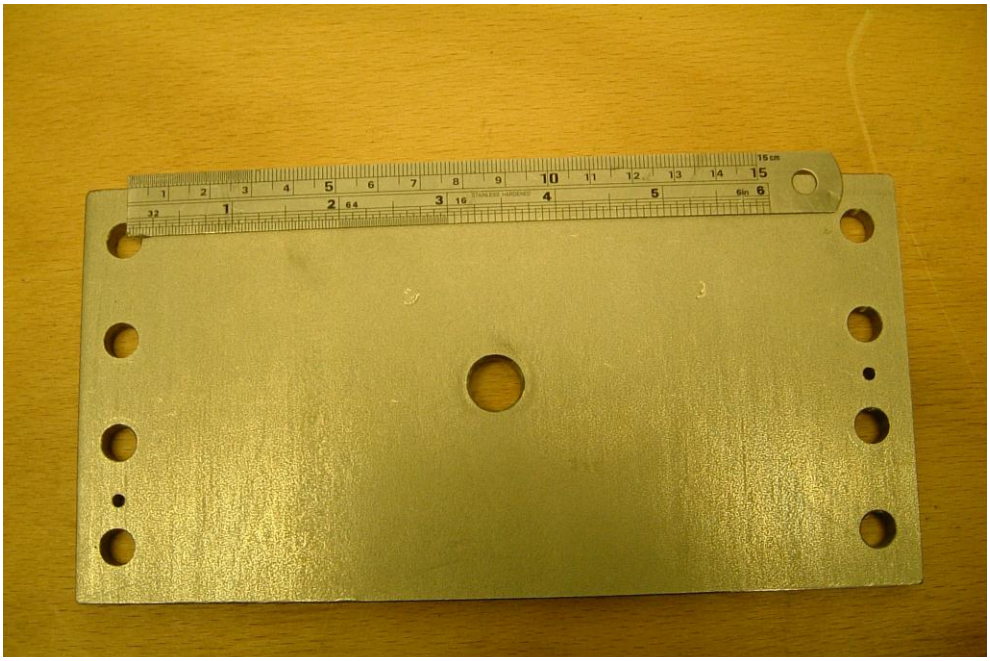

Figure 5.7 Stainless steel flex plate.

Figure 5.8 Hydraulic cylinder with end removed.

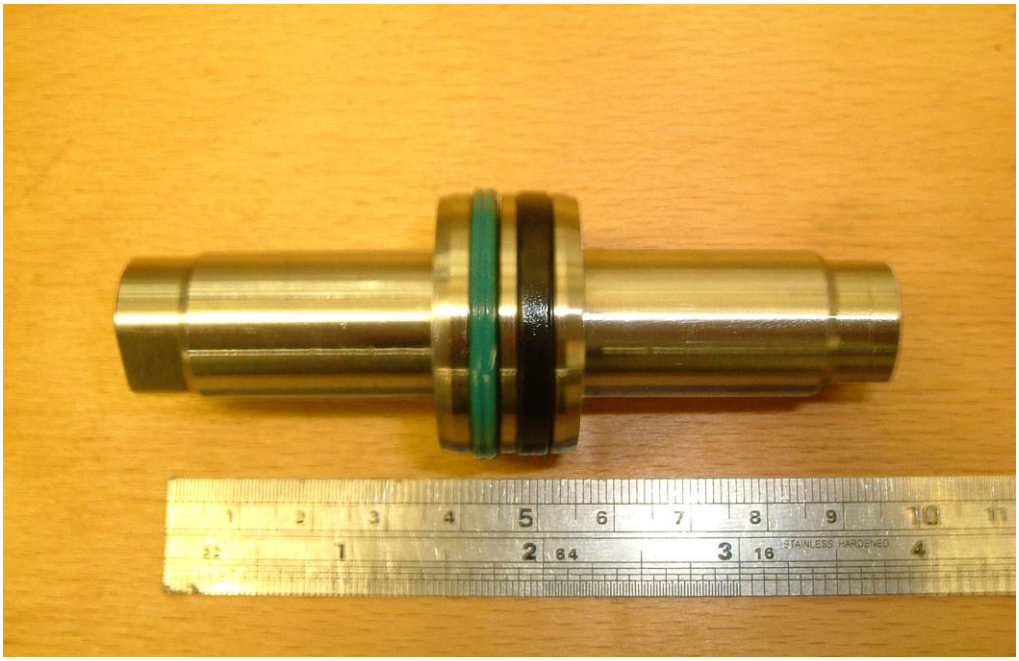

Figure 5.9 Double ended cylinder rod and piston.

5.1.3 Test Setup and Control Scheme

The Resonant EHA is mounted in an Instron 1332 dynamic materials testing machine where the mechanical input is from below and an Instron 2518-101 load cell measures the transmitted force to the test machine frame. Two open loop demand channels, the servo motor demand (typically a torque input, with velocity or displacement inputs possible) and the testing machine demand (typically a displacement input, with a force input possible) are sent out from a single waveform card with a common clock. In addition to the two output channels, the following six channels of data are synchronously recorded:

i. Load cell force. Dynamic range of ±25 kN.

ii. Pressure P1 (located outside left pump port, positive pressure extends cylinder rod). Range of 0 to 280 bar.

iii. Pressure P2 (located outside right pump port, positive pressure retracts cylinder rod). Range of 0 to 280 bar.

iv. Resolver angular position (rigidly attached to electric motor shaft). Range of ±2270°, resolver resolution ±10 arcmin.

v. Displacement of testing machine. Maximum displacement ±50 mm.

vi. Linear variable differential transformer (LVDT) extension (between flex plate and hydraulic cylinder). Range of 3 mm.

The current feedback and velocity feedback from the electric motor are able to be obtained separately. A thermistor is present within the electric motor. The thermistor output is monitored by the servo drive which cuts out in the occurrence of an over temperature event. The temperature of fluid next to the electric motor is separately measured by a thermocouple which can be monitored visually. A schematic of the signals in the test setup is shown in Figure 5.10.

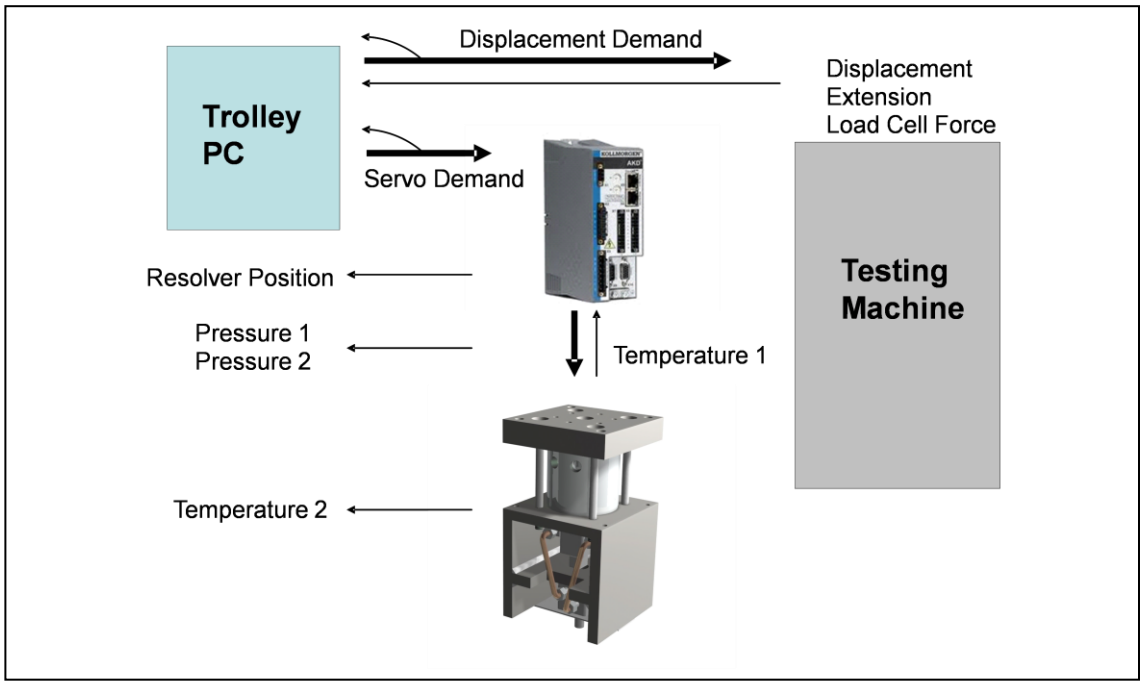

Figure 5.10 Schematic diagram of data streams in experiment.

5.2 Device Parameter Measurement

The flex plate stiffness, the EHA structural stiffness and frequency response, the rotor inertia, the motor viscous friction in oil, and the hydraulic motor leakage of the Resonant EHA were measured experimentally. A comparison of the results with an expected range of parameter values is also stated.

5.2.1 Flex Plate Design

Using Euler beam bending theory and finite element based models (ANSYS) a flat flex plate with a stiffness of 19 kN/mm was initially designed using stainless steel material properties. Figure 5.11 shows the simulated deflection of the flex plate with the boundary condition being ends that are perfectly clamped and 7 kN force applied through the inner surface of the centre hole. The contour lines indicate deflection magnitude. The flex plate was experimentally found to have a stiffness of 14.6 kN/mm. The lower stiffness is attributed to small rotations of the flex plate's clamped ends as a consequence of the holding bolts stretching. Although the lower stiffness lowers the zero degree of freedom device resonant frequency from 25.6 Hz to 22.4 Hz, the testing frequency was considered still satisfactory for proof of concept testing. The flex plate stiffness was found to be within 10% linearity for a 0.3 mm amplitude position input.

To obtain position measurement data excluding the testing machine stiffness an LVDT was mounted on the body of the hydraulic cylinder with the probe pressed against the spring surface. The location of the LVDT probe on the flex plate is shown by the circle in Figure 5.11, which is not the centre of the flex plate. .The deflection result of the finite element model was used to scale the LVDT's location to the actual testing machine's displacement at the centre of the flex plate. The scaling factor was determined to be 1.30.

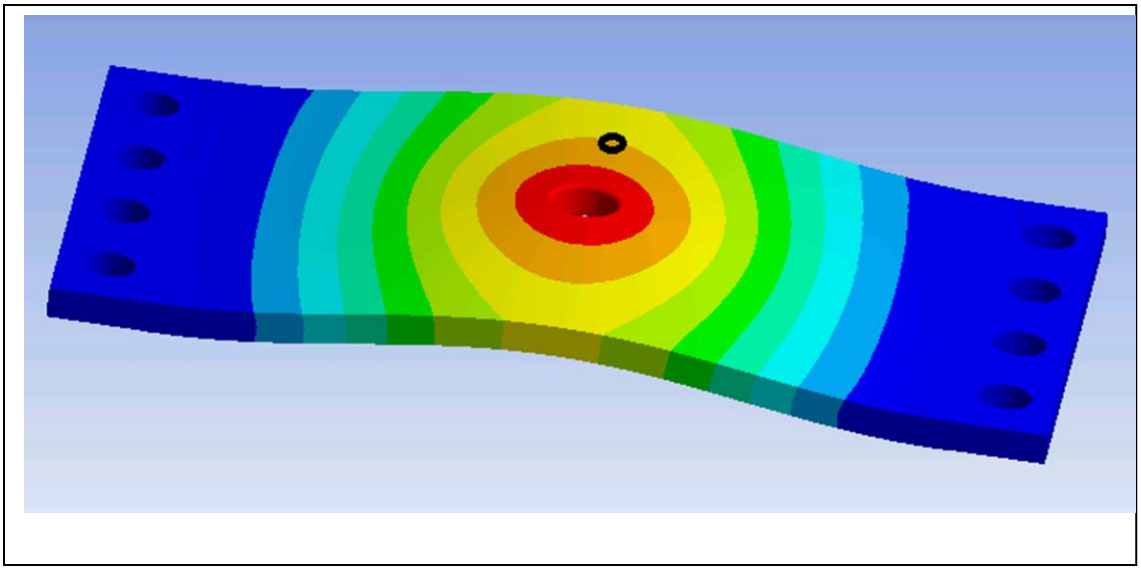

Figure 5.11 Finite element result of flex plate deflection. LVDT position indicated by circle.

5.2.2 EHA Structural Integrity and Response

For the proof of concept Resonant EHA design the bolts holding the end caps of the pressure vessel of the electric motor also act as the load path between the displacement input and the measured force. In an actual helicopter the use of the motor pressure vessel to carry static flight loads would have to be considered with extreme caution, however for testing purposes it is sufficient that the structure is sufficiently stiff and has its lowest modes of vibration at frequencies an order of magnitude higher than the fundamental test frequency.

The pressure vessel was tested at 120 bar (1.3 times the nominal system pressure) for three hours with no external loading and was found to be leak free. In compression the Resonant EHA structure was found to have a stiffness of at least 66 kN/mm, where the flexibility of the testing machine itself is beginning to be considered significant. The Resonant EHA was hung off the test load cell and a vertical tap test applied to the base. The measured resonant frequency of the EHA structure hanging off the load cell was found to be 260 Hz, which at greater than ten times the fundamental testing frequency validates the test setup.

5.2.3 Rotor Inertia

The inertia of the motor rotor, including the hydraulic pump inertia, was validated experimentally by demanding a sinusoidal angular velocity (157 rad/s amplitude, 20 Hz frequency) with the rotor in air, and by measuring the current required to obtain the peak acceleration. Newton's angular acceleration equation was then used to find the rotor inertia:

$$I = \frac{T_e}{\alpha} = \frac{K_T i}{\omega 2\pi f} \quad \textbf{(5.1)}$$

The rotor inertia was found to 1.40 kgcm^2. This rotor inertia is close to the value predicted from CAD modelling and manufacturer's data.

5.2.4 Rotor Viscous Drag and Hydraulic Pump Friction

Using theory from Massey [70], the opposing torque produced by viscous drag in a laminar flow rotary viscometer is:

$$T_V = \frac{\pi h \mu \omega D_{Ro}^{\ 3}}{4c} = C_V \omega \quad \textbf{(5.2)}$$

where, h is the height of cylinder in contact with the fluid, μ is the absolute viscosity of the fluid, ω is the rotational velocity, D_{Ro} is the outer diameter of the cylinder, and c is the annular clearance. Using Equation (5.2) on the electric motor rotor in oil, with a height of 50 mm, diameter of 45 mm and an annular clearance of 0.2 mm with the absolute viscosity of the HLP32 hydraulic oil at 30° being 0.04 Pas [70] gives a torque loss per radian of 0.7 mNms/rad. At 20 Hz a 0.35 mm input transferred through the hydraulic gearing gives a peak angular velocity of 100 rad/s, which implies a maximum viscous torque of 70 mNm.

The combined viscous drag of the rotor and the friction in the hydraulic pump was investigated by moving the cylinder using the testing machine with a 0.1 Hz to 0.5 Hz range of 3mm amplitude triangular waves in position control. The pressure difference across the gear pump and the rotor velocity were recorded. The frictional torque was found by the pump displacement multiplied by the pressure difference with the results shown in Figure 5.12. The experimental results show Coloumb friction dominating the viscous friction components for the velocities tested.

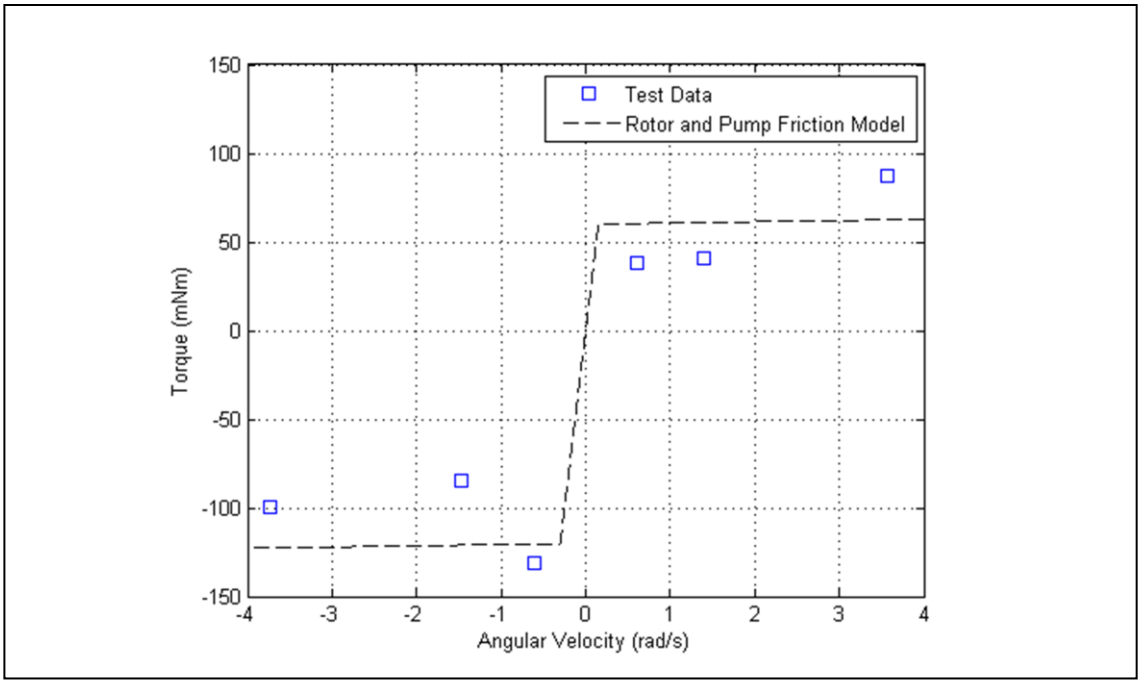

Figure 5.12 Torque resistance against rotor velocity for gear pump and rotor. Dashed line shows Coloumb and viscous model.

The offset in torque resistance with direction is attributed to the initial pump running in being performed in only one direction. The difference between the theoretical viscous drag friction and the experimentally measured friction is thought to be from the gear pump journal bearing. A combined pump and rotor friction model was used in the simulation where a Coloumb friction model was implemented for the gear pump, and a viscous friction model used for the rotor. The Coloumb friction values of -120 mNm and 60 mNm absolute values were chosen and combined with the viscous torque of of 0.7 mNms/rad, where the plot of which is shown in Figure 5.12. From Figure 5.12 there is some evidence that a Stribeck friction model would be appropriate however there was not enough test data to justify the implementation.

5.2.5 Cylinder Seal Friction

The combined friction force of the filled PTFE (Teflon) piston seal, two rod wiper seals, and two flurocarbon shaft seals must be cancelled by the electric motor torque to obtain a zero net force on the load cell. For an initial estimate from the Seal and Sealing Handbook by Flitney [71] (from Figure 4.16, page 295) the seal friction force on one general plastic reciprocating seal at a pressure of 90 bar and moving at 0.04 m/s is 160 N. Excluding the wiper seals the expected friction of three seals in the hydraulic cylinder is 480 N, however actual friction values are dependent on many factors including individual seals geometry, and material, and the rod or cylinder bore surface roughness.

For experimental testing lateral loads on the cylinder were minimised by confirming the vertical alignment of the test rig in the testing machine. The cylinder only was tested at atmospheric pressure with a light oil coating by a 0.35 mm displacement triangle wave at 20 Hz, and the friction amplitude was found to be ±400 N. The cylinder and gear pump (with the electric motor rotor not present) were tested at 70 bar. Figure 5.13 shows the time series response for a 0.35 mm displacement triangle wave at 20 Hz. Similar magnitude results were found for 1mm 1Hz input displacements.

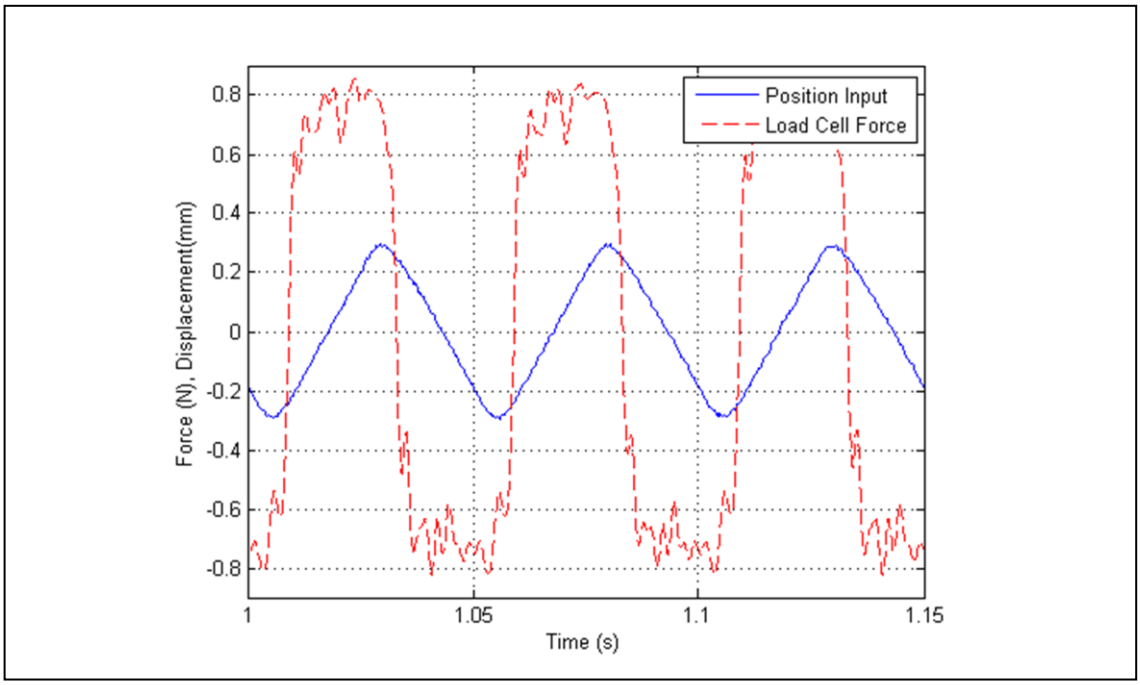

Figure 5.13 Friction from the hydraulic cylinder and gear pump at 70 bar system pressure.

The average friction amplitude of ±760 N was found for the cylinder and pump over a series of tests. A Coloumb friction model was implemented to match the test results where the gear pump friction found in the previous section, Section 5.2.4, was converted to an equivalent linear motion friction and subtracted from the experimental combined seal and pump friction. A seal friction value of ±550N was found with this method and used in the simulation. The combined seal and gear pump friction showed variability even with nominally identical tests. For further discussion on hydraulic cylinder seals the reader is referred to the thesis by Bullock [72]. Bullock has analysed the amplitude dependence and frequency dependence of seal friction from sinusoidal motion and found the friction force increases as the displacement amplitude is reduced (Figure 3-16, page 55).

In a closed EHA hydraulic system it is critical that the cylinder shaft seals are tight and seal the hydraulic fluid with near zero external leakage, however there is trade-off between higher cylinder friction forces and lower leakage. The compact hydraulic cylinder chosen for the proof of concept device had very good sealing capability, but relatively high friction. Due to the sub millimetre dynamic stoke for this application future work involving clamped flexing seals, or bellows instead of the cylinder is of consideration if the millimetre scale semi static stroke is also able to be compensated for.

5.2.6 Pump Internal Leakage

The internal leakage of the gear pump was found by the quasi steady state angular velocity of the pump against a constant pressure difference, which was created by driving the electric motor against blocked ports, as shown in Figure 5.14. The angular velocity was found from the difference in angular position over time. The leakage flow coefficient was found from:

$$K_{il} = \frac{D\omega}{\Delta P} \qquad \textbf{(5.3)}$$

The leakage was found for a positive pressure difference to be $1.0\text{x}10^{-13}$ $m^3/s/Pa$, and for a negative pressure difference to be $1.8\text{x}10^{-13}$ $m^3/s/Pa$. The leakage magnitude is similar to those given in previous literature [3]. In the hydraulic pump the difference in leakage values with direction may be attributed to the initial pump running-in being performed in only one direction.

5.2.7 Hydraulic Stiffness Characterisation

5.2.7.1 Initial Testing Results

The effective bulk modulus of the fluid and mechanically compliant elements (such as seals) is found from the rotational response of the pump shaft to torque square wave inputs when the cylinder position is locked. In an ideal case there should be no rotation of the shaft for an infinite fluid bulk modulus. The rotor rotation for a 1 Hz reversing torque square wave input is shown Figure 5.14. The jumps in position coincide with torque reversals. The steady state drift due to leakage is punctuated by ripple when discrete gear teeth disengage and remesh. The effective compressibility equation of the fluid trapped between the cylinder and pump is:

$$B_{Eff} = V\frac{\Delta P}{\Delta V} \qquad \textbf{(5.4)}$$

where the volume of trapped fluid V is taken as the volume of fluid in the pump, pipes and cylinder on a single side of the pump, which is 8.9 cm^3, ΔP is the steady state difference in pressures which is 40 bar, ΔV is taken as the fluid ejected from the rotation of the pump, the difference in position multiplied by pump displacement; which for the 80° rotation is 0.33cm^3.

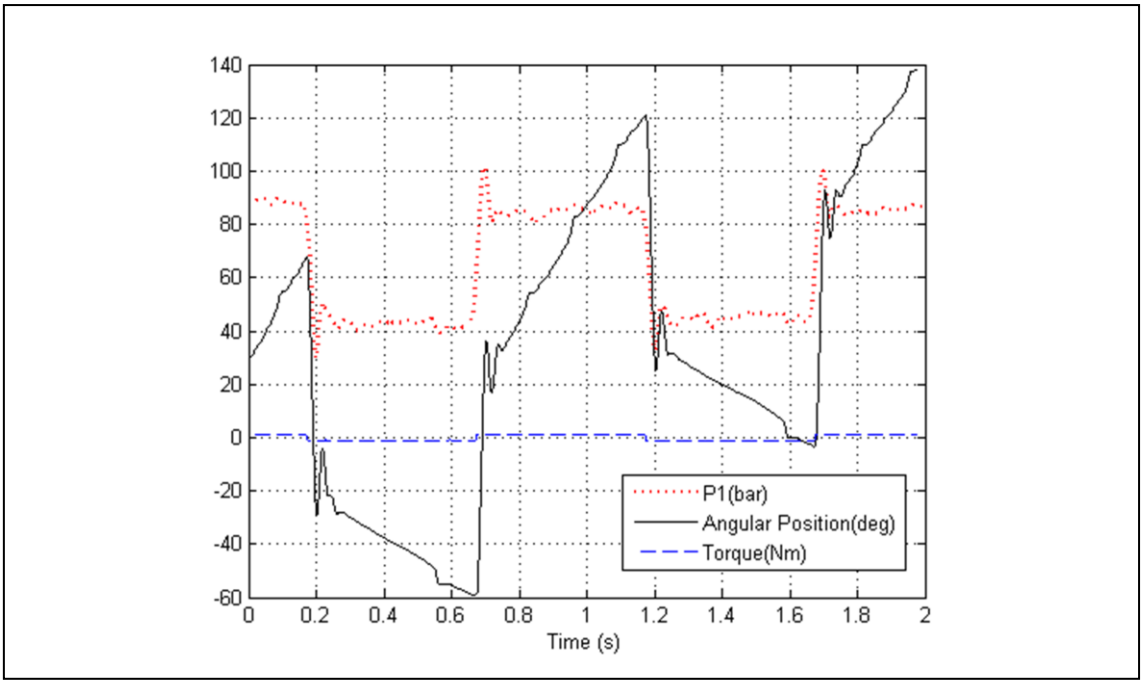

Figure 5.14 Motor rotor position for locked cylinder subject to a ±1 Nm square wave torque.

The calculated effective bulk modulus is 110 MPa, much less than what would be expected from a simple consideration of oil compressibility. For reference, oil at room temperature with a mean pressure of 70 bar and 10% air content has an effective bulk modulus of 1000 MPa [4]. On removing the pipes and blocking the pump ports and retesting with a range of torque inputs there was still found to be a consistent free play in rotor position for reversing torque inputs, as shown in Figure 5.15. Figure 5.15 shows rotor position and the pressure at either side of the pump in time, the free play is the 40° gross rotation when the torque reversal occurs.

Backlash in the shaft coupling was investigated by viewing the gear pump teeth rotation for low frequency triangular position input. As no delay was visually observed at the velocity reversal mechanical backlash was rejected as the origin of the free play. The cause of the backlash is hypothesised to be from the action of the gear pump. A potential explanation for the gross rotation is given as follows:

i. A steady state torque compresses the fluid on the high pressure side. The gear teeth are forming a seal between the high and low pressure sides.

ii. The torque direction reverses, the teeth of the gear pump rotate in the direction of the torque reversal due to both the torque of the electric motor and the pressure difference between the two ports. At some point sealing between the gear teeth is lost.

iii. Prior to the opposite faces of the gear teeth establishing a seal, the new high pressure side leaks fluid to low pressure side.

iv. The pump rotates to compensate for the lost fluid.

This was investigated by demanding in position control a triangular wave, and on the reversal of direction a period with zero pressure difference where the pressures on either side of the pump are equal, was noted to occur, as shown in Figure 5.16. Ideally with only pump leakage the pressure difference would be a square wave, with edges where the gradient for the decrease is the same as the increase, which is not the case. To improve the linearity of the pump the use of a non-zero mean torque was investigated.

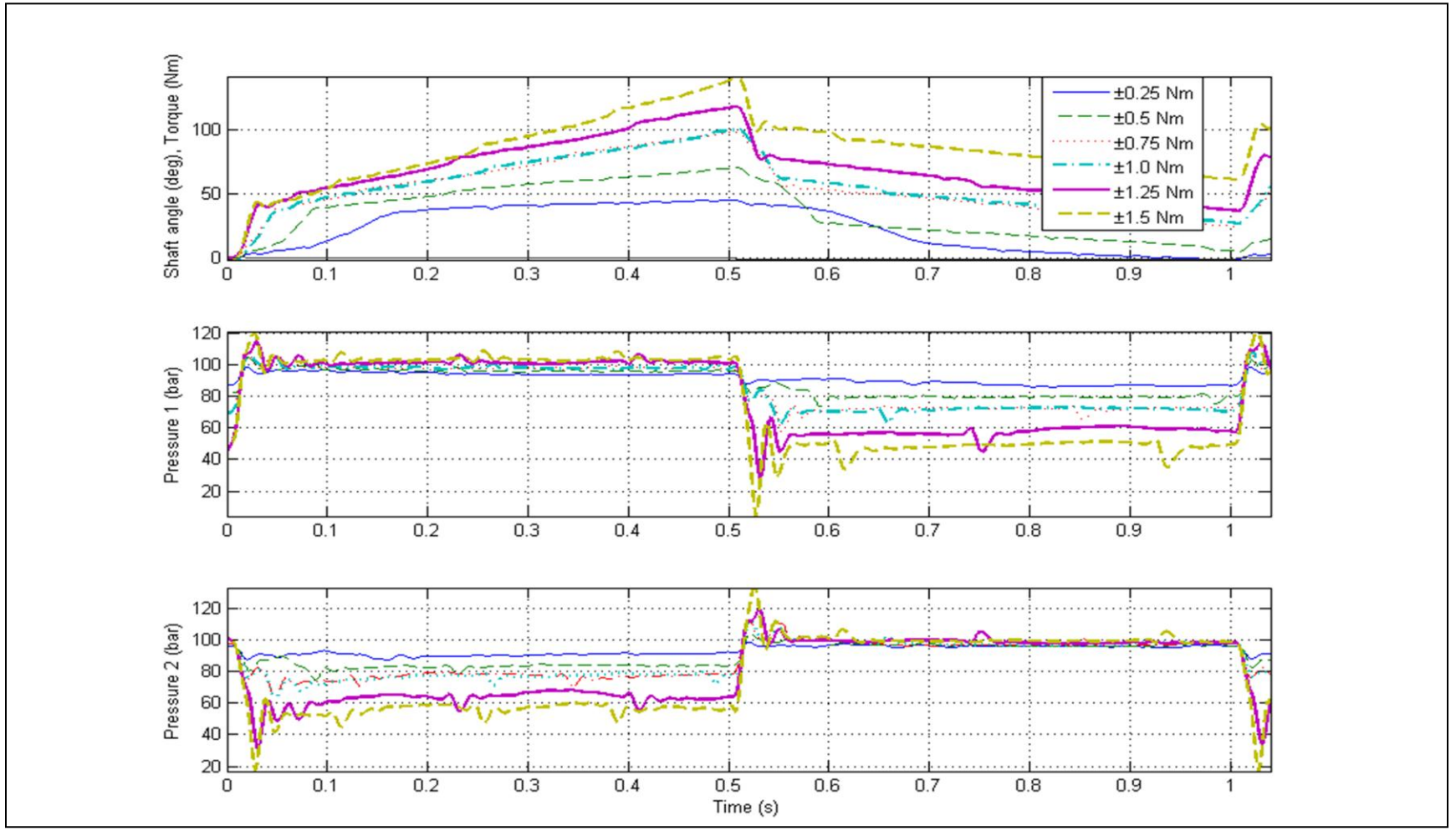

Figure 5.15 Motor rotor position and pressures for square wave ±0.25 Nm to ±1.5 Nm torque inputs with blocked pump ports.

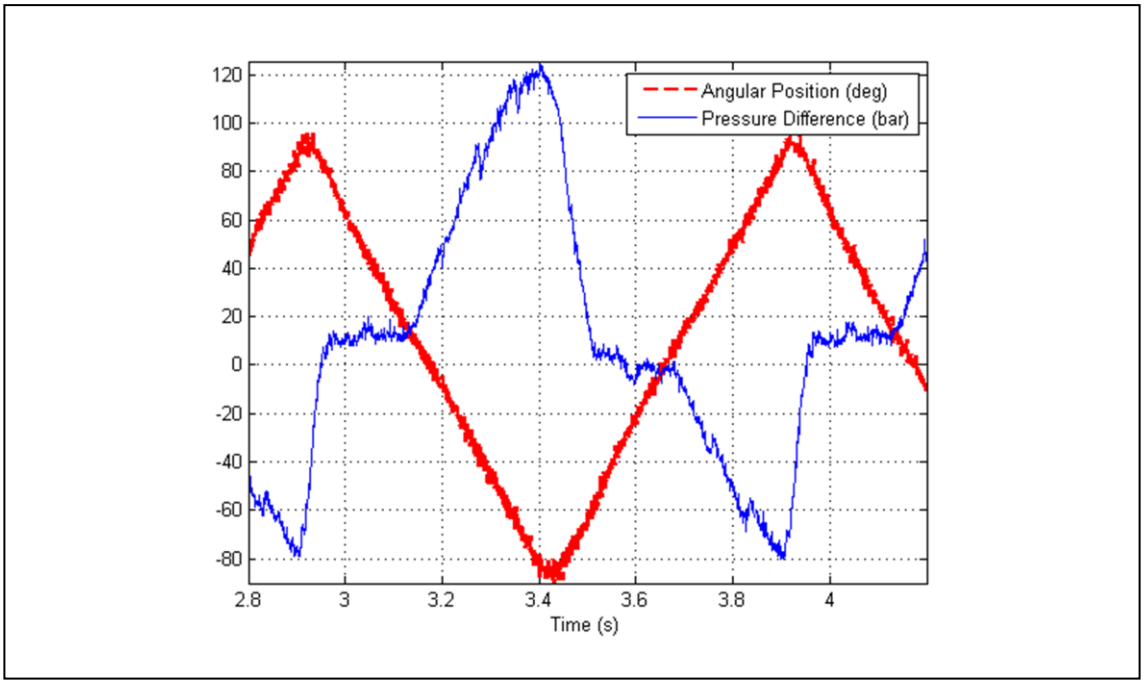

Figure 5.16 Triangular wave in position control showing pressure difference across pump with blocked ports.

5.2.7.2 Non Reversing System Operation

The extent of free play in the gear pump about zero mean torque made vibration isolation unsatisfactory in that regime. Testing with a mean positive torque input, therefore ensuring that the torque direction on the pump was constant was investigated as a means of reducing the free play.

Figure 5.17 shows the shaft rotation and pressure values in time for square wave torque inputs of ±0.25 Nm to ±1.25 Nm with a mean torque of 2 Nm against blocked ports. In processing the shaft rotation in Figure 5.17 the constant rotation for the torque inputs has been subtracted for clarity. The ripple in position and pressure seen in the figures is from the discrete gear teeth disengaging and remeshing. In the position plot in Figure 5.17 it can be seen that there is up to 10° shaft rotation at the torque change, which is less than the previous torque reversing case, and the shaft rotation is dependent on the torque level, which would be expected from compressibility effects.

With the hydraulic cylinder reattached and locked, Figure 5.18 shows the shaft position for a square wave torque inputs of ±0.25 Nm to ±1.25 Nm amplitude with a 2 Nm mean torque. It should be noted the pressure difference is distorted by the high pressure side experimentally not rising as high as would be expected. From Figure 5.18 for the ±1Nm torque input the angular change due to compressibility is improved to about 20°, and an average pressure change of 30 bar gives an effective bulk modulus of 300 MPa. Although 300 MPa is a much improved value over the previous, under subsequent sinusoidal non reversing operation a bulk modulus of 700 MPa gave a better match between simulation and experimental results, and is used in the simulation results presented in Chapter 6. One possibility for the difference in bulk moduli values is that the square wave compressibility tests do not adequately reflect sinusoidal system operation.

To avoid the free play region, experimental testing was performed using a non-zero mean torque ensuring a constant torque direction. For testing the dynamics of the device, using a non-zero mean torque was considered acceptable, however the practical feasibility of the device to be implemented using a non-zero mean torque is not compelling as the electrical energy used to rotate the motor is unused outside ensuring the linearity of the device, therefore there is a

significant waste of energy. In addition to the wasted energy, the volume and mass of the motor will be greater if the motor has to be sized for a higher peak and RMS torque.

The design of the proof of concept Resonant EHA included a gear pump, as a gear pump is compact, robust, and has low inertia, however the loss in linearity when reversing about small angles discovered implies that for future work redesign and testing with other pump categories, such as piston pumps or vane actuators, is highly recommended.

The simulation model was updated to include the experimentally observed effect of free play for torque reversals about zero as described in Section 5.2.7.3.

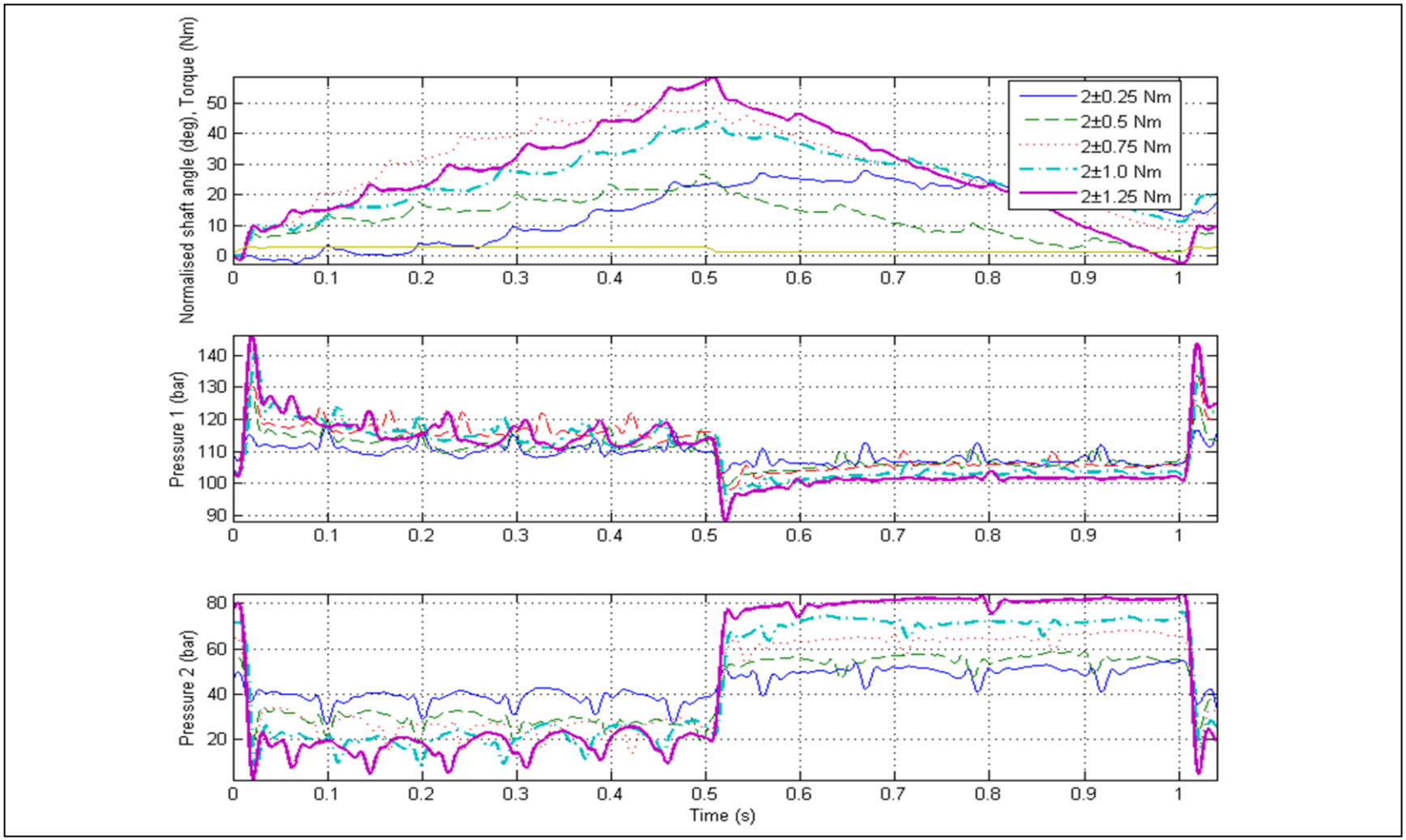

Figure 5.17 Motor rotor position and pressures for square wave 2 ±0.25 Nm to 2 ±1.25 Nm torque inputs against blocked ports. The changes in mean position have been subtracted for comparison purposes.

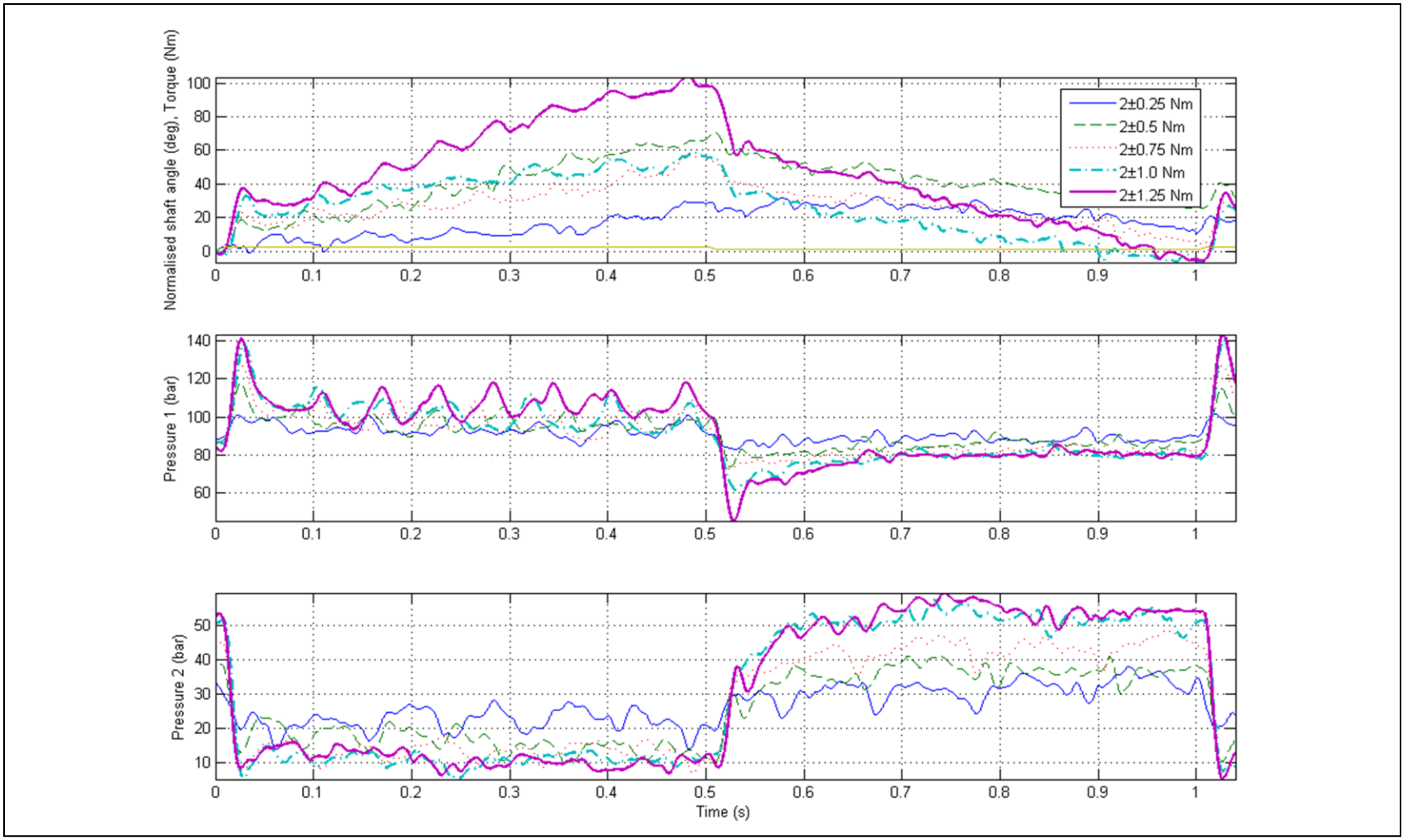

Figure 5.18 Motor rotor position and pressures for square wave 2 ±0.25 Nm to 2 ±1.25 Nm torque inputs with cylinder attached. The change in mean position have been subtracted for comparison purposes.

5.2.7.3 Free Play Model

To mimic free play in the gear pump the shaft model was split into two sections, the electric motor shaft and the pump shaft, and was connected by a non-linear stiffness as shown in Figure 5.19.

The load torque acting on the electric motor shaft is:

$$T_{Ex} = \begin{cases} k_T(\theta_e - \theta_p - \theta_{Fp}) & if\ (\theta_e - \theta_p) \geq \theta_{Fp} \\ 0 & if\ -\theta_{Fp} \leq (\theta_e - \theta_p) \leq \theta_{Fp} \\ k_T(\theta_e - \theta_p + \theta_{Fp}) & if\ (\theta_e - \theta_p) \leq -\theta_{Fp} \end{cases} \quad \textbf{(5.5)}$$

where θ_{Fp} is a constant free play angle , θ_e and θ_p are the rotational angle of the electric motor and the pump shaft where a positive rotation is defined as anti-clockwise as viewed from the motor, and k_T is the shaft stiffness.

The equation of motion of the pump shaft is:

$$T_{ex} - T_p = k_T(\theta_e - \theta_p) - D(P_1 - P_2) = I_p\dot{\omega}_p + c_{fp}\omega_p \quad \textbf{(5.6)}$$

where T_p is the torque produced by the pump as it is driven by a pressure difference across its ports, I_p is the inertia of the pump gears, and c_{fp} is the viscous damping on the pump gears. The free play model described here was included in the Resonant EHA simulation.

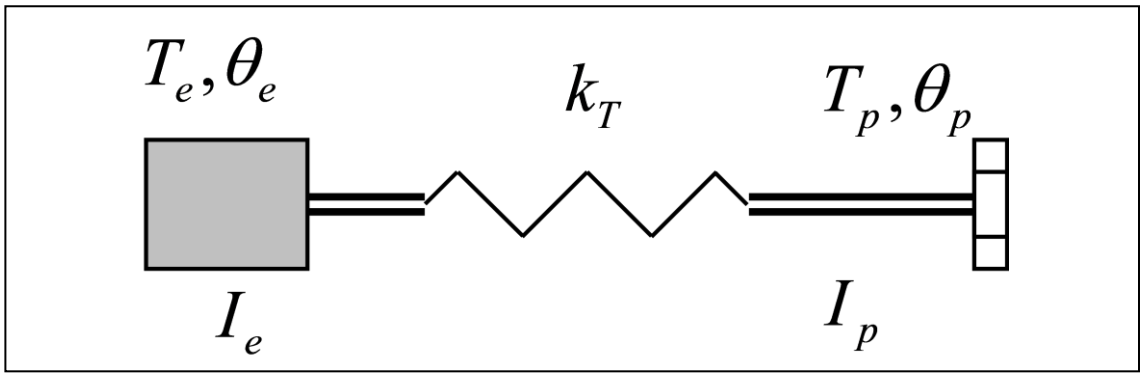

Figure 5.19 Pump free play modelled as non-linear shaft stiffness.

5.2.8 Experimental Non Linear Bulk Modulus Effects

For experimental torque inputs it was observed that the high pressure side was not rising as would be expected. Figure 5.20 shows an initial 88 bar system pressure and 98 bar (high, P1) and 64 bar (low, P2) pressures after a torque input of -1 Nm has been applied. The pump ports are blocked after the pressure transducers and the volumes on either side are equal. Being a closed system, volumes are conserved, therefore for a linear bulk modulus if an equal volume of fluid is transported from the low pressure side to the high pressure side then the pressure fall and rise should be symmetrical. Figure 5.20 shows a 24 bar fall and a 10 bar rise.

This experimental effect was possibly connected to a non-linear bulk modulus. The definitive cause of the experimental pressure differences is unknown, but for simulation purposes the system pressure was lowered to match the mid-point of the experimental pressures.

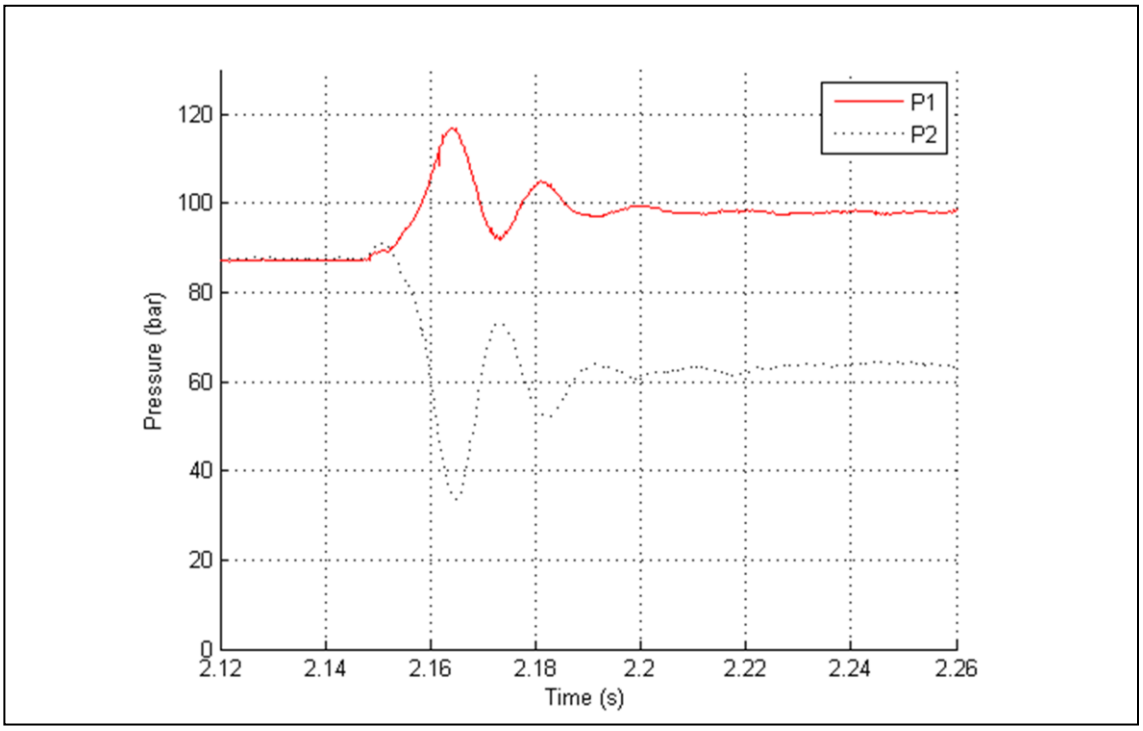

Figure 5.20 Non-symmetric pressures after -1 Nm torque offset initiated.

5.2.9 Simulation Parameter Summary

The parameters used in the simulation of the Resonant EHA are given in Table 5.2. The experiment and simulation were run in open loop torque control. The simulation was run in Simulink version 7.9 using the Adams-Bashworth variable step solver with a maximum step size of 2 ms. The following chapter, Chapter 6, compares experimental and simulation results for the Resonant EHA.

Table 5.2 Proof of concept Resonant EHA simulation parameters

Parameter	Value
Strut stiffness, k	14.6 kN/mm
Piston area, A	550 mm^2
Motor displacement, D	1.52 cm^3/rev
Combined inertia, I	$1.4x10^{-4}$ kgm^2
Back electromotive force constant, K_C	0.28 V/(rad/s)
Motor winding inductance, L	5 mH
Motor winding resistance, R	1.56 Ω
Torque constant, K_t	0.355 Nm/A
Non zero current (torque) offset	-3A
Viscous friction of motor and pump, c_{Sh}	2 mNm/(rad/s)
Internal leakage coefficient of pump, K_{Il1}	$1.0x10^{-13}$ m^3/Pa
Internal leakage coefficient of pump, K_{Il2}	$1.8x10^{-13}$ m^3/Pa
External leakage coefficient of pump, K_{El}	$1.0x10^{-13}$ m^3/Pa

System pressure, P_{Ac}	80 bar
Bulk modulus, B	700 MPa
Vapour pressure	-1 bar
Free play angle θ_{Fp}	40°
Shaft stiffness, k_T	314 Nm/rad
Pump absolute friction positive direction	60 mNm
Pump absolute friction negative direction	120 mNm
Pump friction cross over gradient	400 mNm/(rad/s)
Pump gear inertia, I_p	0.05×10^{-4} kgm^2
Hose (accumulator) volume, V_{Ho}	55 cm^3
Hose effective bulk modulus, B_{Ho}	180 MPa
Internal leakage coefficient of piston, K_{Lp}	1.0×10^{-11} m^3/Pa
Initial volume of each chamber and connection , V_{1i} , V_{2i}	8.9 cm^3
Cylinder friction absolute value, F_{Mx}	±550 N
Cylinder friction cross over gradient, c_{Cf}	500 kN/(m/s)
Displacement input nominal amplitude, x	±0.18mm

Chapter 6
Experimental and Simulation Results

Passive and active experimental and simulation results for the Resonant EHA are presented in this chapter.

6.1 Resonant EHA Passive Results

6.1.1 Experimental Results

All active and passive testing was carried out using a 0.18 mm amplitude sinusoid displacement input, and a semi-static 1 Nm mean torque. Although a 0.35 mm displacement input was initially designed for, testing was carried out at 0.18 mm as the effect of the offset torque to lower the pressure on one side of the pump limited the displacement amplitude that could be used under nominally similar non cavitating conditions in the 10 Hz to 30 Hz testing range.

The measured data for a 20 Hz sinusoidal input for 4 cycles are shown in Figure 6.1. The top graph in Figure 6.1 shows the pressure on either side of the pump. The pressures are centred about separate high and low offset caused by the steady state offset non-zero mean torque. The middle graph is the load cell force, and the bottom graph is the scaled displacement measured by the LVDT on the flex plate. The force waveform transmitted to the load cell has some harmonic distortion. In Figure 6.1 the LVDT displacement waveform can be seen to be not perfectly sinusoidal, which is attributed to the relatively small displacements demanded compared to the size of the testing machine.

The load cell force waveform's frequency components were obtained by taking a Fourier transform. Figure 6.2 shows the harmonic components and the load cell force per displacement input from eight frequencies between 10 and 30 Hz. The magnitude of the fundamental frequency shows a minimum before rising again, while harmonics are consistently present.

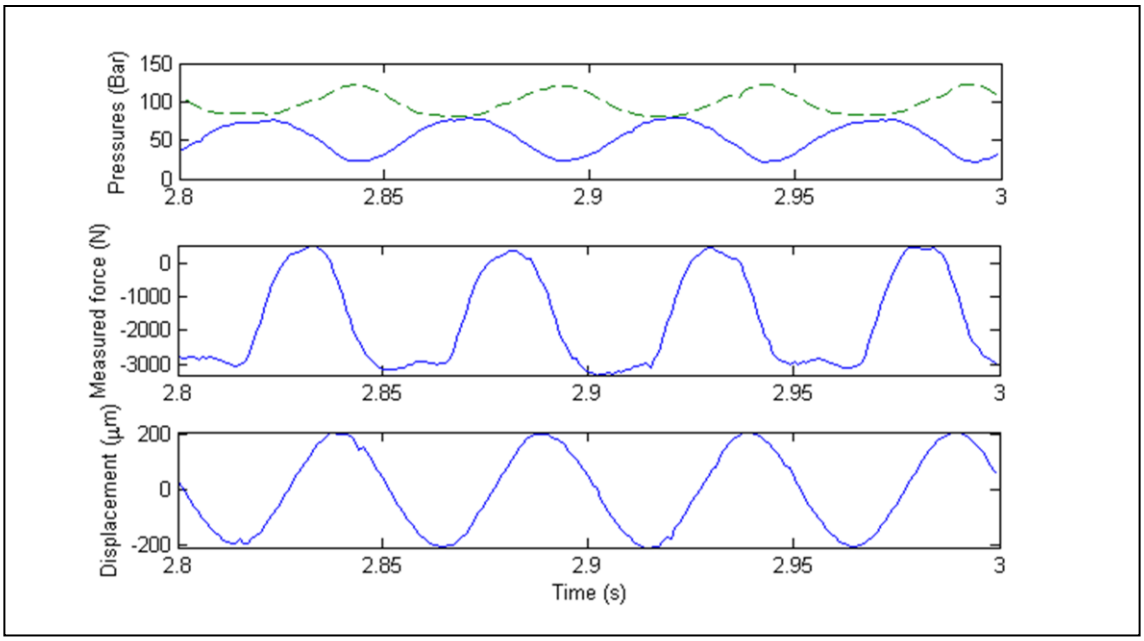

Figure 6.1 Pressures, load cell force and displacement input for 20Hz sinusoidal input.

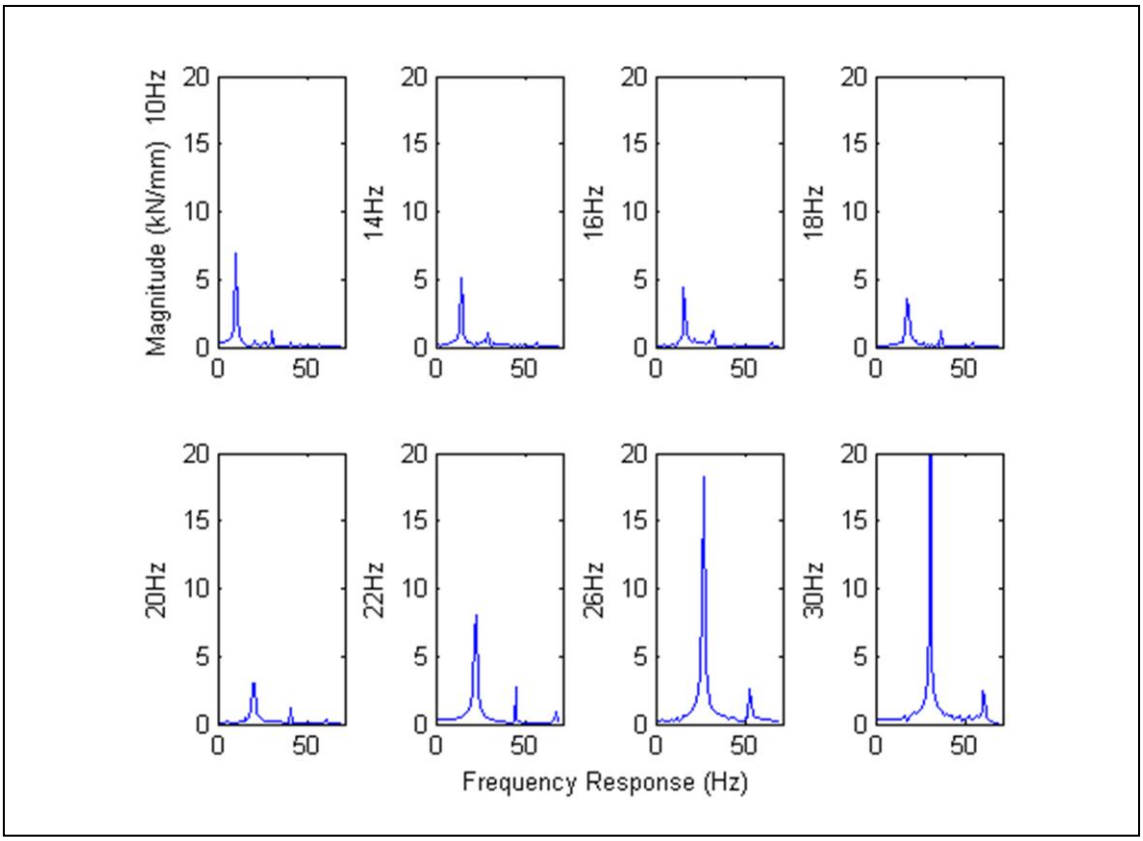

Figure 6.2 Frequency components of passive load cell force for sinusoidal inputs from 10 Hz to 30 Hz.

Figure 6.3 shows the frequency response of the apparent stiffness of the Resonant EHA device acting as a dynamically passive vibration absorber. In Figure 6.3 "RMS" is the root mean square measure of all frequency components in the net force waveform, while "Fundamental" is the net force waveform at only the primary driving frequency.

The baseline equivalent stiffness k_{Bl} represents the response the strut with no isolation device, where the strut acts as a spring with light damping, given by:

$$k_{Bl} = \sqrt{k^2 + (c_{St}\omega)^2} \qquad \textbf{(6.1)}$$

where the value of c_{St} is the damping taken as 40 kNs/m. Figure 6.3 shows that the Resonant EHA works as a passive vibration absorber with a bandwidth from 16.0 Hz to 20.3 Hz. The quality factor Q is found to be 4.7, which is relatively low if the device was only being used as a passive vibration absorber.

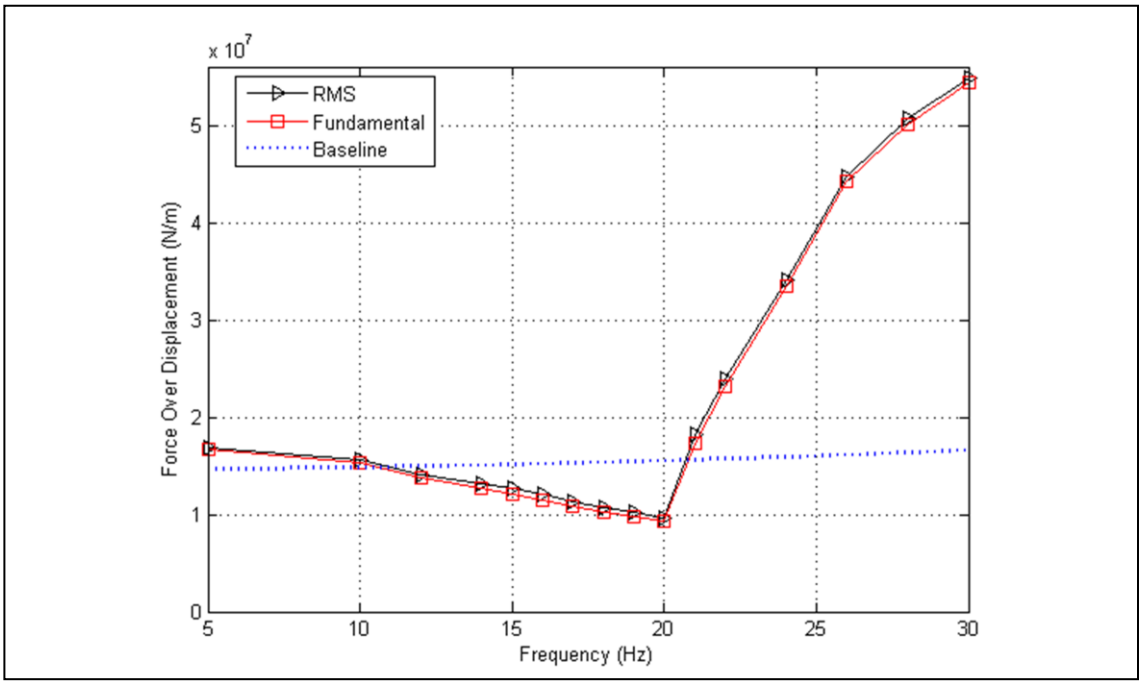

Figure 6.3 Resonant EHA passive frequency response compared with baseline response.

6.1.2 Resonant EHA Passive Simulation and Experimental Results

It was found higher harmonic content in the input influenced how closely the simulation results reflected the experimental results. Experimental displacement data from the flex plate LVDT was used as the input to the simulation as a replacement for a single frequency sinusoid. The proposed final rotorcraft application will include harmonics above the fundamental therefore the use of the simulation input containing harmonics is reasonable.

The RMS and fundamental frequency response of the simulation versus the experiment is given in Figure 6.4. The time series response of the simulation and experimental data at 10 Hz, 20 Hz and 26 Hz are shown for the pressure transducers in Figure 6.5, Figure 6.7 and Figure 6.9 and for the net load cell force in Figure 6.6, Figure 6.8 and Figure 6.10 respectively. The figures show that the simulation passively is a good match to the experimental results up until the resonant frequency.

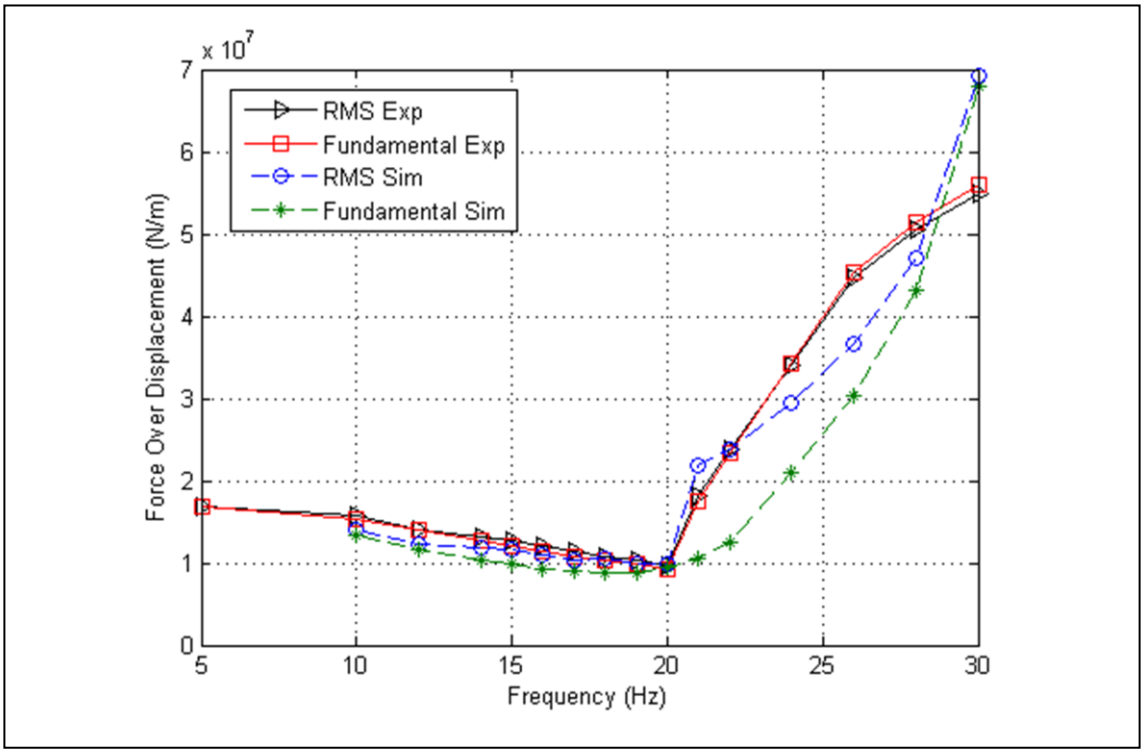

Figure 6.4 Passive experimental and simulation net force magnitude.

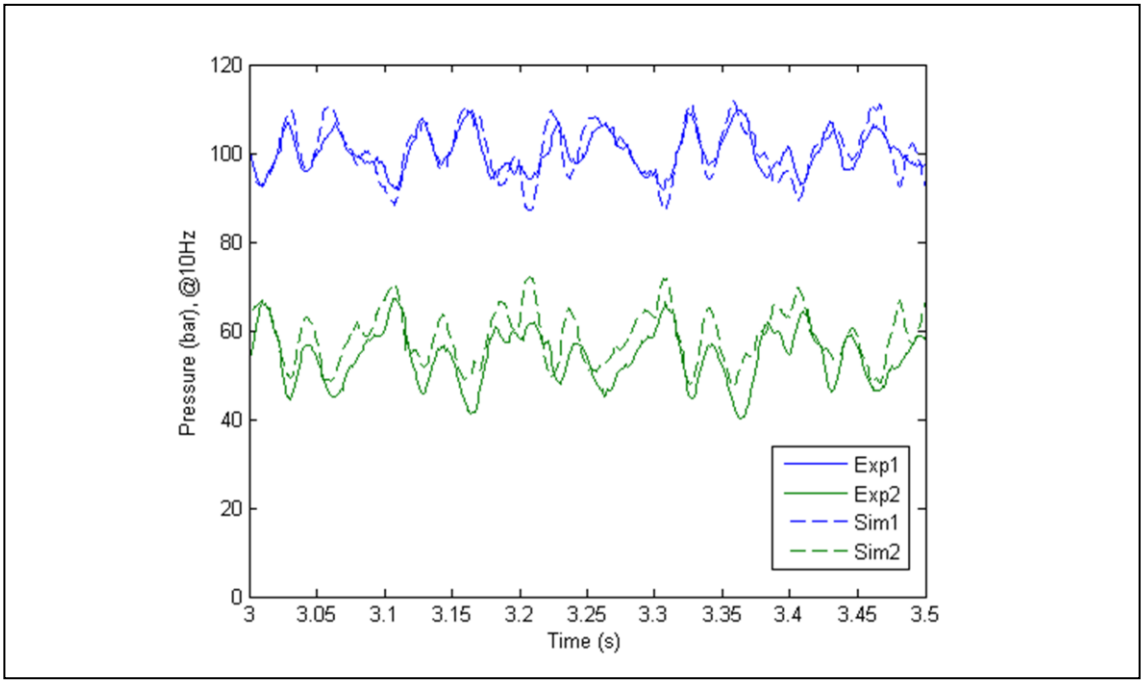

Figure 6.5 Experimental and simulation pressures at 10 Hz.

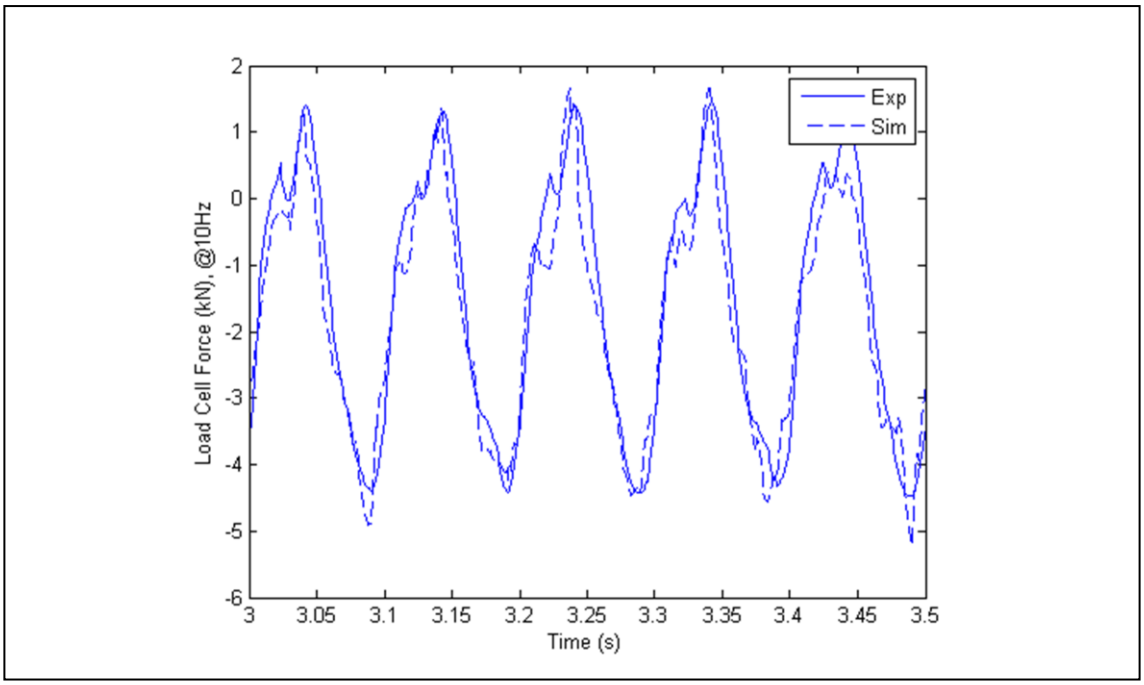

Figure 6.6 Experimental and simulation load cell force at 10 Hz.

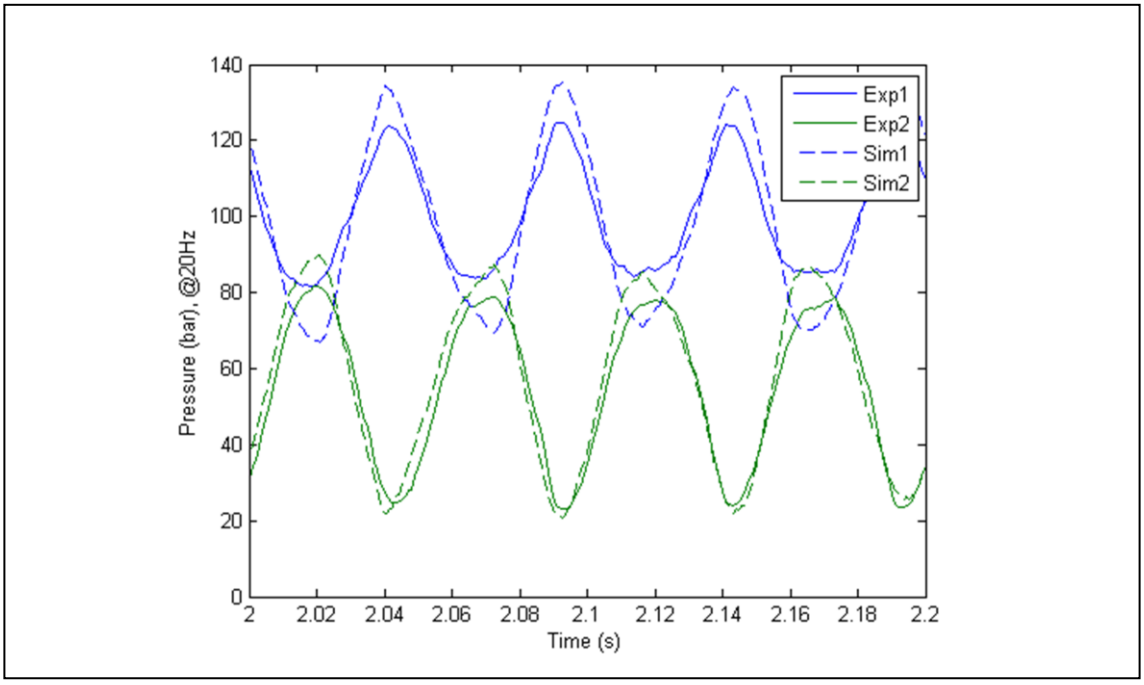

Figure 6.7 Experimental and simulation pressures at 20 Hz.

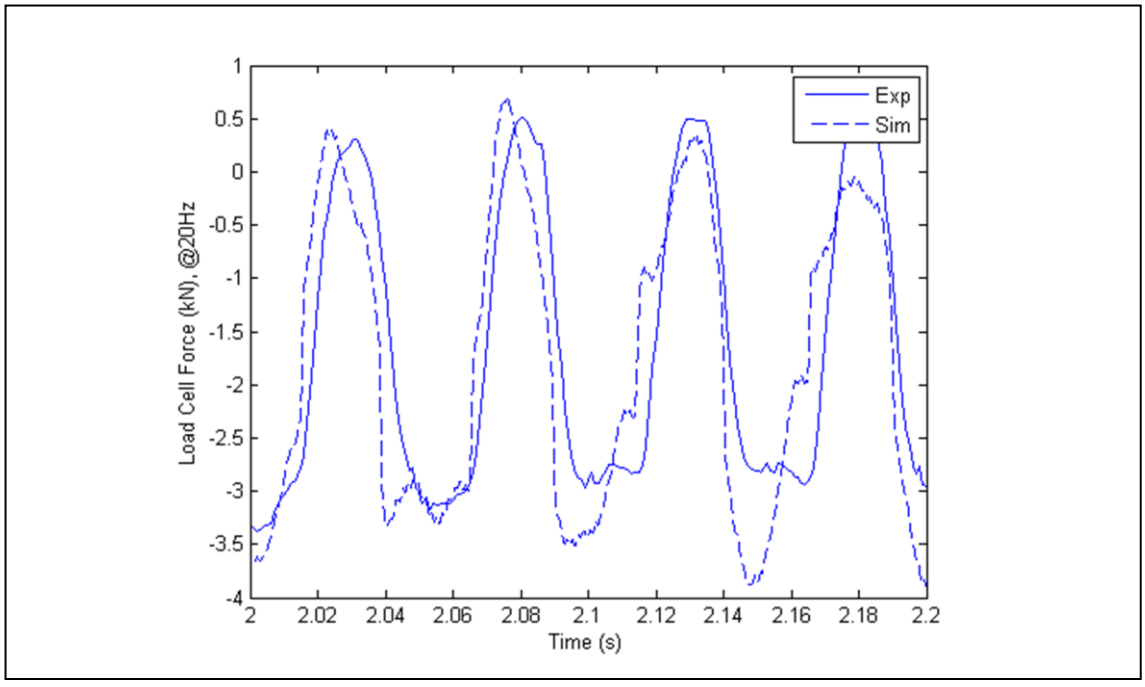

Figure 6.8 Experimental and simulation load cell forces at 20 Hz.

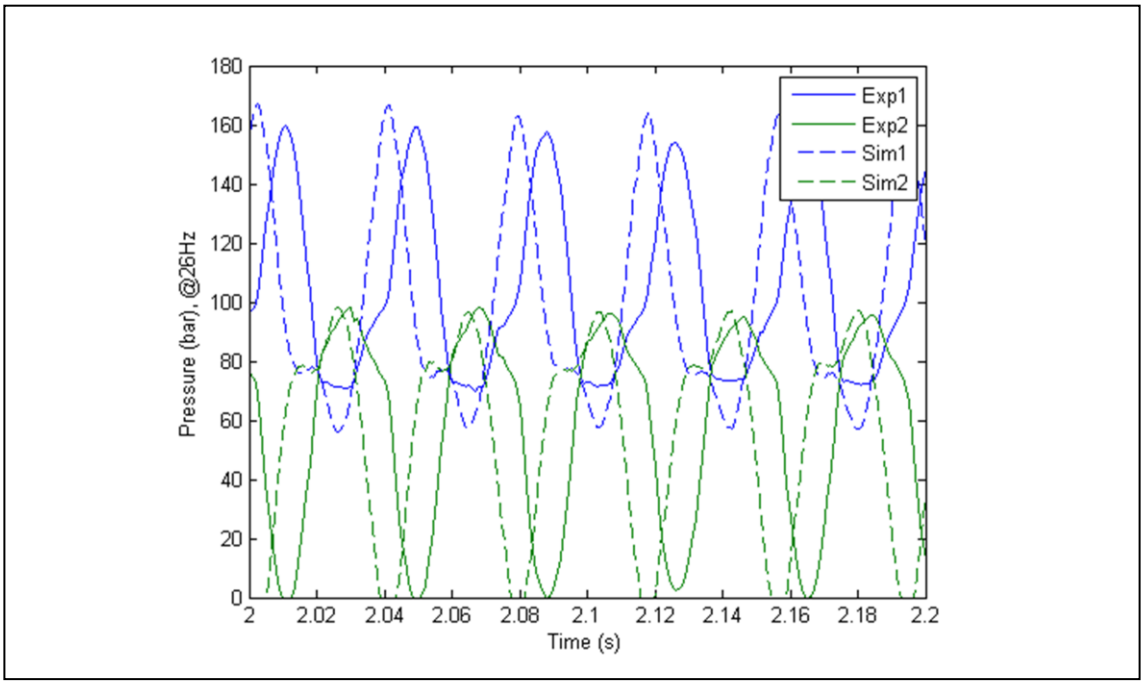

Figure 6.9 Experimental and simulation pressures at 26 Hz.

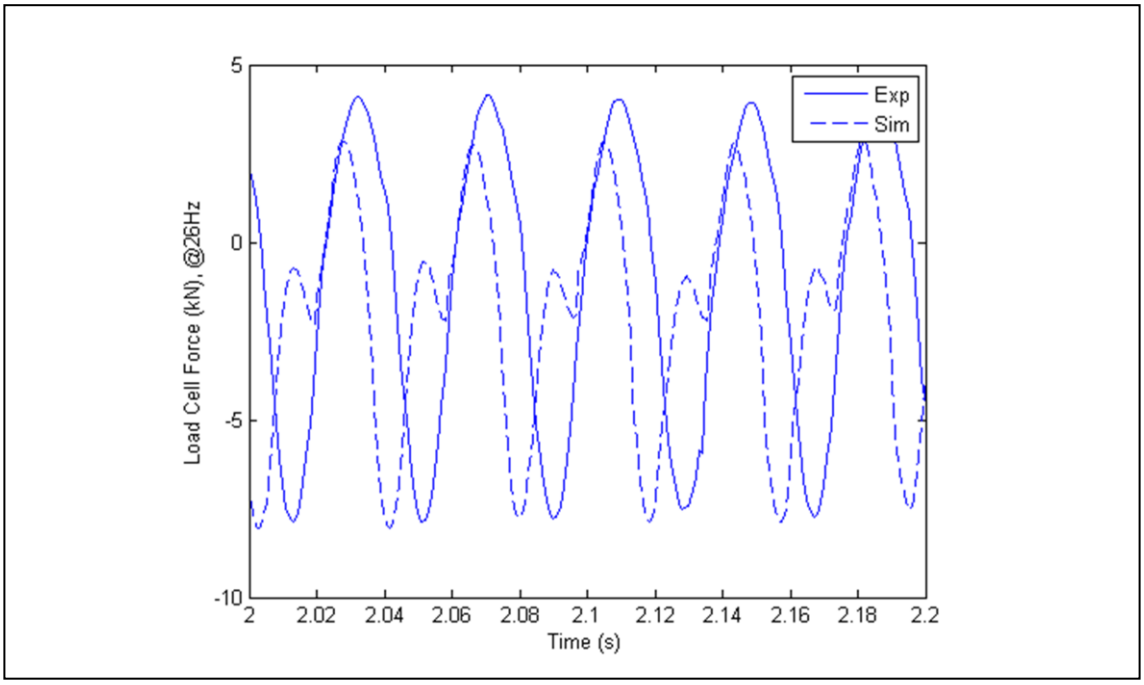

Figure 6.10 Experimental and simulation load cell forces at 26 Hz.

6.1.3 Resonant EHA Passive Operation Discussion

The passive vibration isolation minimum of both the simulation and experiment occurs at 20 Hz. In Figure 6.4, up to the 20 Hz minimum there is consistency between the experimental and simulation net force magnitude, however beyond the minimum there are differences.

Figure 6.5 at 10 Hz matches the experimental pressures with the simulation pressures in time well. At 20 Hz, in Figure 6.7 the pressures in the simulation overlap, while in experiment they do not, implying there are modelling errors affecting the condition when the pressure difference between the two ports is small. The experimental pressure sensor data at 26 Hz in Figure 6.9 shows the measured pressures measured cross-over, which brings the simulation into the free play region. In the simulation the pressures also cross-over, which is encouraging but the simulation response with a 'chatter' type effect which is not present in the experiment is not correct. The pump model could be upgraded to include discrete teeth which may bring better accuracy to comparisons between the simulation and experimental results. Fluid friction losses due to pipe friction, bends or orifices were neglected in the simulation where the maximum fluid velocity in the pipes was in the order of 1.5 m/s. In Figure 6.9 the experimental low pressure side pressures are seen to reduce to zero, implying cavitation was occurring. The simulation has a cavitation model in the form of a pressure limit, where the pressure is cut from going below atmospheric pressure. Using only the pressure limit is not realistic in that the bulk modulus of the fluid is not updated for the new fluid and entrained gas condition, and could improved.

A comparison of the experimental results with the single degree of freedom model is performed to investigate bulk modulus effects. From Chapter 4, Section 4.2.2 the single degree of freedom transfer function between the fuselage force and the input displacement Equation 4.13 is restated:

$$\frac{F_{Fu}(s)}{X(s)} = \left(\frac{A}{D}\right)^2 \left(\frac{Is^2 + c_2 s}{\frac{I}{k_2}s^2 + \frac{c_2}{k_2}s + 1} \right) + c_1 s + k_1 \qquad \textbf{(6.2)}$$

Figure 6.11 is a comparison between the passive experimental results and the single degree of freedom passive transfer function for bulk moduli of 100 MPa to infinite stiffness (the zero degree of freedom model) using the parameters given in Table 6.1. The 100 MPa value which

represents initial reversing torque experimental results, or the zero degree of freedom model which represents an infinitely stiff fluid, do not represent the experimental data well. A fluid stiffness between 300 MPa and 700 MPa appears to represent the data better, but the single degree of freedom model does not represent the higher magnitude forces above 20 Hz accurately due to either cavitation on the low pressure side of the hydraulic circuit, or the occurrence of free play in the gear pump.

The active operation of the proof of concept Resonant EHA is given in the following section, Section 6.2.

Table 6.1 Single degree of freedom passive model parameters

Parameter	Value
Strut stiffness k_1	14.6 kN/mm
Piston area, A	550 mm^2
Motor displacement, D	1.5 cm^3/rev
Combined inertia, I	$1.4x10^{-4}$ kgm^2
Single degree of freedom damping, linear , c_1	$2.4x10^4$ Ns/m
Single degree of freedom damping, rotary , c_2	$4.7x10^{-3}$ Nms/rad
Nominal bulk modulus, B	700 MPa
Fluid volume, V_{To}	8.9 cm^3
Nominal single degree of freedom rotary stiffness, k_2	11.5 Nm/rad

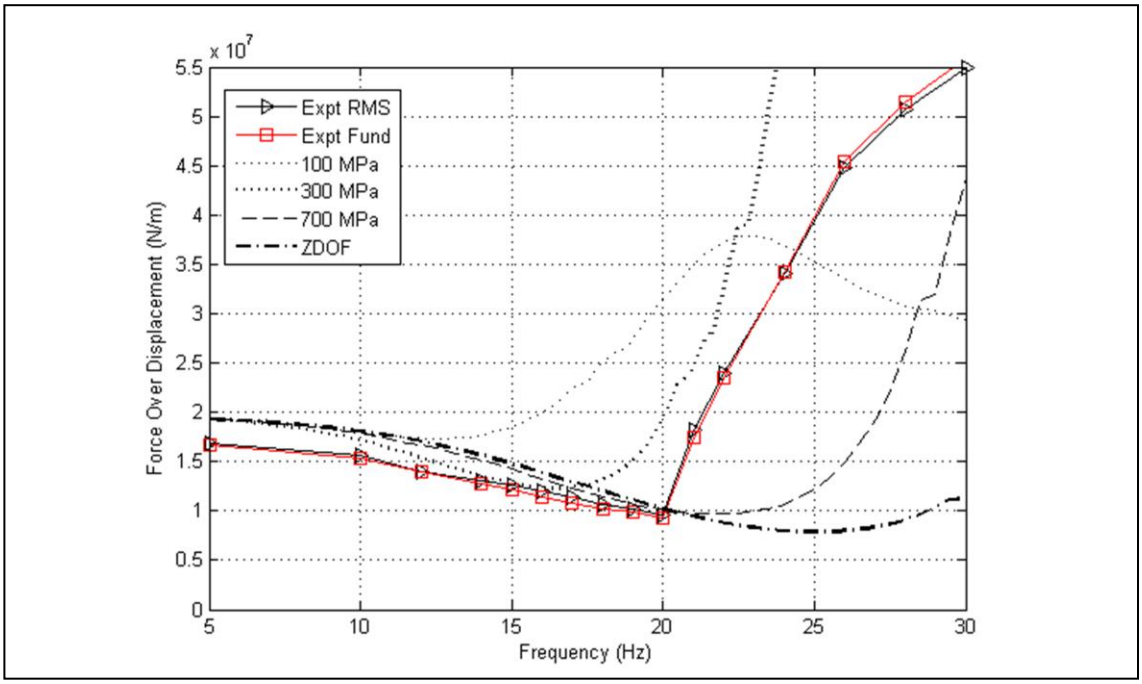

Figure 6.11 Experimental passive force results (N/m) versus single degree of freedom passive model for range of bulk moduli.

6.2 Resonant EHA Active Results

The electric motor was used in torque control, where the magnitude and relative phase of a sinusoidal input was fed into the motor. For each displacement input frequency, the same torque frequency was demanded. The magnitude and phase of the torque was varied at each frequency until a minimum net load force was confirmed.

Figure 6.12 shows the net force on the load cell for a range of phases. The torque input magnitude is 0.64 Nm with a constant -1 Nm offset torque being applied. At -115° a minimum is reached where the fundamental frequency net force is almost completely cancelled and only the higher frequency components remain. Figure 6.13 shows the frequency components of the net force clearly showing the fundamental and higher harmonics. Figure 6.14 illustrates the torque magnitude dependence on finding a correct minimum as well as the phase requirement for each torque. In Figure 6.14 the minimum force occurs at -110° phase difference with a torque amplitude of 0.64 Nm at 20 Hz and a -1 Nm mean offset.

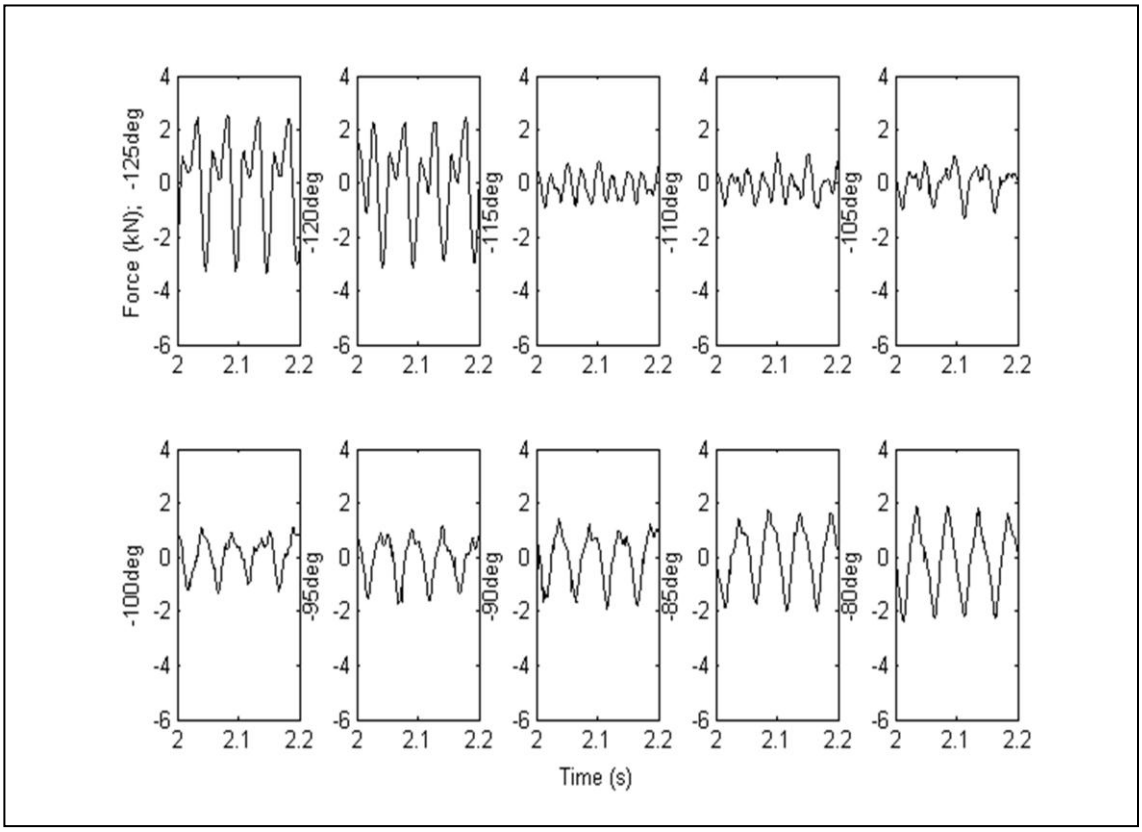

Figure 6.12 Net load cell force variation with phase for 20 Hz constant magnitude input.

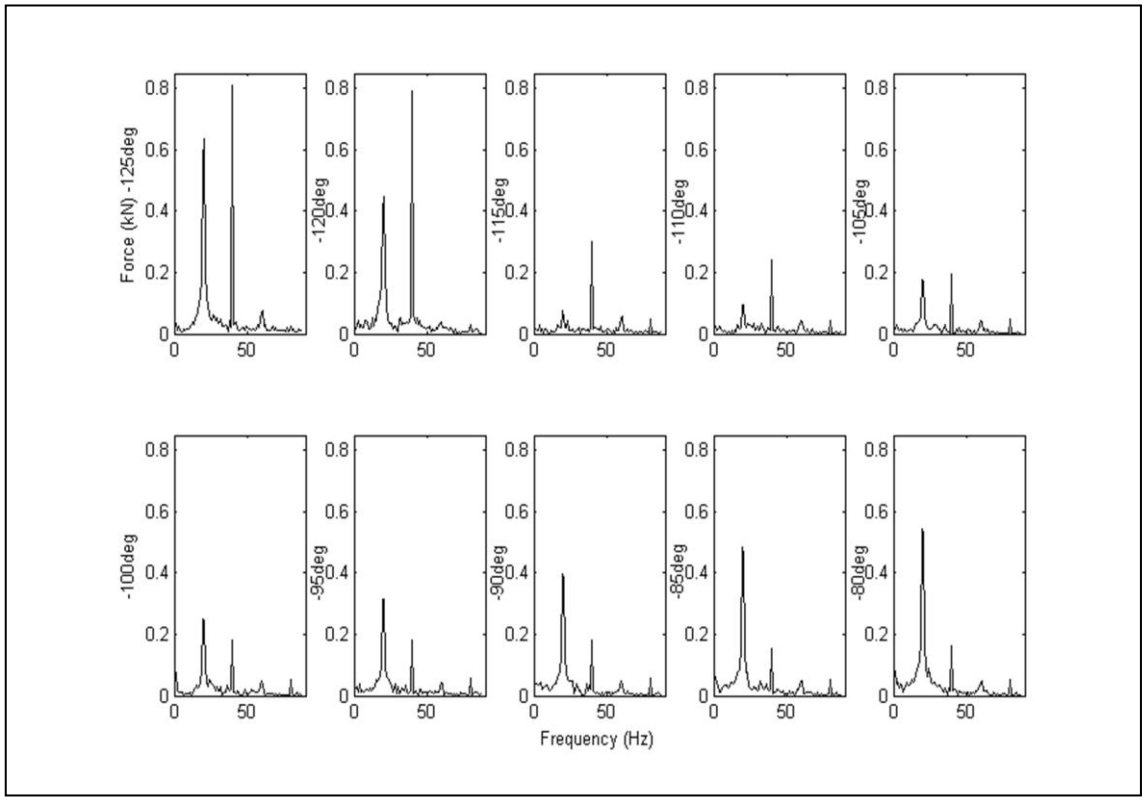

Figure 6.13 Frequency components of net force with phase for 20 Hz input.

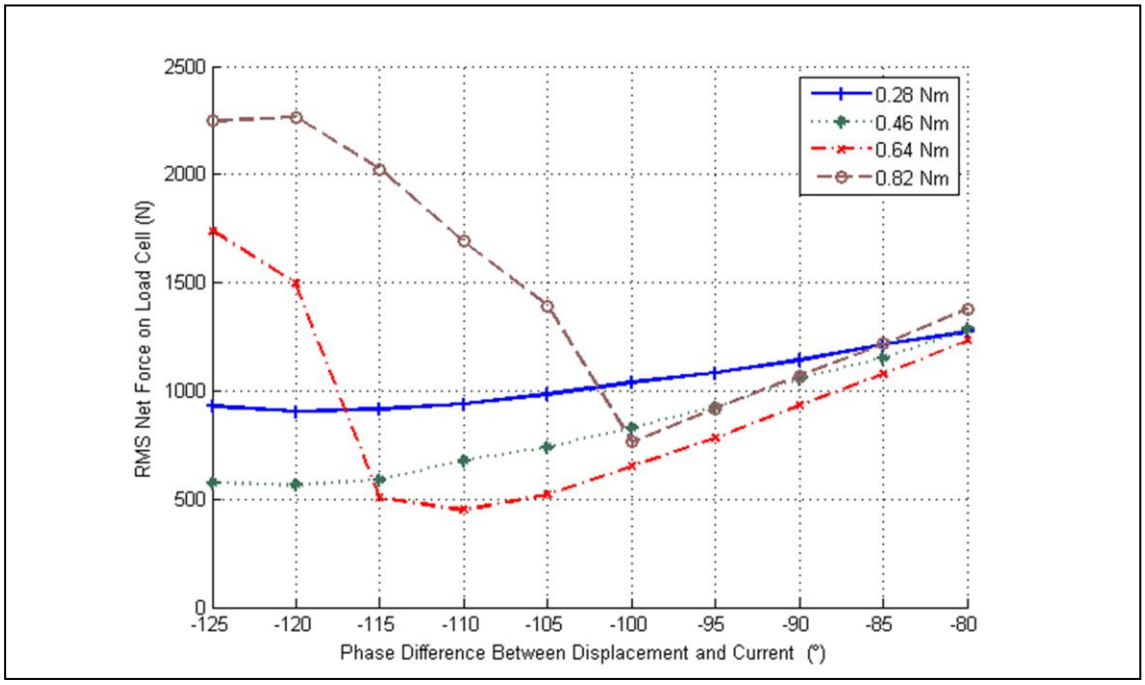

Figure 6.14 RMS net force variation with torque magnitude and phase for 20 Hz input.

For 5 to 30 Hz the fundamental and RMS transmitted net forces at selected frequencies were found through manual adjustment of the torque dynamic magnitude and phase. A constant -1Nm offset torque was applied throughout testing. The dynamic torque magnitude was adjusted in 0.14 Nm increments and the torque phase in 5° increments. The dynamic torque magnitudes required to obtain a minimum net force at 10 Hz and 20 Hz are given in Table 6.2. The experimental and simulation dynamic torque values that obtain minimum net transferred forces agree reasonably well.

The net force results over the range 5 Hz to 30 Hz are shown in Figure 6.15. The active torque inputs significantly lower the transmitted force. True optimisation is not found as harmonics of the waveform were not attempted to be cancelled, and also coarse manual search increments were employed in both torque magnitude and phase when finding the minimum fundamental transferred net force. The use of closed loop adaptive control algorithms to automatically calculate the magnitude and phase of the fundamental frequency and harmonics would be preferable give a true minimum. It would be instructive in future work to implement adaptive control especially to confirm whether the torque magnitude required for the second harmonic is not excessive and that an acceptably stable convergence can be achieved.

Table 6.2 Dynamic torque magnitude for minimum net force.

Frequency (Hz)	**Dynamic Torque Experiment (Nm)**	**Dynamic Torque Simulation (Nm)**
10	0.98	1.04
20	0.57	0.64

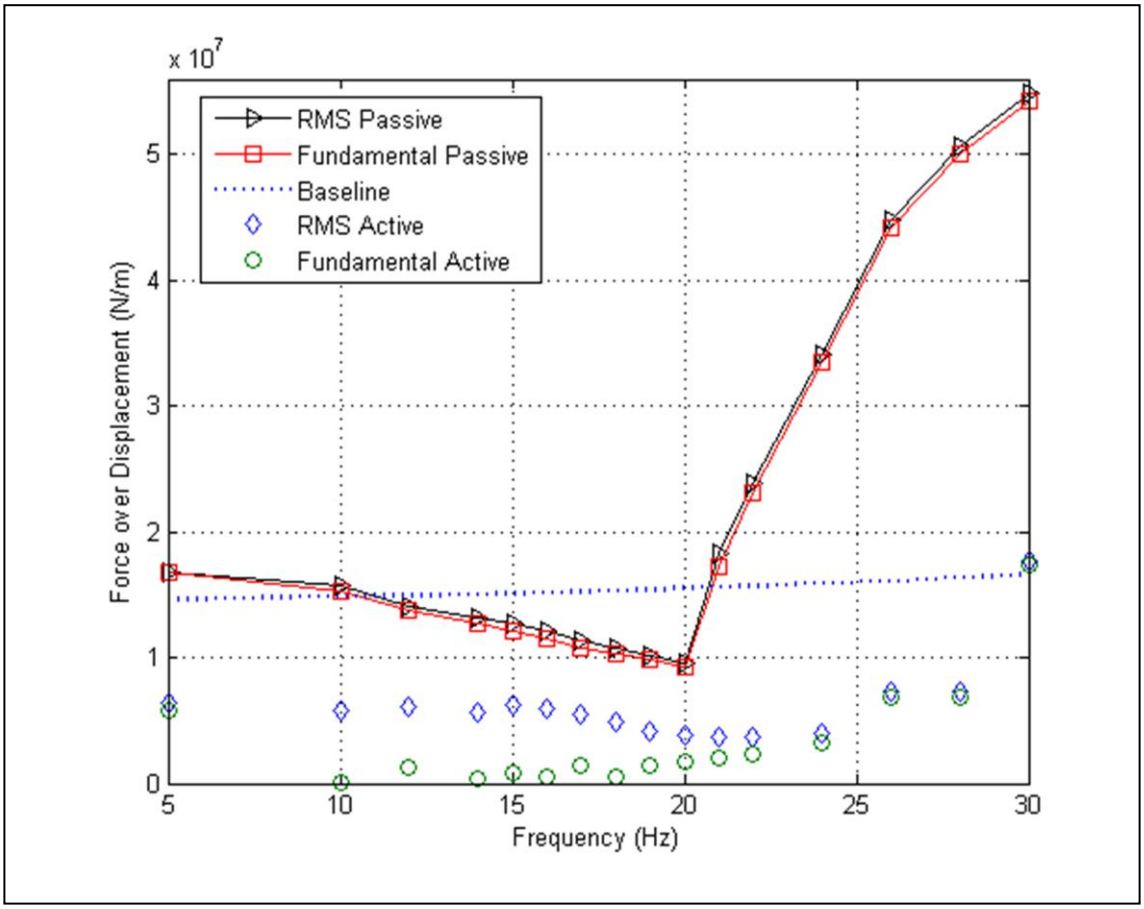

Figure 6.15 Resonant EHA active fundamental and RMS transmitted forces.

6.3 Resonant EHA Discussion

The proof of concept resonant EHA actively achieved RMS vibration reduction of up to a factor of four and near complete cancellation at the fundamental frequency from 10 Hz to 20 Hz against the baseline strut. Above 20 Hz active vibration suppression was possible but the phase window in which to achieve a minimum net force was narrow. The experimentally required dynamic torque of 0.57 Nm at 20 Hz is half the 1.15 Nm that would be required from a frictionless leak free active EHA pushing 0.18 mm against a 14.6 kN/mm spring with the experimental pump and hydraulic cylinder. Considering that the 0.57 Nm is also compensating the relatively high cylinder friction and real losses in the pump the actively augmented vibration suppression system performs well.

The results are promising but it should be emphasised that the non-zero mean torque used in the present experiments limits the immediate practical application of the current Resonant EHA device through increased power consumption and a larger electric motor. The use of a piston pump is more common in commercial EHA's. Although the gear pump was chosen as being low inertia, low displacement piston pumps are available and their inertia is similar to or less than the electric motor rotor inertia. The use of a custom limited angle vane actuator as the hydraulic pump is possible, however maintaining low friction with low leakage could be a concern. The gear pump or limited angle actuator should be investigated in order to obtain to find a stiff, linear hydraulic transmission. Generally how to build a near leak free yet low friction closed hydraulic system is challenging, but replacing the hydraulic cylinder with bellows is one possible direction.

The effect of temperature on the transmission fluid is an issue. The leakage dependence on viscosity is one consideration. Expansion of the fluid with temperature will have to be compensated for with an accumulator to maintain a constant system pressure. Finally, that the Resonant EHA concept is one of four broad device architectures should not be forgotten. Using linear hydraulic gearing with a linear electric motor in light of the experimental stiffness, leakage and friction issues now has renewed interest. Mechanical gearing using rotary or linear transmission devices are also possible. In either case, building a device that is capable to operate hundreds of millions of cycles is a significant design issue.

Chapter 7
Conclusions

Conclusions from the research and recommended future work are given in this chapter.

7.1 Conclusions

The broad scope of electrically powered active vibration suppression devices for mounting between the fuselage and gearbox in rotorcraft was examined in the categories of piezoelectric and electromagnetic actuation.

For piezoelectric actuators the use of hydraulic motion accumulation to achieve a larger stroke from a compact piezoelectric stack actuator, a piezo pump, was examined at a simulation level. It was shown piezo pump current demands and stack temperature rises prohibited the use at the envisaged application size, but piezo pumps have potential for smaller scale with low duty cycle applications.

For electromagnetic actuators the potential of a hybrid actively augmented passive vibration system was investigated. The hybrid device in principle will have a low power demand and be a compact low mass device compared to an active system, and have wider vibration suppression bandwidth than a passive system. The relatively mature use of Hybrid Mass Dampers (HMD) in civil structures was noted in the literature. Chiefly, the notion of using the mass or inertia of the rotary or linear electric motors' moving element with gearing to give passive vibration suppression at the required fundamental frequency has appeal.

For experimental proof of concept purposes a hydraulic linear to rotary gearing mechanism was chosen, leading to the device termed a "Resonant Electro Hydrostatic Actuator (EHA)". Initial modelling showed the feasibility of constructing a Resonant EHA with commercially available electric motors. The torque required, which determines the size of the electric motor, was shown to be dependent on the losses in the system, and if needed how far the operating point is to be shifted from the resonant frequency. The stiffness of the gearing was shown to affect the resonant frequency and harmonics. Simulation results indicated that a hydraulic circuit in which the pump leakage is fed back into the low pressure line would introduce unacceptable

disturbances. To overcome this issue, an integrated electric motor and pump design was chosen in which the electric motor is immersed in hydraulic fluid.

A proof of concept Resonant EHA was built for a 1.5 tonne rotor craft. Experimental testing of the Resonant EHA produced “free play” results that emphasised the critical nature of the gearing mechanism’s stiffness and linearity. The free play was traced to the gear pump and a hypothesis of the origin put forward. To improve the linearity of the transmission the motor was controlled to generate a non-zero mean torque so that the torque never reversed direction during testing. Practically, the introduction of an offset torque leads to a higher continuous power demand which limits the device’s immediate application in the present form.

Passive testing successfully showed the Resonant EHA functions as a passive vibration absorber. Active testing achieved near complete force cancellation of the fundamental frequency of vibration, and reduction by a factor of four of the root mean square forces in the 10 to 20 hertz range. Patent application A12850GB D08 which describes the Resonant EHA device has been assigned to the project industrial partner, AgustaWestland.

7.2 Recommend Future Work

The piezo pump concept has been shown to be suited to low duty cycle small scale applications. It is recommended the range of potential applications be reviewed and new projects based on the new objective be taken into the experimental stage.

The present proof of concept Resonant EHA should be modified to use a piston pump or vane actuator and retesting with the new pump to see if there is an improvement in the free play phenomenon. It is essential that the device gearing that has stable stiffness, linearity and lifetime. With regards to the hydraulic cylinder, active sealing, or a bellows type arrangement to improve the friction versus leakage characteristics should be investigated.

A single degree of freedom analysis of the passive transmission characteristics of hybrid devices showed initial concern regarding the magnification of harmonics. The potential to actively control harmonics for a motor sized to work for vibration suppression at the fundamental frequency would give the hybrid system a significant advantage over passive system, but was not part of this project. Future work on active control techniques are recommended in conjunction with hardware development eliminating free play.

Finally, hybrid actively augmented vibration suppression devices have the possible combinations of mechanical or hydraulic gearing, and rotary or linear resonating masses, giving four distinctive device architectures with many opportunities for further research.

References

[1] P. Konstanzer, B. Enekl, P.-A. Aubourg, and P. Cranga, "Recent advances in Eurocopter's passive and active vibration control," presented at the American Helicopter Society 64th Annual Forum, Montreal, Canada, 2008.

[2] C. R. Fuller, S. J. Elliot, and P. A. Nelson, *Active Control of Vibration*. London: Academic Press, 1996.

[3] J. T. Pearson, R. M. Goodall, and I. Lyndon, "Active control of helicopter vibration," *Computing & Control Engineering Journal*, pp. 277-284, 1994.

[4] H.Yoshida, Y.Takahashi, K.Katayama, T.Imazawa, and N.Murai, "An active microvibration isolation system for hi-tech manufacturing facilities," *Journal of Sound and Vibration*, vol. 123, pp. 269-275, 2001.

[5] A.Preumont, M.Horodinca, I. Romanescu, B. d. Marneffe, M. Avaraam, A.Daraemaeker, Fossens, and A. A. Hanieh, "A six-axis single-stage active vibration isolator based on Stewart platform," *Journal of Sound and Vibration*, vol. 300, pp. 644-661, 2006.

[6] O. Tokhi and S. Veres, *Active sound and vibration control: theory and applications*. London: Institution of Electrical Engineers, 2002.

[7] Y. Nakaji, S. Satoh, T. Kimura, T. Hamabe, Y. Akatsu, and H. Kawazoe, "Development of an active control engine mount system," *Vehicle System Dynamics*, vol. 32, pp. 185-198, 1999.

[8] J. Z. Jiang, M. C. Smith, and N. E. Houghton, "Experimental testing and modelling of a mechanical steering compensator," presented at the ISCCSP, Malta, 2008.

[9] M. C. Smith, "Force controlling mechanical device," U.S. Pat. No. 7316303, 2008.

[10] F. B. Stamps and M. R. Smith, "Method and Apparatus for Improved Vibration Isolation," U.S. Pat. No. 6009983, 1997.

[11] D. R. Halwes and W. A. Simmons, "Vibration Suppression System," U.S. Pat. No. 4236607, 1979.

[12] A. J. H. Goodwin, "Vibration Isolators," U.S. Pat No. 3202388, 1963.

[13] C. Yilmaz and N. Kikuchi, "Analysis and design of passive band-stop filter-type vibration isolators for low-frequency applications," *Journal of Sound and Vibration*, vol. 291, pp. 1004-1028, 2005.

[14] T. Krysinski and F. Malburet, *Mechanical Vibrations: Active and Passive Control*. London: ISTE, 2007.

[15] J. T. Xing, Y. P. Xiong, and W. G. Price, "Passive-active vibration isolation systems to produce zero or infinite dynamic modulus: theoretical and conceptual design strategies," *Journal of Sound and Vibration,* pp. 615-636, 2005.

[16] E. Flint, M. Evert, E. Anderson, and P. Flannery, "Active/passive counter-force vibration control and isolation systems," presented at the IEEE 2000 Aerospace Conference, Montana, USA, 2000.

[17] S. Daley, F. A. Johnson, J. B. Pearson, and R. Dixon, "Active vibration control for marine applications," *Control Engineering Practice,* pp. 465-474, 2003.

[18] S. Daley, I. Zazas, and J. Hatonen, "Harmonic control of a 'smart spring ' machinery vibration isolation system," *Proc Instn Mech Engrs, Part M: Journal of Engineering for the Maritime Environment,* vol. 222, 2008.

[19] S. Daley and I. Zazas, "A recursive least squares based control algorithm for the suppression of tonal disturbances," *Journal of Sound and Vibration,* vol. 331, pp. 1270-1290, 2012.

[20] O. N. Baumann and S. J. Elliott, "Destabilization of velocity feedback controllers with stroke limited inertial actuators," *Journal of the Acoustical Society of America,* vol. 121, pp. 211-217, 2007.

[21] M. R. Jolly, D. J. Rossetti, M. A. Norris, and L. R. Miller, "Hybrid active-passive noise and vibration control system for aircraft," United States Patent, 1998.

[22] Y. Yu, N. G. Naganathan, and R. V. Dukkipati, "A literature review of automotive vehicle engine mounting systems," *Mechanism and Machine Theory,* vol. 36, pp. 123-142, 2001.

[23] H. Mansour, S. Arzanpour, and F. Golnaraghi, "Design of a solenoid valve based active engine mount," *Jounal of Sound and Vibration,* vol. Published online before print, 2011.

[24] N. R. Fisco and H. Adeli, "Smart structures: part II- hybrid controls systems and control strategies," *Scientia Iranica Transactions A:Civil Engineering,* vol. 18, pp. 285-295, 2011.

[25] B. F. Spenser Jr and S. Nagarahjaiah, "State of the art structural control," *Jounal of Structural Engineering,* vol. July, pp. 845-856, 2003.

[26] A. Kareem and T. Kijewski, "Migation of motion of tall buildings with specific examples of recent applications," *Wind and Structures,* vol. 2, pp. 201-251, 1999.

[27] M. D. Symans and M. C. Constantinouf, "Semi-active control systems for seismic protection of structures, a state of the art review," *Engineering Structures,* vol. 21, pp. 469-487, 1999.

[28] Y. Nakamura, K.Tanaka, M.Nakayama, and T.Fujita, "Hybrid mass dampers using two types of electric servomotors: AC servomotors and linear-induction servomotors," *Earthquake Engineering and Structural Dynamics,* vol. 30, pp. 1719-1743, 2001.

[29] G. M. Stewart and M. A. Lackner, "The effect of actuator dynamics on active structural control of offshore wind turbines," *Engineering Structures,* vol. 33, pp. 1807-1816, 2011.

[30] O. Gomis-Bellmunt and L. Flavio Campanile, *Design rules for actuators in active mechanical systems*: Springer, 2010.

[31] J. E. Huber, N. A. Fleck, and M. F. Ashby, "The selection of mechanical actuators based on performance indices," *Proceedings of the Royal Society of London Series a-Mathematical Physical and Engineering Sciences,* vol. 453, pp. 2185-2205, Oct 8 1997.

[32] C. Bowen and A. R. Plummer, "ACSR active strut feasibility study," PTMC, University of Bath, Bath2007.

[33] P. Jänker and F. Claeyssen, "New actuators for aircraft and space applications," presented at the International Conference on New Actuators, Bremen, Germany, 2006.

[34] G. A. Lesieutre, J. J. Loverich, G. H. Koopmann, and E. M. Mockenstrum, "Increasing the mechanical work output of an active material using a nonlinear motion transmission mechanism," *Journal of Intelligent Material Systems and Structures,* vol. 15, 2004.

[35] R. Vos, R. Barrett, R. d. Breuker, and P. Tiso, "Post-buckled precompressed elements: a new class of control actuators for morphing wing UAVs," *Smart Materials & Structures,* vol. 16, 2007.

[36] T. Galante and Galante, "Design, modelling, and performance of a high force piezoelectric inchworm motor," *Journal of Intelligent Material Systems and Structures,* vol. 10, p. 962, 1999.

[37] J. J. Loverich, G. H. Koopmann, G. A. Lesieutre, J. E. Frank, and W. Chen, "A new piezoelectric actuator using a feed-screw for quasi-static motion accumulation - Part I: Experimental development," *Journal of Intelligent Material Systems and Structures,* vol. 19, pp. 73-81, Jan 2008.

[38] J. J. Loverich, G. H. Koopmann, and G. A. Lesieutre, "A new piezoelectric actuator using a feed-screw for quasi-static motion accumulation - Part II: Mathematical modeling and design optimization," *Journal of Intelligent Material Systems and Structures,* vol. 19, pp. 83-91, Jan 2008.

[39] S.-B. Choi and Y.-M. Han, *Piezoelectric actuators: control applications of smart materials*: CRC-Press, 2010.

[40] Q. Cui, C. Liu, and X. F. Zha, "Simulation and optimization of a piezoelectric micropump for medical applications," *The International Journal of Advanced Manufacturing Technology*, vol. 36, p. 516, 2008.

[41] S. John, J. Sirohi, G. Wang, and N. M. Wereley, "Comparison of piezoelectric, magnetostrictive, and electrostrictive hybrid hydraulic actuators," *Journal of Intelligent Material Systems and Structures*, vol. 18, pp. 1035-1048, Oct 2007.

[42] J. Sirohi, C. Cadou, and I. Chopra, "Investigation of the dynamic characteristics of a piezohydraulic actuator," *Journal of Intelligent Material Systems and Structures*, vol. 16, pp. 481-492, Jun 1 2005.

[43] C. Cadou and B. Zhang, "Performance modelling of a piezo-hydraulic actuator," *Journal of Intelligent Material Systems and Structures*, vol. 14, pp. 149-160, Mar 2003.

[44] W. S. Oates and C. S. Lynch, "Piezoelectric hydraulic pump system dynamic model," *Journal of Intelligent Material Systems and Structures*, vol. 12, pp. 737-744, Nov 2001.

[45] H. H. Tan, W. Hurst, and D. Leo, "Performance modelling of a piezohydraulic actuation system with active valves," *Smart Materials & Structures*, vol. 14, pp. 91-110, Feb 2005.

[46] A. Chaudhuri, J.-H. Yoo, and N. M. Wereley, "Design, test and model of a hybrid magnetostrictive hydraulic actuator," *Smart Materials & Structures*, pp. 1-21, 2009.

[47] A. Chaudhuri and N. M. Wereley, "Compact hybrid electrohydraulic actuators using smart materials: a review.," *Journal of Intelligent Material Systems and Structures*, vol. 22, pp. 1-37, 2011.

[48] S. John, C. Cadou, J. H. Yoo, and N. M. Wereley, "Application of CFD in the design and analysis of a piezoelectric hydraulic pump," *Journal of Intelligent Material Systems and Structures*, vol. 17, pp. 967-979, Nov 2006.

[49] B. Denkena and S. Simon, "Computer-aided analysis of flow-characteristics of a micro-positioning system," *Prod. Eng. Res. Devel.*, vol. 2, 2008.

[50] D. G. Lee, S. W. Or, and G. P. Carman, "Design of a piezoelectric-hydraulic pump with active valves," *Journal of Intelligent Material Systems and Structures*, vol. 15, pp. 107-115, Feb 2004.

[51] J. Sirohi and I. Chopra, "Design and development of a high pumping frequency piezoelectric-hydraulic hybrid actuator," *Journal of Intelligent Material Systems and Structures*, vol. 14, pp. 135-147, Mar 2003.

[52] R. Rammer, P. Konstanzer, and P. Janker, "Dynamical behavior of a piezo-hydraulic hybrid actuator," presented at the Sixteenth International Conference on Adaptive Structures and Technologies, 2006.

[53] J. F. Jansen, R. F. Lind, J. B. Chesser, and L. J. Love, "Design analysis, fabrication and testing of a novel piezoelectric pump," Oak Ridge National Laboratory2003.

[54] D. G. Lee, D. D. Shin, and G. P. Carman, "Large flow rate/high frequency microvalve array for high performance actuators," *Sensors and Actuators a-Physical*, vol. 134, pp. 257-263, Feb 29 2007.

[55] L. D. Mauck, W. S. Oates, and C. Lynch, "Piezoelectric hydraulic pump performance," *Smart Structures and Materials 2001: Industrial and Commercial Applications of Smart Structures Technologies*, vol. 4332, pp. 246-253, 2001.

[56] R. Rammer and P. Jänker, "Potential of piezo hydraulic actuators for aerospace," presented at the Recent Advances in Aerospace Actuation Systems and Components, Toulouse, France, 2007.

[57] D. T. Nosse and M. J. Dapino, "Magnetorheological valve for hybrid electrohydrostatic actuation," *Journal of Intelligent Material Systems and Structures*, vol. 18, pp. 1121-1136, Nov 2007.

[58] W. S. Oates, L. D. Mauck, and C. S. Lynch, "System dynamic modeling of a piezoelectric hydraulic pump," *Smart Structures and Materials 2002: Modeling, Signal Processing, and Control*, vol. 4693, pp. 598-606, 2002.

[59] P. Jänker, P. Konstanzer, and R. Rammer, "Hydraulic actuator having a fluid delivery unit inside the actuator piston ", 2007.

[60] N. Sclater, *Mechanisms and Mechanical Devices*: McGraw-Hill, 2011.

[61] Z. A. Chaudhuri, B. E. Wake, A. Bagai, P. F. Lorber, and A. J. Collins, "Active rotor development for primary and secondary flight control," presented at the American Helicopter Society 65th Annual Forum, Grapevine,Texas, 2009.

[62] M. Todeschi, "A380 flight control actuation - Lessons learned on EHAs design," presented at the Recent Advances in Aerospace Actuation Systems and Components, Insa Toulouse, 2007.

[63] R. Navarro, "Performance of an Electro-Hydrostatic Actuator on the F-18 Systems Research Aircraft," 1997.

[64] R. Kang, Z. Jiao, S. Wu, Y. Shang, and J.-C. Mare, "The nonlinear accuracy model of electro-hydrostatic actuator," presented at the IEEE Conference on Robotic, Automation and Mechatronics, 2008.

[65] K. G. Cleasby and A. R. Plummer, "A novel high efficiency electro-hydrostatic flight simulator motion system," presented at the Fluid Power Motion Control (FPMC), UK,Centre for PTMC, 2008.

[66] R. W. Henke, *Fluid Power Systems and Circuits*: Penton Publishing.

[67] D. N. Johnston, "Numerical hodelling of reciprocating pumps with self-acting valves," *Proc Instn Mech Engrs*, vol. 205, pp. 87-96, 1991.

[68] S. John, A. Chaudhuri, C. Cadou, and N. M. Wereley, "Unsteady fluid flow in hybrid hydraulic actuators," *Journal of Intelligent Material Systems and Structures*, vol. 20, pp. 2201-2214, 2009.

[69] J. Pritchard, R. Ramesh, and C. Bowen, "Time-temperature profiles of multi-layer actuators," *Sensors and Actuators A-Physical*, vol. 115, pp. 140-145, 2004.

[70] B. Massey and J. Ward-Smith, *Mechanics of Fluids*, 7th ed., 1998.

[71] R. Flitney, *Seals and sealing handbook (5th edition)*: Elsevier, 2007.

[72] A. Bullock, "Fundamental concepts associated with hydraulic seals for high bandwidth actuation," Thesis (Ph.D.), University of Bath, Bath, 2010.

Appendix A
Target Specifications

The strut target specifications for the AW101 scale rotorcraft are as follows:

Static load:	-80 kN to +200 kN in direction of strut
Temperature range:	-40°C to +135°C
Maximum compressive load:	200 kN (must not buckle in crash landing)
Pseudo-static displacement:	4 mm peak to peak
Torque loads:	Negligible
Side loads:	Negligible
Length:	1006 mm between mounts
Mounting type:	Pin jointed
Diameter:	To fit surrounding equipment

If the actuator is mounted in parallel with a 100kN/mm composite tube the actuator specifications are as follows:

Dynamic load:	Greater than -35 kN to +35 kN in direction of strut
Dynamic stroke:	0.7 mm peak to peak
Operating frequency:	18 Hz continuous with a variation of operating frequency by up to -20% anticipated.
Velocity at full load:	33.6 mm/s
Acceleration:	3775 mm/s^2
Ideal input average power:	Greater than 182 W (without power regeneration, force and velocity are sinusoidal with 90 degree phase difference)
Torque loads:	Negligible
Side loads:	Negligible
Robustness:	10000 hour's operational lifetime (approximately 640 million cycles at 18Hz)

Power supply:	Up to 750 W
Safety requirements:	In case of power supply failure then actuator runs free

More general specifications for the strut for a range of helicopters include

Operating frequency:	15 Hz to 35 Hz
Dynamic stroke:	Approximately 0.7 mm peak to peak

From the actuator specifications the following indices can be implied:

(i) A maximum of 750 W of power per strut is available and a system with no energy storage needs to be able to provide an output power of 182 W. This implies that the electrical to mechanical energy conversion has to have a minimum goal of 24% efficiency.

(ii) For the AW101 the dynamic stroke to strut length ratio is 300 μm /1 m = $3x10^{-4}$, but for smaller helicopters due to smaller strut sizes the required dynamic stroke ratio might be comparatively larger.

The average output power requirement was as an actuator presses against a spring, the force is proportional to the displacement, and the velocity will be 90 degrees out of phase. The power required is calculated as the vector of force multiplied by velocity in the extension and compression part of the cycle only.

Appendix B

Piezo Pump Scalability

	Light 1	Light 2	Intermediate 1	Intermediate 2	Heavy
Mean Take Off Weight (kg)	2000	3000	5000	7000	10000
Strut Stiffness (kN/mm)	20	30	50	70	100
Actuator Dynamic Stroke (mm)	0.35	0.35	0.35	0.35	0.35
Blade Passing Frequency (Hz)	25	25	24	24	18
Actuator Dynamic Load (kN)	7	10.5	17.5	24.5	35
Strut Length (m)	0.5	0.5	0.7	0.7	1
Max Pressure (bar)	150	150	150	150	150
Piston Area (m^2)	0.000467	0.0007	0.00117	0.00163	0.00233
Rod Diameter (mm)	25	25	25	30	30
Rod Area (m^2)	0.000491	0.000491	0.000491	0.000707	0.000707
Piston Diameter (mm)	34.9	38.9	45.9	54.6	62.2
Max Flow (m^3/s)	0.0000257	0.0000385	0.0000616	0.0000862	0.0000924
Chamber Diameter (mm)	35	45	45	56	56
Chamber Area (m^2)	0.000962	0.00159	0.00159	0.00246	0.00246
Driving Frequency (Hz)	400	400	400	400	400
Displacement (µm)	66.7	60.5	96.8	87.5	93.8
Free Displacement (µm)	133	121	194	175	188
Target Blocking Force (kN)	28.9	47.7	47.7	73.9	73.9
Piezo (PI Instruments Catalogue)	**P035.80**	**P045.80**	**P045.90**	**P056.90**	**P056.90**
Blocking Force (kN)	28	44	45	70	70
Free Displacement (µm)	120	120	180	180	180
Capacitance (nF)	5200	8800	13000	21000	21000
Piezo Diameter (mm)	35	45	45	56	56
Piezo Length (mm)	116	116	169	169	169
Piezo Mass (kg)	0.871	1.44	2.1	3.25	3.25
Current Demand (A)	**6.53**	**11.1**	**16.3**	**26.4**	**26.4**
Temperature Rise (degrees C)	**87.5**	**113**	**113**	**140**	**140**

Appendix C

Resonant EHA Scalability

		Light 1	Light 2	Intermediate 1	Intermediate 2	Heavy
	Mean Take Off Weight (kg)	2000	3000	5000	7000	10000
	Strut Stiffness (kN/mm)	20	30	50	70	100
	Actuator Dynamic Stroke (mm)	0.35	0.35	0.35	0.35	0.35
	Blade Passing Frequency (Hz)	25	25	24	24	18
	Actuator Dynamic Load (kN)	7	10.5	17.5	24.5	35
	Max Pressure (bar)	150	150	150	150	150
	Piston Area (m^2)	0.000467	0.0007	0.00117	0.00163	0.00233
	Rod Diameter (mm)	25	25	25	30	30
	Rod Area (m^2)	0.000491	0.000491	0.000491	0.000707	0.000707
	Piston Diameter (mm)	34.9	38.9	45.9	54.6	62.2
	Max Flow (m^3/s)	0.0000257	0.0000385	0.0000616	0.0000862	0.0000924
	Max Pressure Rise (bar/s)	23600	23600	22600	22600	17000
	Zero DOF Equivalent Mass (kg)	810	1220	2200	3080	7820
	Single DOF Mass Estimate (kg)	567	851	1540	2150	5470
1	Nominal Pump Displacement (cm^3/rev)	1.35	2	3.3	4.65	3.46
	Maximum Inertia ($kgcm^2$)	1.2	1.76	3.12	4.42	3.05
	Torque -10% of Resonant Freq	1.56	2.3	3.8	5.3	4
	Torque +10% of Resonant Freq	1.23	1.9	3.2	4.4	3.3
2	Nominal Pump Displacement (cm^3/rev)	0.6	1	1.6	2.3	1.8
	Maximum Inertia ($kgcm^2$)	0.238	0.44	0.733	1.08	0.825
	Torque -10% of Resonant Freq	0.71	1.2	1.8	2.6	2.1
	Torque +10% of Resonant Freq	0.56	1	1.5	2.3	1.7
3	Nominal Pump Displacement (cm^3/rev)	0.3	0.5	0.8	1.15	0.9
	Maximum Inertia ($kgcm^2$)	0.0594	0.11	0.183	0.271	0.206
	Torque -10% of Resonant Freq	0.39	0.58	0.9	1.3	1
	Torque +10% of Resonant Freq	0.31	0.48	0.7	1.1	0.85